IDEA League

Geophysical methods for forensic investigations: detection and characterization of simulated clandestine burials using GPR and GCM

Master of Science in Applied Geophysics
Research Thesis

Kate Brooks

Delft University of Technology

IDEA League

Geophysical methods for forensic investigations: detection and characterization of simulated clandestine burials using GPR and GCM

by

Kate Brooks

Supervisors (TU Delft):	Prof. dr. ir. E. Slob Dr. D. Ngan-Tillard Dr. ir. D. Draganov
Supervisor (NP):	M. Lüschen
Supervisor (NFI):	C. Nienaber
Institution:	Delft University of Technology
Place:	Faculty of Civil Engineering and Geoscience, Delft
Project Duration:	March 2022 - August, 2022

Cover Image: TUDelft.

TUDelft

Preface

This dissertation is an extension of previous works investigating the application of geophysical methods in the detection of clandestine burials for applications in homicide investigations and forensic research at the ARISTA facility. Data acquisition was carried out with the help of Mark Lüschen from the Dutch national police, as well as Cara Carpenter, a colleague and friend. Evert Slob, Deyan Draganov, and Dominique Ngan-Tillard were the supervisors of this thesis, as well as Mark Lüschen and Coen Nienaber from the Netherlands Forensic Institute. Data collected in this investigation which was not included in this report can be found in the TU Delft Webdrive for anyone seeking to continue this research.

This work would not have been possible without the help and donation of time from numerous individuals. Thank you to my supervisors Evert Slob, Deyan Draganov, and Dominique Ngan-Tillard for their guidance and support throughout all phases of this project. Thank you in particular to Mark Lüschen for his generous help and company in the field, and for the use of geophysical instruments from the Dutch national police. Thank you to the organizers at ARISTA for allowing us access on numerous occasions to this unique and interesting test site. Thank you as well to those at the Netherlands Forensic Institute, in particular Coen Nienaber for providing us with important context for the investigation, and to Mike Groen for the use of the GPR. Thank you to Florencia Balestrini and Jan Thorbecke for helping me on multiple occasions with applying electromagntic interferometry and adaptive subtraction, and with the large learning curve associated with programming in linux. Most of all thank you to my friends and family, my classmates, and in particular Teus and Cara, for their support throughout this challenging yet rewarding project. I couldn't have - and wouldn't have wanted to - do it without you.

Kate Brooks
Delft, August 2022

Abstract

In this thesis I conducted ground penetrating radar (GPR) and ground conductivity meter (GCM) surveys to detect the presence of simulated clandestine burials at the Amsterdam Research Initiative for Subsurface Taphonomy and Anthropology (ARISTA) test facility, and determine their characteristic response in this environment; providing valuable insights and recommendations for forensic investigations. I performed four days of GPR and GCM surveys over three simulated clandestine burials at ARISTA. I collected common-offset GPR data to investigate changes to burial detectability due to different central antenna frequencies (250 MHz and 500 MHz), different GPR instruments (NOGGIN or pulseEKKO), changes to survey grid orientation relative to burials, and increased soil moisture content in the survey area. Additionally, I acquired common-source GPR data to examine the efficacy of electromagnetic interferometry (EI) and adaptive subtraction (AS) methods in improving burial detectability. I conducted GCM surveys with two coil configurations, (horizontal co-planar (HCP) and vertical co-planar (VCP)), three intercoil spacings (0.32 m, 0.71 m, 1.18 m), two different line spacings (0.5 m, 0.25 m) and in the presence of variable soil moisture content. I also performed low induction number (LIN) correction and elevation correction procedures on GCM data to determine the extent to which these influence the detectability of clandestine burials in this environment.

In common-offset radargrams characteristic burial anomalies take on many forms, appearing as disruptions to existing features (direct-wave arrivals and soil horizons) and as isolated reflection events (hyperbolic events and burial length horizontal anomalies). In timeslices, burials are characterized by high or low amplitude rectangular anomalies. When used in conjunction, radargrams and timeslices produced characteristic responses regardless of survey grid orientation, consistent with the locations of the burials. Increased soil moisture at the site improved the detectability of burials and the 250 MHz antenna was found to be superior to the 500 MHz antenna in obtaining a characteristic burial response, though both were successful to a large extent. EI and AS processing techniques were successful in removing direct-wave contributions in radargrams, though detectability was not significantly improved when compared to raw data. Overall, the three burials were detected using GPR to various extents, and in future work thorough historical data in addition to zero-measurements should be obtained for all burials in order to investigate the source of these differences. GCM surveys conducted in this work were largely unsuccessful in detecting simulated clandestine burials due to significant conductive noise sources (metal fence, sensors, etc.) and the limited conductivity contrast in the soil. Low conductivity zones were detected over some burials using HCP at an intercoil spacing of 1.18 m, however, confidence in the validity of these responses is low due to the dominating noise sources.

Contents

Nomenclature

Abbreviations

Abbreviation	Definition
AS	Adaptive Subtraction
EI	Electromagnetic Interferometry
EM	Electromagnetic
EMI	Electromagnetic Induction
ERT	Electrical Resistivity Tomography
GCM	Ground Conductivity Meter
GPR	Ground Penetrating Radar
HCP	Horizontal Co-planar
VCP	Vertical Co-planar

Symbols

Symbol	Definition	Unit
$\mathbf{d}$	electric displacement vector or electric flux density	[C/m^2]
$\mathbf{b}$	magnetic flux density vector	[T]
$\mathbf{e}$	electric field strength vector	[V/m]
$\mathbf{h}$	magnetic field intensity	[A/m]
$\mathbf{j}$	electric current density vector	[A/m^2]
ρ	electric charge density	[C/m^2]
t	time	[s]
σ	electrical conductivity	[S/m]
ϵ	dielectric permittivity	[F/m]
μ	magnetic permeability	[N/A^2]
k	wavenumber	[rad/m]
ω	angular frequency	[rad/s]
v	phase velocity	[m/s]
v_0	speed of light	[m/s]
ϵ_r	relative dielectric permittivity	[F/m]
μ_r	relative magnetic permeability	[N/A^2]
λ	wavelength	[m]
θ_c	critical angle	[rad]
f	frequency	[Hz]
δ	skin depth	[m]
B	induction number	[-]
s	intercoil spacing	[m]
z	normalized distance	[-]
σ_a	apparent conductivity	[S/m]

List of Figures

List of Tables

1
Introduction

Criminal homicide investigations often seek the aid of forensic archaeologists to recover evidence which cannot be obtained through traditional law-enforcement approaches (Schultz, 2007). Traditional methods typically involve invasive processes which may result in destruction of the crime scene and forensic evidence, or loss of context and association of evidence. Non-destructive search methods include walking a search area, visual inspection, cadaver dogs and the application of geophysical methods. Forensic investigations, in particular those associated with homicide investigations, require methods which are quick and effective in order to gather evidence and reach conclusions to aid police. Geophysical methods have been repeatedly used for the detection and location of clandestine burials; burials which are located in a remote, unrecorded location, which have been hand-excavated and sit at a depth of <1 m below ground level (bgl) (Pringle et al., 2016). Detection of clandestine burials is much different from graves in graveyards and cemeteries as they lack monumental features and significant material casings such as a casket which make detection much easier (J. D. Hansen et al., 2014). Pre-excavation geophysical surveys can be applied in homicide investigations to help forensic searchers to rapidly identify target regions, and image subsurface features, saving time, money and resources by identifying suspected areas for further invasive investigation (Pringle et al., 2008). The systematic evaluation of the efficacy of geophysical techniques under variable conditions through the use of simulated clandestine burials is essential for improving their applicability and success in the field.

1.1. Literature Review

There are a number of geophysical methods which have been used in previous investigations for the detection of simulated clandestine burials, including ground penetrating radar (GPR) (Schultz and Martin, 2012), electrical resistivity methods (Jervis et al., 2009), electromagnetic induction (EMI) methods (Bigman, 2012), magnetic methods (Pringle et al., 2015), and even seismic methods (Hildebrand et al., 2002). Geophysical methods are often used in conjunction for optimized detection, for example the combined use of EMI and GPR to identify unmarked graves (Nobes, 1999), and the 10 year monitoring study over buried pig cadavers using GPR and bulk ground resistivity surveys (Pringle et al., 2020). In order for forensic units to obtain optimum search results using geophysical techniques, a number of factors must be considered; such as the local burial environment (geology, soil type, weather conditions), the expected depth bgl, the target type, target size and post depositional interval (PDI) or time elapsed since deposition (Pringle, Ruffell, et al., 2012). An in-depth summary and analysis of the efficacy of GPR, EMI, electrical resistivity and magnetic methods in the context of these factors is attached in Appendix D. The conclusions drawn from this report suggest that the optimal combination of methods are EMI with ground conductivity meter (GCM), common-offset GPR and electrical resistivity tomography (ERT).

1.1.1. Ground Penetrating Radar

GPR is the most common geophysical technique used in forensic investigations, and for good reasons: data can be collected quickly and with high resolution in the field. In the past two decades, the number of published case studies using GPR to locate clandestine burials in a forensic context has steadily increased. Typically, antenna frequencies between 400 MHz and 500 MHz are used to perform clandestine burial searches as they strike a balance between resolution and depth of penetration (Schultz, 2007; Schultz and Martin, 2011, 2012). However, 110 MHz to 250 MHz antennas have also been used, and were found to be better in some studies to detect deeper burials, to prevent the collection of data with extensive clutter, and in environments where soil conditions limit the depth of penetration of the signal (Nobes, 1999; Pringle, Ruffell, et al., 2012). Molina et al. (2016) found that 500 MHz GPR was successful in detecting pig cadavers at shallow depths (0.8 m) but of poorer detection quality at greater depth (1.2 m), while 250 MHz was successful for both. The presence of a clandestine burial can be detected using GPR due to a contrast in material properties between the grave and/or the body and the surrounding material. Disturbed soil within the grave, or a break in a soil horizon, has been found to generate prominent features in GPR sections (Johnston, 2021), appearing as a high-amplitude horizontal reflection (Molina et al., 2016). Hansen et al. (2014) found that 1/2 hyperbolic reflections occurred in response to the presence of rapidly dug unmarked graves. The target response of clandestine burials in GPR timeslices was demonstrated by Molina et al. (2016) to form rectangular shaped anomalies. Non-biological items such as clothing or coverings have been found to increase detectability due to increased material contrast (Pringle, Jervis, Hansen, et al., 2012; Pringle et al., 2016; Pringle et al., 2020). Molina et al. (2016) published results which show that skeletonized remains show much lower-amplitude 1/2 hyperbolic reflections as compared to remains in earlier stages of decomposition. Van Schoor et al. (2017) found that the largest contributor to the total burial anomaly was the disturbed burial zone rather than the buried body itself, due to the absence of buried artefacts. Moreover, the detectability of clandestine burials is impacted by their relative position with respect to GPR lines. Schultz and Martin (2011) scanned clandestine burials lengthwise, which resulted in long dense reflections, and when scanned through the chest and abdomen, produced a hyperbolic reflection.

Target detectability and signature have been found to vary significantly over time due to the decreasing contrast between the surrounding soil and the burial (Nobes, 1999). Research conducted by Pringle et al. (2012, 2016, 2020) in the UK monitored the change in GPR response over 10 years, and found that naked cadavers were detected up to 5 years post-burial, producing only a faint hyperbolic reflection after 18 months. In addition to decomposition, soil compaction, in particular in sandy soils, has been found to result in a decrease in contrast over time, reducing anomaly amplitudes and overall detectability (Schultz and Martin, 2012).

Favorable environmental conditions for conducting GPR surveys include regions with sandy soils, which are free of debris, flat and level ground and open areas without dense brush (Schultz, 2007). Non-favourable conditions include soils with high conductivity, i.e. soils which are water saturated, or have high clay and high organic content. Detection in sandy soils might be improved by the presence of a diagnostic soil horizon, as observed by Schultz and Martin (2012) who found that detection of clandestine burials was very limited in sandy homogeneous soil. In some cases, added moisture in the soil may help to highlight clandestine burials. Schultz and Martin (2012) found this to be the case following rainfall events, where increased soil moisture improved the contrast between burials and surrounding soil, and may also have increased decomposition processes resulting in increased soil conductivity surrounding the body. Conversely, Van Schoor et al. (2017) found that heavy seasonal rainfall and other site-specific environmental characteristics negatively impacted the detectability of clandestine burials with GPR.

1.1.2. Electromagnetic Induction

EMI methods measure changes in the apparent conductivity of the subsurface, which is influenced by an object's material properties, size, shape, orientation and porosity/compaction of the soil (Bigman, 2012). The most commonly used EMI instruments in the scope of forensic investigations are ground conductivity meters (GCMs), which can detect the presence of clandestine objects through changes in apparent conductivity associated with changes to soil properties and composition, changes in compaction, the presence of air cavities and disturbed soil in the grave-fill. The signature of the response has been found to vary: Nobes (1999) found anomalous positive responses with negative side lobes, as well as the opposite case; the response depending on the contrast between the contents of the grave and the surroundings. In-situ conductivity data collected over a 2-year period by Pringle et al. (2010), using a lysimeter, found increased conductivities surrounding the burial with respect to background values. However, no published works have confirmed the ability of GCM methods to detect this increase in apparent conductivity due to the release of decompositional fluid. Prehistoric and historic North American burials were successfully detected with GCMs and identified as low apparent conductivity regions (Bigman, 2012). Similarly, France et al. (1992) were able to locate simulated clandestine burials of pig cadavers in the Western US.

A primary advantage to EMI methods is their flexibility for use in different environments and landscapes, and the time efficient manner in which data can be acquired. However, there has been limited use of GCMs in forensic investigations, primarily due to their susceptibility to noise in urban environments (Dick et al., 2015). In particular, issues arise in differentiating anomalies in the presence of background interference from fence boundaries, and local topography (Nobes, 1999). Molina et al. (2016) produced results from a GCM survey in which simulated clandestine burials were very poorly detectable. One disadvantage to EMI methods is that often, and in particular with GCMs, slow sampling rates (measurements per second) result in the limited capacity to detect smaller features, such that burials may not be detected (Bigman, 2012). Although EMI methods may be limited in their ability to identify the exact position of individual burials, they might be useful for rapid characterization of a burial site and work well alongside other methods (Nobes, 1999; Bigman, 2012; Dick et al., 2015). Dick et al. (2015) performed measurements over a burial ground containing unmarked Black Death plague victims with the EM31 GCM and successfully characterized the site quickly and efficiently before performing GPR to obtain a more in-depth characterization of the burials.

1.1.3. Resistivity methods

Resistivity methods measure the resistivity distribution in the subsurface which depends on the electrical parameters of the soil volume of interest. These methods require the galvanic coupling of at minimum four electrodes into the subsurface: two current-electrodes, which introduce current into the ground, and two potential-electrodes which measure the resulting electric potential. A primary advantage to electrical resistivity surveys is that they are very minimally affected by above-ground noise sources due to galvanic coupling with the ground, unlike EMI methods. These methods are often used in environments with high clay content in the soil or in the presence of numerous trees, wherein GPR is unsuitable (Molina et al., 2020). Resistivity methods perform best under consistent environmental conditions; studies have shown (Ellwood et al., 1994; Jones, 2008) that variations in soil moisture content in heterogeneous soil may have a masking effect on burial anomalies.

Resistivity methods predominantly detect the position of clandestine burials based on the detection of decompositional fluids (Jervis et al., 2009; Pringle, Jervis, Hansen, et al., 2012). As was mentioned previously, an increase in conductivity in the vicinity of a burial due to the presence of decompositional fluids can be detected for considerable time post burial (Juerges et al., 2010). The response of a clandestine burial has been shown to be a low-resistivity anomaly, due to the conductive decompositional fluid and increased soil porosity (Pringle, Ruffell, et al., 2012). Monitoring studies performed by Pringle, Jervis, Hansen et al. (2012), Pringle et al. (2016) and Pringle et al. (2020) over a ten year period found that the detection of decompositional fluid conductivity changes significantly over time. In particular, after 4 years, "naked" pig cadavers were very difficult to identify, which is thought to be due to the migration of fluids overtime.

1.1.4. Taphonomic considerations

In forensic geophysical investigations a general taphonomic knowledge is required, as the decompositional state in which the cadaver resides, in addition to the length of time since burial, are factors that largely impact the geophysical response of the instrument. The decomposition of all organic resources, including human bodies, is mediated by three primary factors: the community of decomposers which have access to the body, the environment in which the burial is in and the biophysiochemical properties of the organic material, the body itself (Schotsmans et al., 2017; Nienaber et al., 2022). The stages of decomposition have been presented by numerous authors (Reed, 1958; Payne, 1965; Galloway et al., 1989; Vass et al., 2002; Megyesi et al., 2005; Simmons et al., 2010). Galloway et al. (1989) performed studies in the desert of Arizona and presented the first decompositional stages with descriptive subcategories, consisting of fresh, early decomposition, advanced decomposition, skeletonized and decomposition of skeletonized remains. However, these stages are not necessarily distinct from one another, and their length in time is highly variable; the authors themselves (Galloway et al., 1989) recognize that this method might result in an overestimation of post-mortem interval in many cases. This variability is due to the influence of temperature and moisture which are found to have a strong control over decomposition rates (Hayman and Oxenham, 2016). In general, it is accepted that higher temperatures will increase the rate of decomposition, while cooler temperatures will decrease the rate of decomposition (Schotsmans et al., 2017). However, soil texture, moisture and oxygen content in the soil environment exercise strong control over decomposition processes, resulting in very complex relationships between the soil environment and rate of decomposition. Carter et al., (2010) found that grave soil moisture content can modify the relationship between temperature and rate of decomposition. Though clay soils have higher water-holding capacity than sandy soils promoting rapid decomposition, in wet, sandy soils, greater cadaver decomposition occurs than in wet fine-textured soil, due to the lack of gas diffusivity in the latter (Carter et al., 2010). There are numerous intrinsic properties of human remains which also influence the decomposition, such as drug use, age, sex and mass, due to their effects on the nutritional quality of the remains (Schotsmans et al., 2017). Simmons et al. (2010) determined through comparative analysis that the presence or absence of insects has the greatest control over decomposition. Given the high variability of influences on the decompositional stage, predicting the state of buried cadavers based on post-mortem intervals is often inaccurate and difficult to predict.

The vast majority of past works performed investigations over simulated clandestine burials containing buried pig cadavers (Schultz and Martin, 2012; Pringle et al., 2020; Molina et al., 2016; Booth and Pringle, 2016). Though pig cadavers do provide a close proxy to human remains, the use of animal models is not ideal as studies have shown that a significant taphonomic difference exists between the two species (Connor et al., 2018; Knobel et al., 2019). Hayman and Oxenham (2016) determined that variations in fatty acid composition and nutrient levels in pig and human tissue result in differences in decomposition rates. This is of particular importance when considering the response due to decompositional fluids, which we might expect from EMI and resistivity methods.

1.2. Motivation

The following work was conducted at the Amsterdam Research Initiative for Sub-surface Taphonomy and Anthropology (ARISTA) test facility, in Amsterdam, The Netherlands. This research facility is the first of its kind in Europe, having been instated in 2017. The sites primary use is to investigate, under known conditions, the taphonomy of buried human remains. The site is located in the province of North-Holland which from the early 1600s onward was drained with mills and filled up with sediment from nearby lakes, consisting of sand and peaty soil (Oostra et al., 2020). This soil fill which is not native to the area makes up the top 1 m of the subsurface. ARISTA consists of a 32 x 18 m plot of land, surrounded by a large 3-m-high metal fence, which extends 1 m into the ground. During site construction the terrain was leveled and the large vegetation was removed, while smaller pieces of vegetation were left in-situ to preserve a "natural state". In a soil analysis conducted by Buijs and Skinner (2021), the terrain at the site was found to consist of a 1-m-thick layer of homogeneous sand, covered by 10-20 cm of humus-rich topsoil, this being the soil fill moved to the area in the early 1600s. The ground water table is very shallow, at approximately 70 cm depth, tilting down towards the north-west direction (Oostra et al., 2020). At ARISTA, cadavers donated to science are buried, and have often undergone significant hospital treatments prior to their passing. This is an important consideration as the effects of hospital treatments such as radiation and high levels of opiates on decomposition are unknown. Although systematic scientific studies at the ARISTA facility are ongoing, no results have been published. Few insects appear to be present, even during the initial stages of decomposition, potentially suggesting that the toxicity of the cadavers is impacting the taphonomy and decompositional environment. At present these are anecdotal conclusions based on personal observation (Nienaber, personal comm.).

The taphonomical situation of a particular environment is always unique (Nienaber et al., 2022), and the nature of the Dutch environment is, in itself, complex and variable. A large proportion of The Netherlands consists of heavily modified natural environments and man-made areas which have been artificially drained and filled-in (Römkens and Oenema, 2004). In some regions the land has been reclaimed from the sea. As a result many locations, including the ARISTA test facility, consist of a mix of natural, modified and man-made soil environments. The complexity of this aspect and how it might interact with buried cadavers is not yet fully understood, however the taphonomical "sequence" and the manner in which bodies decompose in the soil seems to differ in Dutch environments from what is described in the general literature. It should be noted that most of the studies that attempt to establish and define a "normal" taphonomy for buried human bodies are based on animal models and were conducted in locations that have a different (warmer) climate and soil composition (Reed, 1958; Payne, 1965; Galloway et al., 1989; Vass et al., 2002). From preliminary observations at ARISTA and from other documented cases in the Netherlands, it appears that the decompositional progression of buried human bodies are delayed when compared to other taphonomical and decomposition studies in the general literature (Nienaber, personal comm.). From preliminary observations it is suggested that the specific environment and climate in the Netherlands acts to "preserve" the buried bodies. This is thought to come from the unique soil environment in combination with a cooler climate, high water table and the possible effects of medical treatments pre- and post-mortem (Nienaber, personal comm.). Seasonal variation at ARISTA has not been systematically accounted for and various other taphonomical influences are still being studied. From occasional case reports and other anecdotal evidence it seems as if a similar taphonomy is present in coastal dune environments in the United Kingdom and Belgium (Nienaber, personal comm). These dunes are, likewise, characterized by marine sands and a cool-wet climate. The consequence for this work is that the detection of decompositional fluids, which have been measured using geophysical methods in different environments, will likely not be a factor in the detection of burials at ARISTA. Additionally, the preservation of the buried human bodies in the environment for this study suggests that the post-depositional interval (PDI) will be unlikely to follow the same trends summarized previously in different soil environments elsewhere in the world.

In a previous thesis performed at ARISTA, Hansen (2019) conducted GPR measurements using a 250 MHz pulseEKKO GPR over a single burial. The results of this investigation contained a high degree of interference from the surrounding metal fences and metal plate near the burial, and thus significantly reduced the authors ability to interpret the data. Hansen (2019) recommended the use of a 500 MHz antenna in order to provide higher resolution measurements, and to reduce the depth of penetration, which was three times deeper than the maximum burial depths.

In this thesis, in addition to the work conducted at the ARISTA test facility, zero-measurement data was obtained at a new test site in Almere, The Netherlands, which will be used by the Dutch national police and the Netherlands Forensic Institute (NFI) to conduct geophysical surveys over buried cadavers. The Almere site is located in a retired correctional facility yard and consists of predominantly grass covered, sandy, man-made soil. Thus, much like the ARISTA test site, the Almere site is characteristic of soil environments most common in the Netherlands. The site consists of two rectangular fields with dimensions 30 x 50 m, surrounded on one side by two layers of tall metal fences and the correctional facility building on the other side. In the future, a minimum of two burials are planned on this site, which will be dug alongside two empty graves for comparison studies. These burials will be used for both geophysical investigations and cadaver dog training, providing an important opportunity for the Dutch national police and the NFI to further investigate clandestine burial detection methods in a controlled environment.

GPR, EMI and resistivity methods are the most prevalent geophysical survey methods used in the detection of clandestine burials in the literature, as summarized above, and presented in depth in Appendix D. Resistivity methods are not applied in this thesis because their real-world applicability to police investigations in The Netherlands is very low. This is primarily due to labor-intensive setup, requirement for galvanic coupling with the ground and extensive equipment requirements. In addition, the unique decompositional setting expected from soil environments in The Netherlands is likely to negatively influence the applicability of resistivity methods. As mentioned previously resistivity methods are thought to rely on the detection of decompositional fluids in order to detect burial positions. Given the unique homogeneous, cool, damp soil environment and state of the cadavers at ARISTA, decompositional fluids are unlikely to be present to a significant degree. Both GPR and GCM surveys are more flexible, can cover large areas quickly, and work in a variety of environments. Therefore, these methods are most suitable for use in forensic investigations concerning buried bodies by law enforcement in The Netherlands. This thesis therefore involves the application of GPR and EMI GCM methods for the detection of clandestine burials. The choice of 250 MHz and 500 MHz GPR antennas for this investigation was intended to test their effectiveness, given recommendations and debates in the literature and based on the recommendations from works performed at the ARISTA facility. The comparison between the contrasting resolutions and penetration depths of both antennas in the environment unique to The Netherlands will inform the Dutch law enforcement institutions on the correct selection of antenna in real field investigations. The CMD-MiniExplorer is the GCM instrument of choice for this investigation given its capacity for fast acquisition in the field, and high potential as a method to rapidly characterize a large area in the context of forensic investigations.

1.2.1. Research Questions

The aim of this investigation is to provide information to Dutch law enforcement institutions and the NFI on the efficacy of GPR and GCM surveys in producing detectable signatures over the location of simulated clandestine burials at ARISTA, and to present the character of these geophysical signatures. First, this investigation will provide a quantitative analysis on the selection of acquisition and survey parameter settings, for GPR (antenna frequency, instrumentation and survey grid alignment), and for GCM (coil configuration and survey line spacing) to provide the greatest likelihood of burial detection. Second, this work aims to provide qualitative analysis of the impact of soil moisture and noise sources at the field site on detectability, which will provide very important context for law enforcement when performing forensic investigations. Last, this work will provide recommendations on the use of particular processing and visualization techniques, such as direct-wave removal techniques in GPR and correction procedures in GCM, through qualitative analysis of their success in aiding the detection of simulated clandestine burials at ARISTA. In summary, the central research question which this work aims to answer is the following:

Can GPR and GCM geophysical surveys be used to identify the location of clandestine burials, and if so, what are the geophysical signatures of these features?

The following sub-questions will help to guide the investigation of the central research question in order to better inform the Dutch police and will be examined for both GPR and GCMs.

1. How can the detectability of simulated clandestine burials be influenced by acquisition and survey parameter settings?
   (a) **GPR**: Which is more effective, 250 MHz or 500 MHz antenna? How does the orientation of the survey grid relative to the alignment of the burials impact the detectability of the target? How does the instrument used influence the detectability of the target?
   (b) **GCM**: Which is more effective, HCP or VCP configuration? What is a sufficient line spacing, 0.25 m or 0.5 m?
2. How does the survey environment, which is unique to The Netherlands, affect the detectability of simulated clandestine burials for both **GPR** and **GCM**?
   (a) How does the presence or absence of moisture in the soil impact the detectability of simulated clandestine burials?
   (b) How does the presence or absence of noise sources impact the detectability of simulated clandestine burials?
3. How can the data be improved through processing and visualization techniques, and what is the effect of these steps on the successful detection of simulated clandestine burials?
   (a) **GPR**: What are the effects on the data of applying airwave subtraction, average background subtraction, and adaptive subtraction methods? How does visualizing GPR data in lines versus grid display affect the detectability of the targets?
   (b) **GCM**: What are the effects on the detectability of the targets from applying LIN correction and elevation correction procedures?

This thesis will have the following structure: In Section 2 a theoretical framework will be constructed providing a brief overview and background on electromagnetic theory, GPR and GCM equipment, methods and limitations. The specific methodologies applied in this work are then presented in Section 3 including a summary of the survey site, survey instruments and design, as well as the data processing techniques used. The results obtained from GPR acquisition and processing are then presented and subsequently discussed in Section 4 and Section 5, respectively. In Section 6 the results of GCM surveys will be presented, and a discussion of these results are provided in the following Section 7. Lastly, in Section 8 the conclusions drawn from this thesis are presented, providing an outlook towards future studies and recommendations thereof.

2
Theory and Equipment

2.1. Electromagnetic theory

Electromagnetic (EM) geophysical methods are those which measure the ground's response to the presence of an EM surface field resulting from a time-dependent EM source. The goal of such methods is to collect information about the electrical properties of the subsurface. In order to successfully implement EM geophysical methods in the field, first a strong understanding of EM theory must be established. Here a brief overview of EM theory is presented, with particular emphasis being placed on those concepts which are most essential to this thesis. More extensive theory can be found in books such as Annan (2005), Reynolds (2011) and Knödel et al. (2007).

EM waves are made up of two orthogonal vector components, the electric field strength ($\mathbf{e}$) and the magnetic field intensity ($\mathbf{h}$). The two orthogonal vector components are located in a plane perpendicular to the direction of travel. Maxwell's equations provide an all encompassing mathematical description of the physics of EM fields. Maxwell's equations are the following:

$$\nabla \cdot \mathbf{d} = \rho \tag{2.1a}$$

$$\nabla \cdot \mathbf{b} = 0 \tag{2.1b}$$

$$\nabla \times \mathbf{e} = -\frac{\partial \mathbf{b}}{\partial t} \tag{2.1c}$$

$$\nabla \times \mathbf{h} = \mathbf{j} + \frac{\partial \mathbf{d}}{\partial t} \ , \tag{2.1d}$$

where
$\mathbf{d}$ = electric displacement vector or electric flux density (C/m^2)
$\mathbf{b}$ = magnetic flux density vector (T)
$\mathbf{e}$ = electric field strength vector (V/m)
$\mathbf{h}$ = magnetic field intensity (A/m)
$\mathbf{j}$ = electric current density vector (A/m^2)
ρ = electric charge density (C/m^2)
t = time (s).

These equations form the building blocks for all classical EM theory. In particular, Equation 2.1c and 2.1d elucidate that a magnetic field induces an electric field, and vice versa, and thus these equations provide the basis for self-sustaining EM radiation, which consist of disturbances to the EM field moving through media at the speed of light. EM radiation has a frequency range from atmospheric micropulsations ($<$ 10 Hz), through the radar frequency bands (10^8 to 10^{11} Hz) up to and beyond 10^{24} Hz, the highest frequencies consisting of x-rays and gamma rays.

The constitutive equations relate the physical properties of materials to EM fields, providing an average behaviour description of how the material responds to the application of an EM field. They are the following:

$$\mathbf{j} = \tilde{\sigma}\mathbf{e} \tag{2.2}$$

$$\mathbf{d} = \tilde{\epsilon}\mathbf{e} \tag{2.3}$$

$$\mathbf{b} = \tilde{\mu}\mathbf{h} \ , \tag{2.4}$$

where $\tilde{\sigma}$ is the electrical conductivity, $\tilde{\epsilon}$ is the dielectric permittivity and $\tilde{\mu}$ is the magnetic permeability.

In the context of most geophysical investigations these quantities are taken as field-independent scalar quantities, which is rarely a true assumption, but the complexity of the non-linearity of these quantities and their dependence on field strengths is beyond the scope of virtually all practical issues (Annan, 2005). Combining the constitutive relationships and Maxwell's equations provides the foundations of EM theory.

One very interesting and important characteristic of EM radiation is that depending on the relative magnitude of losses as the disturbance moves through a medium, the radiation may take on different forms: diffusion, or propagating as waves. These different manifestations of EM radiation can be examined by rewriting Maxwell's equations to eliminate the magnetic fields, combining Faraday's law Equation 2.1c and Ampere's law, Equation 2.1d and plugging in the constitutive equations. First we simplify Maxwell's equations using the constitutive equations to obtain:

$$\nabla \cdot \mathbf{e} = \frac{\rho}{\epsilon} \tag{2.5}$$

$$\nabla \cdot \mathbf{h} = 0 \tag{2.6}$$

$$\nabla \times \mathbf{e} = -\mu \frac{\partial \mathbf{h}}{\partial t} \tag{2.7}$$

$$\nabla \times \mathbf{h} = \sigma \mathbf{e} + \epsilon \frac{\partial \mathbf{e}}{\partial t} \; . \tag{2.8}$$

Now, taking the curl of Equation 2.7 and combining it with Equation 2.8 to eliminate the magnetic fields, we obtain the transverse vector wave equation involving only $\mathbf{e}$:

$$\nabla^2 \mathbf{e} - \mu\sigma \frac{\partial \mathbf{e}}{\partial t} - \mu\epsilon \frac{\partial^2 \mathbf{e}}{\partial t^2} = 0 \; , \tag{2.9}$$

which can also be derived for the magnetic field, obtaining the following which only involves $\mathbf{h}$:

$$\nabla^2 \mathbf{h} - \mu\sigma \frac{\partial \mathbf{h}}{\partial t} - \mu\epsilon \frac{\partial^2 \mathbf{h}}{\partial t^2} = 0 \; . \tag{2.10}$$

Equation 2.9 and Equation 2.10 are also referred to as "lossy wave equations" as they describe EM signals which propagate as waves which are subject to diffusion. The first term, containing ∇^2 is called the Laplacian. The 2nd term containing the first order time derivative controls the diffusive behaviour of the EM signal. The 3rd term containing the second order time derivative is the energy conservation term.

A quasi-static regime, is one in which time-variations in the signal are assumed to be much slower than the charge relaxation time. Thus, in a quasi-static regime the diffusive term is by definition much larger than the conservation term, and thus $\mathbf{e}$ and $\mathbf{h}$ behave according to

$$\nabla^2 \mathbf{e} - \mu\sigma \frac{\partial \mathbf{e}}{\partial t} = 0 \tag{2.11}$$

and

$$\nabla^2 \mathbf{h} - \mu\sigma \frac{\partial \mathbf{h}}{\partial t} = 0 \; , \tag{2.12}$$

also known as the heat equation, where the rate of diffusion is controlled by the term $\mu\sigma$. For most materials, $\mu = \mu_0 = 4\pi \times 10^{-7}$ H/m, while σ may vary over many orders of magnitude. Thus σ is the property which dictates the diffusive properties of EM fields in a quasi-static regime.

Conversely in the so-called wave regime, the opposite is true, the diffusive term is by definition much smaller than the conservation term and thus $\mathbf{e}$ and $\mathbf{h}$ behave according to the classic wave equation

$$\nabla^2 \mathbf{e} - \mu\epsilon \frac{\partial^2 \mathbf{e}}{\partial t^2} = 0 \tag{2.13}$$

and

$$\nabla^2 \mathbf{h} - \mu\epsilon \frac{\partial^2 \mathbf{h}}{\partial t^2} = 0 \; , \tag{2.14}$$

wherein energy is conserved and $\mathbf{e}$ and $\mathbf{h}$ propagate as waves. Under the wave regime the properties of the waves depend on $\mu\epsilon$. However, as mentioned previously in most materials the approximation $\mu = \mu_0$ can be taken, while ϵ may vary over many orders of magnitude. Thus ϵ is the property which dictates the wave properties of EM fields.

The same relationships can be derived in the frequency-domain using the Fourier transform with an $e^{i\omega t}$ time dependence. Given that the derivative of $e^{i\omega t}$ is $i\omega e^{i\omega t}$ with respect to time, Equation 2.9 and Equation 2.10 above can be transformed to the frequency domain by replacing $\frac{\partial}{\partial t} \rightarrow i\omega$ and $\frac{\partial^2}{\partial t^2} \rightarrow -\omega^2$ obtaining

$$\nabla^2 \mathbf{E} + k^2 \mathbf{E} = 0 \tag{2.15}$$

and

$$\nabla^2 \mathbf{H} + k^2 \mathbf{H} = 0 \; , \tag{2.16}$$

where the wavenumber $k = \sqrt{\omega^2 \mu\epsilon - i\omega\mu\sigma}$. Equation 2.15 and Equation 2.16 are the Helmholtz vector equations, wherein the properties of $\mathbf{E}$ and $\mathbf{H}$ depend on k.

In the frequency domain the quasi-static regime occurs when the properties of the EM signal are dominated by conductivities, thus $\sigma >> \omega\epsilon$. In this regime the wavenumber can be approximated as

$$k \approx \sqrt{-i\omega\mu\sigma} \; . \tag{2.17}$$

In this case the wavenumber k still has both real and imaginary components and the signal therefore experiences both attenuation and oscillations and is controlled by $\mu\sigma$. Conversely in the wave regime, the dielectric permittivity dominates, thus $\sigma << \omega\epsilon$. In this case the wavenumber can be approximated as

$$k \approx \sqrt{\omega^2 \mu\epsilon} \; , \tag{2.18}$$

here the wavenumber only contains real components and is controlled by the terms $\mu\epsilon$.

From the Helmholtz equations in Equation 2.15 and Equation 2.16 the general solution for a plane-wave in homogeneous medium can be derived. First, assuming that the wave is propagating along the z-direction, the $\mathbf{E}$ and $\mathbf{H}$ fields must lie in the xy-plane, thus Equation 2.15 simplifies to

$$\frac{\partial^2 \mathbf{E}}{\partial z^2} + k^2 \mathbf{E} = 0 \; , \tag{2.19}$$

where $\mathbf{E} = \mathbf{E}(z, \omega)$ does not depend on x and y. Equation 2.19 has the general solution of the form

$$\mathbf{E} = \mathbf{E}_0^- e^{i(kz - \omega t)} + \mathbf{E}_0^+ e^{i(kz + \omega t)} \; , \tag{2.20}$$

where $\mathbf{E}_0^-$ and $\mathbf{E}_0^+$ are the amplitudes of the downgoing and upgoing waves respectively, $e^{i\omega t}$ controls the temporal phase and where the wavenumber is defined as

$$k = \alpha - i\beta \; . \tag{2.21}$$

The values of α, the real component of the wavenumber k and β, the imaginary component, must be larger than or equal to zero, and given by

$$\alpha = \omega\left(\frac{\mu\epsilon}{2}[(1 + \frac{\sigma^2}{\epsilon^2\omega^2})^{\frac{1}{2}} + 1]\right)^{\frac{1}{2}} \tag{2.22}$$

and

$$\beta = \omega\left(\frac{\mu\epsilon}{2}[(1 + \frac{\sigma^2}{\epsilon^2\omega^2})^{\frac{1}{2}} - 1]\right)^{\frac{1}{2}} \; . \tag{2.23}$$

Thus, the general solution for the planewave in a homogeneous medium is given by

$$\mathbf{E} = \mathbf{E}_0^- e^{\beta z} e^{i(\alpha z - \omega t)} + \mathbf{E}_0^+ e^{-\beta z} e^{-i(\alpha z + \omega t)} \; . \tag{2.24}$$

There are two very important behaviours dictated in Equation 2.24 which are worth mentioning. First, that $e^{\pm i\alpha z}$ controls the oscillatory behaviour (i.e. wavelength) and the velocity of the propagating wave, while $e^{\pm \beta z}$ controls the decay behaviour (i.e. attenuation) of the propagating wave. The magnetic field $\mathbf{H}$ has a general solution of the same form as in Equation 2.24.

Attenuation is the rate at which an EM wave experiences amplitude loss as it propagates through a medium. The attenuation is defined by β, the attenuation coefficient where the attenuation for a down-going plane-wave would be given by

$$A(z) = A_0 e^{\beta z} \ , \tag{2.25}$$

where A is the absolute amplitude, and A_0 the absolute amplitude at $z = 0$ m. The skin depth is the distance a wave travels before it's amplitude has decayed by $\frac{1}{e}$, the reciprocal of the decay constant β. Thus the skin depth is defined as

$$\delta = \frac{1}{\omega}(\frac{\mu\epsilon}{2}[(1 + \frac{\sigma^2}{\epsilon^2\omega^2})^{\frac{1}{2}} - 1])^{\frac{1}{2}} \ . \tag{2.26}$$

Under the quasi-static regime, wherein $\epsilon\omega << \sigma$, the skin depth can be approximated as

$$\delta = \frac{1}{\beta} = \sqrt{\frac{2}{\omega\mu\sigma}} \ . \tag{2.27}$$

While, under the wave-regime approximation where $\epsilon\omega >> \sigma$, the skin depth can be approximated by

$$\delta = \frac{1}{\beta} = \frac{2}{\sigma}\sqrt{\frac{\epsilon}{\mu}} \ . \tag{2.28}$$

The phase velocity v is the speed at which waves oscillating at a particular frequency propagate, and depends on α, wherein

$$v = \frac{\omega}{\alpha} = (\frac{\mu\epsilon}{2}[(1 + \frac{\sigma^2}{\epsilon^2\omega^2})^{\frac{1}{2}} + 1])^{-\frac{1}{2}} \ . \tag{2.29}$$

Under the quasi-static regime, wherein $\epsilon\omega << \sigma$ the phase velocity simplifies to

$$v = \sqrt{\frac{2\omega}{\mu\sigma}} \ . \tag{2.30}$$

Conversely in the wave regime, wherein $\epsilon\omega >> \sigma$ the phase velocity is given by

$$v = \frac{1}{\sqrt{\mu\epsilon}} \ . \tag{2.31}$$

Lastly, the wave impedance can be derived from taking the ratio between the transverse components of the electric and magnetic fields supported by an EM planewave. For a downward propagating planewave for example, the impedance Z_{xy} is given by

$$Z_{xy} = -\frac{\mathbf{E}_x}{\mathbf{H}_y} = \frac{\omega\mu}{k} \ . \tag{2.32}$$

Under the quasi-static regime, wherein $\epsilon\omega << \sigma$, and thus $k \approx \sqrt{-i\omega\mu\sigma}$ then the impedance simplifies to

$$Z_{xy} = \frac{\omega\mu}{\sqrt{-i\omega\mu\sigma}} = \sqrt{\frac{i\omega\mu}{\sigma}} \ . \tag{2.33}$$

Under the wave regime, wherein $\epsilon\omega >> \sigma$ and $k \approx \omega\sqrt{\mu\epsilon}$ then the impedance simplifies to

$$Z_{xy} = \frac{\omega\mu}{\omega\sqrt{\mu\epsilon}} = \sqrt{\frac{\mu}{\epsilon}} \ . \tag{2.34}$$

The behaviour of the phase velocity v and the attenuation coefficient β for a range of frequencies in a simple medium with constant permittivity, conductivity and permeability is shown in Figure 2.1. The transition from a quasi-static regime to a wave regime approximation of EM radiation occurs when electric currents shift from conduction, or free charge dominant behavior to displacement, or constrained charge dominant behavior. The transition frequency at which the behavior changes for a very simple material is given by

$$f_t = \frac{\sigma}{2\pi\epsilon} \,. \tag{2.35}$$

The quasi-static regime, which describes a diffusive EM field assumes that time variations in the signal must be much slower than the charge relaxation time, which is given by $\frac{\epsilon}{\sigma}$. When the time variations are much faster than the charge relaxation time, then the field behaves as propagating waves, in the wave regime, with a frequency independent exponential decay, which can be seen in Figure 2.1.

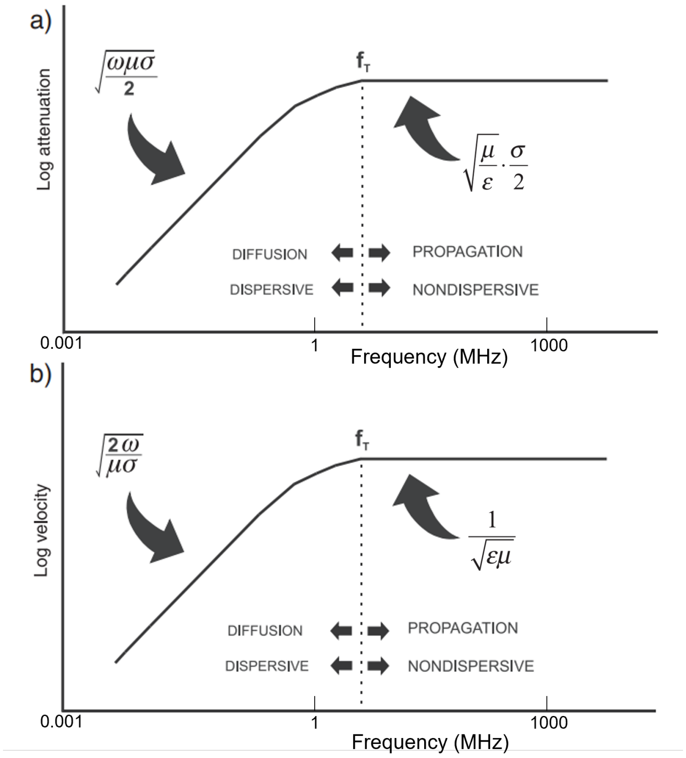

Figure 2.1: Variation of a) attenuation and b) phase velocity in a simple medium with constant material properties due to increasing frequency of an applied field. Adapted from Annan (2005, 2009).

Both the phase velocity and the attenuation behave very similarly as is demonstrated in Figure 2.1. At low frequencies, both properties depend on $\sqrt{\omega}$, whereas at high frequencies the properties become independent of frequency, under the assumption that the material properties remain independent of frequency themselves. The result of this difference in behavior is that at low frequencies ($\omega\epsilon << \sigma$), EM fields diffuse into materials under the so-called quasi-static regime. This behavior is essential to GCM methods. What occurs is that the signal becomes smeared out following transmission because both the attenuation and phase velocity are frequency dependent. Again, the mathematical form of the phase velocity, v and attenuation, β in the quasi-static regime are the following:

$$v = \sqrt{\frac{2\omega}{\mu\sigma}} \tag{2.36}$$

and

$$\beta = \sqrt{\frac{\mu\sigma\omega}{2}} \,. \tag{2.37}$$

While conversely at high frequencies, wherein ($\omega\epsilon >> \sigma$) EM fields propagate as waves in a medium. This is the state in which GPR methods are applied. In the wave regime all frequency components of the signal are said to travel at the same velocity, and also suffer the same attenuation effects, traveling as an intact signal with constant shape. At high frequencies the wave properties can be expressed as

$$v = \frac{1}{\sqrt{\epsilon\mu}} \tag{2.38}$$

and

$$\beta = \sqrt{\frac{\mu}{\epsilon}}\frac{\sigma}{2} \ . \tag{2.39}$$

A few things should be noted in Figure 2.1. First, both the attenuation and phase velocity are plotted on a logarithmic scale, which suggests that the distinction between propagation and diffusion behaviour of EM radiation is not as clean cut as it appears with the plateau, and there must exist a zone in which both behaviours might play a significant role. Thus, neither GPR or GCM methods are without contributions from both propagating and diffusive EM fields. Secondly, the relationships described in Equation 2.36 to 2.39 and in Figure 2.1 rely on the aforementioned assumption that the material properties are constant, or in other words frequency-independent. This assumption is not always valid, for instance water has conductivity σ and permittivity ϵ which exhibit frequency dependent effects which are measurable well below 1 GHz, i.e. at low frequencies (Slob, personal comm.). Therefore, the relationships presented in Figure 2.1 are useful for the purpose of examining the distinction in EM field behaviour for GPR and GCM methods through the velocity, v and attenuation, β, of EM fields, however should be in general used with caution due to the heavy assumptions they rely on.

2.2. Ground Penetrating Radar

GPR is a high resolution geophysical method based on the propagation of high frequency EM waves, with central frequency ranging between 10 to 3000 MHz. GPR systems consist of a signal generator, one or more transmitting and receiving antennae and a control console which manages the signal generation and recordings (Reynolds, 2011). The basic principle of operation in GPR is the transmitting antenna generates a wavetrain of radiowaves which propagates away from the antenna forming a broad beam. The *antenna frequency* refers to the middle frequency of the broadband signal emitted by the transmitter antenna. The transmitter generates pulses of radiowaves at a *pulse repetition rate* which is unique to a particular instrument. The receiving antenna scans the surroundings for a fixed *time window* which is set by the user to match the two-way travel time range for the desired depth of investigation. The scan is then displayed on the video screen in the form of a *radargram* containing the obtained signals at the receiver displayed as a function of two-way travel time. The radar signal contains an amplitude and polarity versus two-way travel time. Figure 2.2 below from Reynolds (2011) depicts a schematic of an example received waveform at the receiver, and the output which would be recorded by the system.

The source pulse consists of more than a single wavelength, and thus has a complex wave shape, as can be seen schematically in Figure 2.2. The resulting reflection has an equally complex wave shape due to ground coupling, which affects the shape and duration of the down-going wavelet. It can be seen in Figure 2.2 that the ground coupled signal has considerably larger amplitude then the recorded transmitted source pulse. The reflected wavelet has a pulse-broadened duration due to attenuation of the high frequency components, and arrives at a time lag away from the source and ground coupled signals. A reflection event in the radar data does not consist of single wavelet, but of several.

Putting the visualization in Figure 2.2 into mathematical terms requires a background in real-time signal processing fundamentals. Annan (2005) provide the most simplistic model for the received signal $r(t)$, as the antenna system impulse response $a(t)$, convolved in the time domain with the impulse response of the ground $g(t)$ and the transmitter electronics output $p(t)$ given by

$$r(t) = g(t) * a(t) * p(t) \ , \tag{2.40}$$

where the convolution is represented by $*$. In the frequency domain the convolution is a multiplication of transfer functions shown here

$$R(\omega) = G(\omega)A(\omega)P(\omega) \ , \tag{2.41}$$

wherein ω represents the angular frequency.

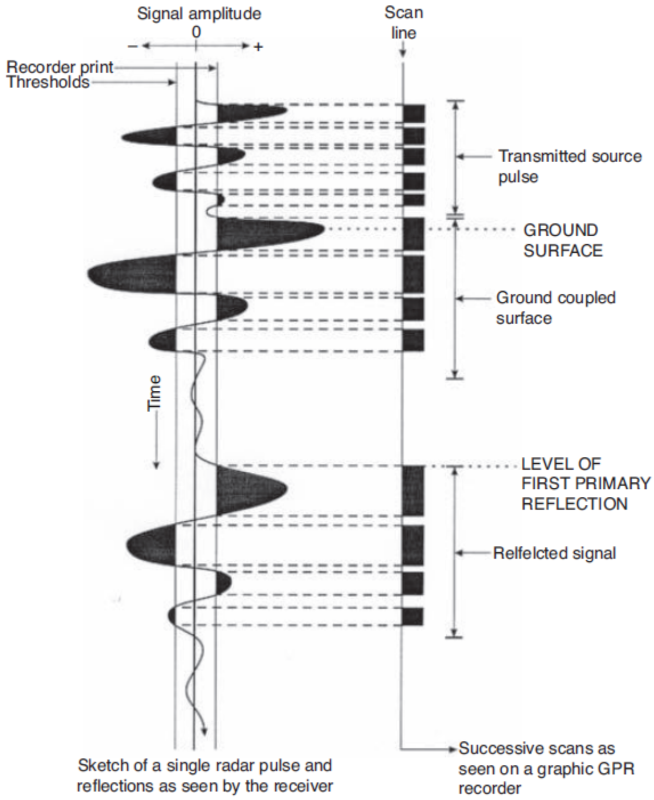

Figure 2.2: Schematic diagram from Reynolds (2011) depicting an example of the translation of a received waveform from a single GPR scan on to a graphic recorder output.

In GPR the desired output is the ground's response $g(t)$, without contributions from the antenna response and the transmitter excitation characteristics. This extraction of the desired impulse response is performed through deconvolution. In theory, if both $P(\omega)$ and $A(\omega)$ were without nulls in the data, the deconvolution to obtain $g(t)$ could be performed as shown here:

$$g(t) = IFT[\frac{R(\omega)}{A(\omega)P(\omega)}] , \tag{2.42}$$

however, in GPR data nulls occur often at zero, and other frequencies in the spectrum. The solution is making the combined excitation and antenna signal mimic a delta function, to perfectly replicate the ground response. Obviously, physical realities of the system limit this from being achieved, however engineers have established a system response which can be reduced to a very compact time duration wavelet $w(t)$ (Annan, 2005). Thus, the received signal takes the form

$$r(t) = g(t) * w(t) . \tag{2.43}$$

For practical GPR applications, the vast majority of the time $r(t)$ is used with great success. There are still additional methods which can be used in post-processing GPR data through deconvolutional processes, namely filtering using airwave measurements or direct-wave removal through adaptive subtraction.

2.2.1. Wave properties

In GPR the observable character of EM fields are the EM wave properties. The key wavefield properties in GPR are the phase velocity, v, the attenuation, β, and EM impedance, Z. The material composition and water content of subsurface materials exert the greatest control over their properties and thus also the velocity, attenuation and impedance of EM waves propagating through the material.

The phase velocity of EM waves, v, in a low-loss host material, which was derived previously in Equation 2.38 is inversely dependent on dielectric permittivity, ϵ, and the magnetic permeability, μ of the host material, independent of angular frequency, ω under the assumption that the material properties remain constant. There are numerous factors which influence the strength of EM signals as they propagate through materials in the subsurface including attenuation, spherical spreading of energy, reflection and transmission loses at boundaries, scattering of energy and absorption (Annan, 2005). However the fundamental cause of energy loss is attenuation, β. As was demonstrated in Equation 2.39 attenuation is a function of dielectric permittivity, ϵ, electrical conductivity, σ, and magnetic permeability, μ. In high conductivity materials radio-waves will be attenuated to a high degree. EM impedance, Z can be understood from analogy with acoustic waves, wherein the magnetic field intensity is analogous with material displacement, and the electric field is considered equivalent to the applied mechanical stress (Annan, 2005). The EM impedance was derived previously in Equation 2.34 for low-loss materials under the wave regime, where the impedance contrast depends on the dielectric permittivity and magnetic permeability of the materials. Water has a relative permittivity $\epsilon_r = 80$, which is much larger than all other natural materials. For instance the relative permittivity of air $\epsilon_r = 1$ and dry sand, $\epsilon_r = 3 - 5$. Thus, the presence of water in media has a large impact on the propagation velocity, and impedance of radar waves in a medium.

The behavior of EM fields across an interface between two materials is described by the Fresnel reflection (R) and transmission (T) coefficients. These quantities depend on the impedance of the material, Z, and the admittance, Y, the inverse of impedance, of the material, two complex values. Therefore, both R and T are complex and as a result, the reflection and transmission of EM waves at a material boundary always causes deformation of the incident wavelet. The most important conclusion is that in order for there to be a response measurable at the GPR instrument, there must exist an impedance contrast between the ground and the material/object being detected. In the case of a low-loss material, assuming that $\mu = \mu_0$, the impedance depends only on the dielectric permittivity of the materials, and thus the impedance contrast exists if a contrast in dielectric permittivity exists.

2.2.2. Wave propagation

Looking at a localized high frequency EM source deployed on the surface of the ground, as portrayed in Figure 2.3, in the air, the incident and reflected waves form an up-going spherical wave. In the ground the transmitted signal is separated into two parts, a planar wavefront traveling at the critical angle and a spherical wave penetrating into the ground. The head-wave is a conical wave propagating into the ground at the critical angle. It has a characteristic linear phase front as it travels over the surface of the earth and is continuously radiating down into the subsurface at the critical angle. The head-wavefront connects the direct-airwave to the spherical groundwave, stopping at the point corresponding to the critical angle, θ_c. The direct-airwave propagates in the horizontal direction just above the surface. The direct-groundwave on the other hand is a wave travelling just below the surface propagating horizontally. The direct-groundwave propagates much beyond the critical angle θ_c and thus does not transmit as a propagating wave into the air. Instead, at the air-ground interface, the spherical groundwave enters the air as an evanescent field. The signal ray paths for the direct-airwave, groundwave, reflected and critically refracted wave are shown in Figure 2.4. the direct-groundwave and direct-airwave make up the direct-wave.

2.2.3. Common-offset reflection profiling

For the investigation of lateral and vertical changes in the subsurface and the identification or detection of objects, the common-offset configuration is most commonly used in GPR surveying. As the name suggests, the antennas are separated by a fixed distance, the *offset*. The source antenna emits an EM wave and the receiving antenna acquires the resulting wave field. This consists of a single measurement. When the measurement is finished the antennas are moved along the survey line by a fixed distance, *step size*, where another measurement is then completed. This process is repeated until all of the survey lines have been acquired. The objective of reflection surveys is determining the subsurface reflectivity as a function of spatial position. Changes in the reflection amplitude and time delay are indicative of a change in the velocity, v, attenuation, β, and impedance, Z. The parameters which define a common-offset GPR survey include the antenna *center frequency*, the recording *time window*, the *time sampling interval*, the station *step size*, the *antenna spacing*, the *line spacing* and lastly the *antenna orientation*.

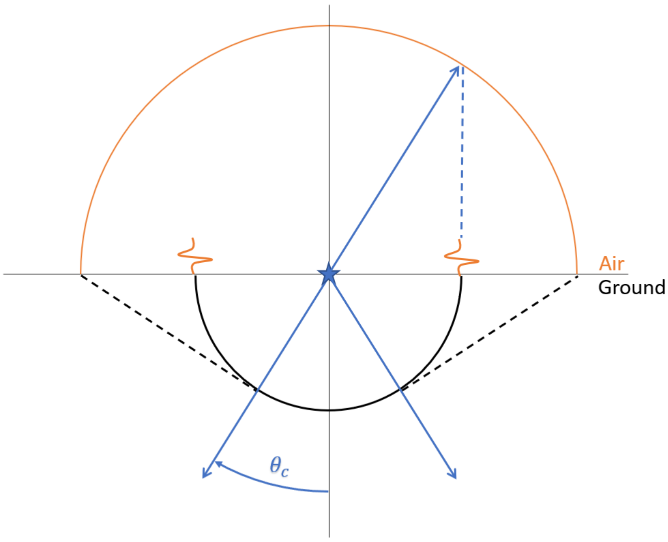

Figure 2.3: Wavefront spreading out from a localized source located on the air-ground interface. The dashed lines represent refracted waves, and the oscillating lines (orange wiggle lines) evanescent waves entering the air.

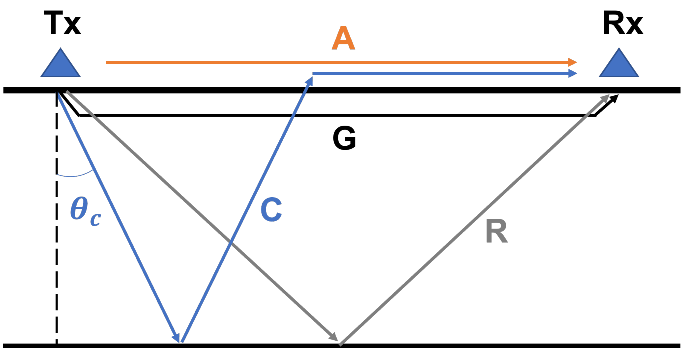

Figure 2.4: Schematic of signal paths treated as straight rays between a transmitter (Tx) and receiver (Rx) on the surface. C is the critically refracted ground wave or headwave, R is a reflected ground wave, G is the direct-groundwave and A is the direct-airwave.

Sampling Criterion

In order to ensure that the subsurface structure can be properly reconstructed from the obtained GPR data, the maximum time sampling interval Δt must be determined as defined by the Nyquist criterion. This criterion states that a signal which contains a maximum frequency of f^{max} should be sampled with a time step given by the following:

$$\Delta t \leq \frac{1}{2f^{max}} , \tag{2.44}$$

where the Nyquist frequency is f^{max}, discrete signals which contain oscillation frequencies greater than f^{max} will not be sampled properly, and thus will be indistinguishable from frequencies lower than f^{max}.

A similar relationship can be derived for the spatial domain. For discrete signals in space, oscillations should be sampled with two points per period. The oscillation period depends on the velocity in which the signal propagates for a given frequency, for the maximum frequency f^{max} in a signal taking the apparent wave velocity in the y-direction c_y^{min}, the shortest apparent wavelength is given by

$$\lambda^{min} = \frac{c_y^{min}}{f^{max}} . \tag{2.45}$$

Thus, we obtain

$$\Delta y \leq \frac{1}{2}\lambda^{min} , \tag{2.46}$$

the spatial sampling criterion in the y-direction, which is analogous to the Nyquist criterion presented in Equation 2.44. The Nyquist sampling criteria in the temporal and spatial domains can be written for transient GPR signals with a center frequency ratio equal to 1, in the form presented here

$$\Delta t \leq \frac{1}{3f^c} \tag{2.47}$$

and

$$\Delta y \leq \frac{c_y}{3f^c} , \tag{2.48}$$

where f_c is the center frequency, and c_y is the apparent wave velocity. These represent an ideal case, however the use of values which are half as large is considered more appropriate by most, therefore the expressions presented here are recommended:

$$\Delta t \leq \frac{1}{6f^c} , \tag{2.49}$$

$$\Delta y \leq \frac{c_y}{6f^c} . \tag{2.50}$$

Antenna Frequency

The selection of antenna center frequency is an important one because it has the strongest effect on depth of penetration and spatial resolution, and so the choice of frequency greatly depends on the objectives of the survey. As the frequency of a signal increases, so too does the signal attenuation in the medium as derived in Equation 2.37. In an ideal survey the antenna frequency is the highest frequency, providing greater spatial resolution, which still maintains an adequate depth of penetration which contains the target depth. An additional consideration is that in a highly cluttered subsurface higher frequencies, which have higher spatial resolution may result in strong reflections from the clutter obscuring the target signal.

Time Window

The time window setting determines the length of time in which the radar system probes the subsurface, and therefore how deep the signal can travel and still be recorded by the system. The time window value is selected based on the desired depth of penetration. The ideal time window is calculated by the system, based on the target depth and frequency being used, as well as the estimated ground velocity. This calculation of time window, t is done based on the following simple relationship

$$t = 1.3\frac{2d}{v} \ , \tag{2.51}$$

relating the velocity, v of a radio wave traveling towards a target at depth d and back. The factor of 1.3 increases the time window estimate by 30%, which helps to compensate for uncertainties in the desired depth and the approximated velocity of the radiowaves.

Antenna Step Size
During a reflection mode survey the antenna step size is the distance that the antenna is moved after each trace. This is an important quantity, as taking a step size which is too large may result in missing the detection of desired subsurface targets. The center frequency of the antenna and the dielectric properties of the subsurface material are closely linked to the selection of antenna step size. To prevent spatial aliasing, the Nyquist sampling interval marks the maximum which cannot be exceeded. The Nyquist sampling interval is presented in Equation 2.50, and also rewritten here:

$$n_x = \frac{c}{6f_c\sqrt{\epsilon_r}} \ , \tag{2.52}$$

subbing in the expression for the apparent velocity, $c_y = \frac{c}{\sqrt{\epsilon_r}}$ where c is the speed of light in free space.

Temporal Sampling Interval
The system records the signal at the receiver as the amplitude of the signal recorded at equally spaced time intervals, each recording represents a point on a trace. The distance between the points on a trace is called the temporal sampling interval. The value of the temporal sampling interval depends on the antenna frequency being used, as higher frequencies require a finer time sampling interval then lower frequencies in order to properly record the incoming signal. To avoid aliasing, the sampling interval should not exceed the Nyquist sampling criterion which is presented in Equation 2.49.

System Stacking
One key way of improving the signal-to-noise ratio of the GPR signal in a noisy environment is by maximizing the system stacking. This refers to the effect of collecting multiple traces at each survey position, averaging them and then recording the average of the traces. The noise which is a random component of the trace signal tends towards zero when averaged while the GPR signal remains unchanged, effectively increasing the signal-to-noise ratio. Stacking is maximized using DynaQ which stacks the signal as many times as possible within the time taken to traverse a single step-size, thus the stacking depends on the step-size and walking velocity.

2.2.4. Multi-offset reflection profiling

In multi-offset reflection GPR surveys, many properties and important survey considerations are the same as in common-offset profiling. The primary advantage of multi-offset profiling is that it may provide additional quantitative information, such as velocity in the subsurface or the ability to estimate the direct-wave, which common-offset surveys do not allow. The downfall is that multi-offset surveys require tedious data collection procedures. In this work, common-source multi-offset lines were collected in order to be applied to Electromagnetic Interferometry and Adaptive Subtraction procedures. Common-source lines are acquired by positioning the transmitter at a fixed position and moving the receiver antenna along a parallel line away from the transmitter position, collecting data at fixed intervals, as defined by the *step-size*. Survey considerations which are important to the success of common-source reflection profiling are *step-size*, *time window*, *time sampling interval*, and *antenna spacing*.

Electromagnetic Interferometry and Adaptive Subtraction
Electromagnetic interferometry (EI) is the process by which new EM responses are retrieved from the data through the cross-correlation of observations at two different receiver locations. The retrieved data is the EM response from so-called virtual sources. Following cross-correlation, the response is stacked (summed) across all sources. This procedure allows us to obtain the Green's function between the two receivers, which represents the EM propagation between the receivers as if there was a virtual source at one of the receiver locations. Slob and Wapenaar (2008) exacted Green's function representation for EM fields and waves in media with loses. This was done through application of the time-correlation and

time-convolution type theorems to Maxwell's equations over a volume $\mathbb{D}$ with boundary $\partial\mathbb{D}$. Taking the following assumptions to be true:

- dissipation is negligible
- electric source currents act as point sources inside $\mathbb{D}$
- medium properties near $\partial\mathbb{D}$ are locally smoothly varying
- rays which leave the volume perpendicular to the surface provide the largest contribution to the final result
- far-field approximation applies

The exact representation of the Green's function for EM fields derived by Slob and Wapenaar (2008) for fields and waves in media with losses can be simplified to

$$2\Re\{\hat{G}^{Ee}_{kr}(x_A, x_B, \omega)\} \approx -\frac{2}{\mu c} \oint_{x\in\partial\mathbb{D}} \hat{G}^{Ee}_{rj}(x_B, x_n, \omega)\{\hat{G}^{Ee}_{kj}(x_A, x_n, \omega)\}^* d^2x_n \ , \tag{2.53}$$

for use in practical applications, wherein both $x_A \in \mathbb{D}$ and $x_B \in \mathbb{D}$. Green's function in the frequency domain is given by $\hat{G}^{Ee}_{kr}(x_A, x_B, \omega)$. The superscripts denote that the signal at the receiver is an electric field E generated by an electric current e. k, r and j are subscripts which indicate the direction of the electric-field components when in the first position, and the direction of the electric-current source vector when in the second position. The receiver position is denoted by the first argument in $\hat{G}$, and the source position by the second. The left hand side of Equation 2.53 is the real part of the k-component of the electric field recorded at x_A, due to the presence of an impulsive electric source positioned at x_B due to the r-component. On the right hand side of Equation 2.53, the integrands are representative of electric fields generated by impulsive sources at the position x_n on the boundary of $\mathbb{D}$ in the j-direction. At x_A the k component of the field is measured, and at x_B the r-component. Thus we can obtain the electric field Green's function at x_A due to an impulsive source at x_B through the cross-correlation of two recordings, and summation over every source direction and every position on the boundary of $\mathbb{D}$ (Slob et al., 2007; Slob and Wapenaar, 2008). In reality the source distribution is limited, as the integration over the boundary $\partial\mathbb{D}$ requires sources surrounding the two receivers, which does not exist. The consequence is spurious events. Summing over a limited source distribution results in incomplete destructive interference meaning that non-physical events should be expected in EI results (Slob et al., 2007).

For transient sources, incorporating the source signatures and defining the electric wavefield recordings at receiver positions x_A and x_B where $x_A \in \mathbb{D}$ and $x_B \in \mathbb{D}$ (Slob and Wapenaar, 2008) the following is derived:

$$\hat{S}_0(\omega)\Re\{\hat{G}^{Ee}_{kr}(x_B, x_A, \omega)\} \approx -\oint_{x\in\partial\mathbb{D}} \hat{F}^j(x_n, \omega)\hat{u}^{obs}_r j(x_B, x_n, \omega)\{\hat{u}^{obs}_k j(x_A, x_n, \omega)\}^* d^2x \ , \tag{2.54}$$

where $\hat{S}_0(\omega)$ is a desired source power spectrum, $\hat{F}^j(x_n, \omega)$ is a shaping filter, and $\hat{u}^{obs}_r j(x_B, x_n, \omega)$ and $\hat{u}^{obs}_k j(x_A, x_n, \omega)$ are the electric wavefield observed recordings at the receivers x_B and x_A respectively. Equation 2.54 provides a method to obtain the electric field response due to a virtual source located at x_B, recorded at x_A through the cross-correlation in the time-domain of the electric field recordings at x_A and x_B due to electric point sources on $\partial\mathbb{D}$, and the summation over all of the source contributions.

Typically GPR surveys involve the acquisition of electric field recordings with the source and receiver antennas on the surface of the earth, thus all sources fall into the stationary-phase region (Snieder, 2004). Rays coming from sources positioned in the stationary-phase region are nearly parallel and thus they interfere constructively in the cross-correlation summation (Balestrini et al., 2020). In other words, across all sources, those for whom the travel-time difference between the propagation between two receivers falls into the stationary phase region, will be the dominant contribution to the cross-correlation (Snieder and Sens-Schönfelder, 2015). For GPR line surveys all of the sources and receivers are at the surface, thus they all fall into the stationary-phase region (Liu et al., 2018) thus the response obtained through the cross-correlation of responses, and stacking over all source contributions, will be dominated by high energy recordings from the direct-wave. Thus, the response obtained from EI is a good approximation for the direct-wave, which can then be used to apply adaptive subtraction procedures on the raw GPR data (Liu et al., 2018; Balestrini et al., 2020).

Adaptive subtraction is a method in which the matching and removal of coherent noise, such as the direct-wave, is performed following their prediction by data driven techniques, such as EI (Liu et al., 2018; Balestrini et al., 2020). Adaptive subtraction requires the application of a matching filter, to compensate for distortions which might appear in the predicted direct-wave model, such as amplitude, phase and frequency distortions (Fomel, 2009). A regularized nonstationary regression procedure is applied in order to allow the filter to become smoothly nonstationary, meaning that the input data does not need to be broken up into windows (Fomel, 2009).

Let's take a signal $m(x)$ which is considered the "master" signal, i.e. the raw data, and a collection of "slave" signals, $s(x)$, i.e. the data we are treating, where x is representative of coordinates in a multidimensional space. Stationary regression involves the estimation of coefficients a_k, where $k = 1, 2, ..., N$ such that the prediction error

$$e(x) = m(x) - \sum_{k=1}^{N} a_k s_k(x) \ , \tag{2.55}$$

is minimized in the least square sense (Fomel, 2009). Conversely, nonstationary regression allows the coefficients a_k to change as a function of x, meaning that the minimization of $e(x)$ in the least-squares sense is then ill-posed, as demonstrated here:

$$e(x) = m(x) - \sum_{k=1}^{N} b_k(x) s_k(x) \ . \tag{2.56}$$

Equation 2.56 is ill-posed due to the fact that more unknown variables can be obtained than constraints. In order to account for the ill-posedness, additional constraints must be included which limit the variability of the coefficients. Tikhonov's regularization is a conventional method which incorporates a regularization operator into the minimization, this is referred to as a roughening operator, D. The difference between conventional regularization methods such as Tikhonov's regularization, versus shaping regularization is that rather than specifying an appropriate regularization operator, shaping regularization requires a shaping operator, S, which is often simpler to design (Fomel, 2007). The regularized inversion takes the form

$$b = \hat{A}^{-1}\hat{d} \ , \tag{2.57}$$

where $\hat{d} = [S[s_1(x)m(x)]S[s_2(x)m(x)]...S[s_N(x)m(x)]]^T$ and the elements of the matrix $\hat{A}$ are defined as

$$\hat{A}_{ij}(x) = \lambda^2 \Delta_{ij} + S[s_i(x)s_j(x) - \lambda^2 \Delta_{ij}] \ , \tag{2.58}$$

where λ is a scaling coefficient (Fomel, 2009). The advantage of shaping regularization over Tikhonov regularization is that the selection of λ and S is much easier than the selection of the regularization roughening operator D and the associated regularization parameters.

2.3. Ground Conductivity Meter

GCMs in general fall into the broad category of small-loop frequency-domain EM systems. They typically consist of a small coil transmitter (Tx) and one or more coil receivers (Rx). The Tx and Rx coils are separated by a fixed distance (intercoil spacing, s) and move along the survey line. The Tx and Rx coils are connected by a shielded cable which carries a phase-referenced signal between the two coils (Milsom, 2003). GCMs typically operate at low frequency ($<$ 15 kHz) and at short s (Beamish, 2011). These attributes are designed such that the depth scale across which the subsurface conductivity is measured depends on the Tx-Rx separation and the coil orientation used, the details of which will be discussed further below. These EM systems are often also referred to by the Swedish term Slingram or horizontal-loop methods (HLEM) (Reynolds, 2011).

Generation of an EM field can be done by passing a current through a large loop of wire, or more commonly a small coil consisting of many wire loops. In EM surveying methods, the Tx coil is used to generate a primary EM field. An alternating voltage is applied to the Tx coil, this voltage takes the form of a sine wave. The application of voltage results in the generation of current flow (I) which follows the applied voltage by a lag time α called the phase lag. The current is sinusoidal in nature just as the applied voltage, and is assumed to be uniform along the loop. Using the thin-wire approximation the actual volume distribution of current in the wire is taken as a line of current concentrated in the centre of the loop, tangent to the loop. It can be shown that a small current carrying loop under the thin-wire approximation is equivalent to a magnetic dipole.

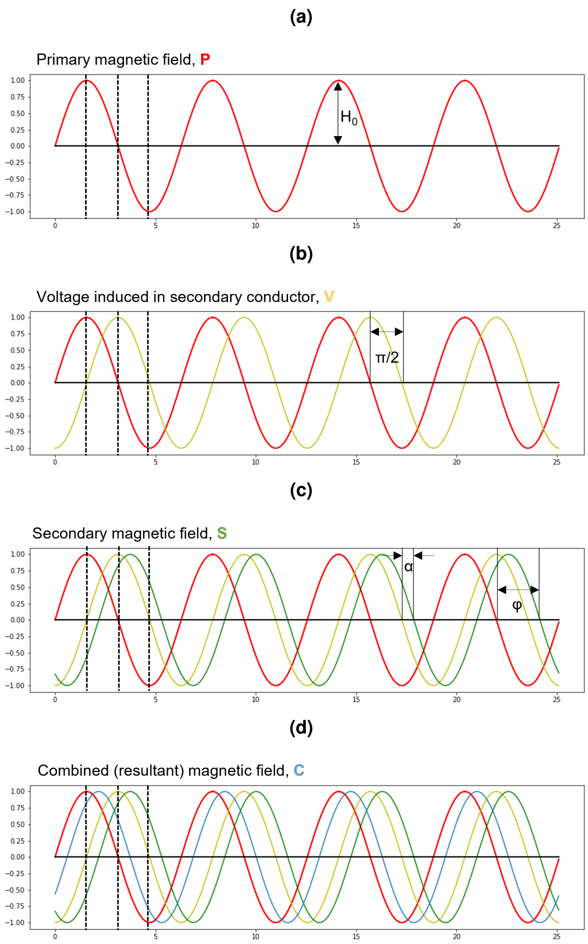

Figure 2.5: (a) The primary magnetic field shown in red with amplitude H_0 in sinusoidal form. (b) The voltage induced in the secondary conductor in the subsurface, shown in yellow, always has a phase lag of $\frac{\pi}{2}$ from the primary magnetic field. (c) The secondary magnetic field, or secondary current, shown in green, has a phase lag α from the induced voltage. The value of α depends on the electrical properties of the material. The total phase lag of S behind P is called ϕ. (d) The combined or resultant magnetic field measured at the Rx coil, shown in blue

As is known from Maxwell's equations and the properties of EM waves, when a primary magnetic field is applied, let's call it P, then the resulting orthogonal electric component of the field, $\mathbf{E}$ is "in-phase" with P, taking on the form presented in Figure 2.5a where H_0 is the peak amplitude of the magnetic field. If we imagine that a perfect conductor is present in the vicinity of the primary magnetic field P, then the voltage induced in this perfect conductor due to P has a time lag of $\pi/2$, as shown graphically in Figure 2.5b. Thus the induced voltage is in "quadrature phase" with the primary magnetic field P.

The introduction of an induced voltage in a conductor produces eddy currents, which take a finite time to generate and depend on the electrical properties of the conductor, this is called the phase lag α. This phase shift arises from self and mutual inductances, and will increase for currents which flow further from the transmitter. Thus, current flow at large distances and greater depths from the transmitter will definitely exhibit a significant phase lag α with respect to the primary field P. The effect of the phase lag is shown in Figure 2.5c. For poor conductors α is small, and in good conductors α is large.

The alternating primary magnetic field P generated at the transmitter results in a secondary magnetic field S which diffuses radially away from the transmitter in all directions. The larger the distance from the transmitter, the more progressively phase shifted S becomes. The total phase lag of S behind P is called ϕ. Once generated, the secondary magnetic field, S formed as a result of the Eddy currents interacts with the primary magnetic field, P, resulting in a combined magnetic field C. The three magnetic fields, the induced voltages and associated phase lags are depicted in Figure 2.5d. The relationship between the primary magnetic field P, secondary magnetic field S, and the combined magnetic field C can be represented in vector form, and are presented in Figure 2.6a.

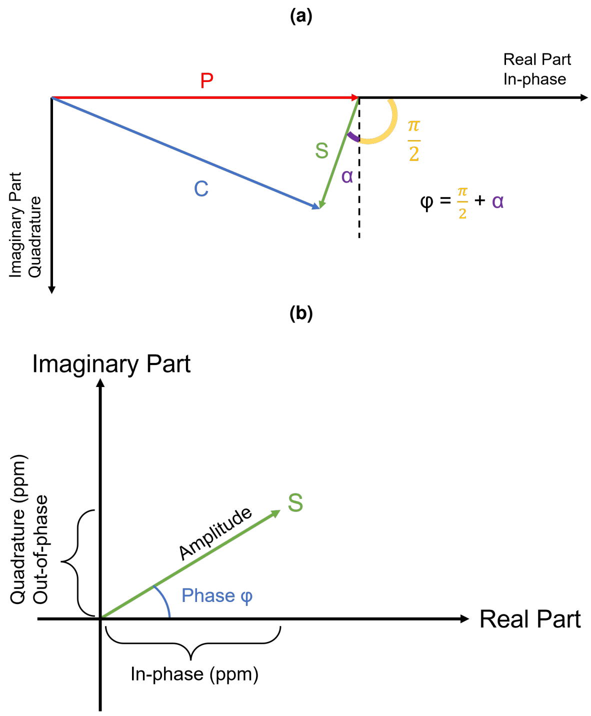

Figure 2.6: (a) Vector diagram defining the phase relationships between the primary magnetic field P, secondary magnetic field S, and the combined magnetic field C. (b) Vector form of in-phase and out-of-phase components of the secondary magnetic field S.

GCMs measure the EM coupling ratios at the Rx coil. This is a complex number which contains an in-phase and out-of-phase (quadrature) component. The in-phase (real) and quadrature out-of-phase (imaginary) components of the secondary magnetic field measured at the Rx are very important quantities, they are presented in vector form in Figure 2.6b. The secondary magnetic field vector arriving at the Rx coil can be reconstructed either from the amplitude and phase, or the in-phase and quadrature components. The field ratio between the primary magnetic field P, and the secondary magnetic field S is obtained by the GCM using phase sensitive measurements at the Tx and Rx coils. At low frequencies ($<$ 15 kHz) the material properties which are relevant to EM induction only consist of magnetic and conductivity components, dielectric components are not significant (Beamish, 2011).

The quadrature response is used to obtain the apparent conductivity (mS/m) of the subsurface, and generally exceeds the in-phase response (ppt) by an order of magnitude. The in-phase is a relative value which is not calibrated to measure magnetic susceptibility directly but is largely determined by the magnetic susceptibility contribution of the subsurface (Bonsall et al., 2013).

As in all geophysical methods, surveys are heavily concerned with depth of penetration of the emitted signal and the resolution of these instruments with depth. In a perfectly isotropic resistive medium, EM waves would travel indefinitely; this is not the case in the subsurface wherein surface conductivites are often significant and depth of penetration very limited. Depth of penetration is influenced by the frequency of the EM waves being applied and the conductivity of the subsurface media. At low frequencies (typically < 15 kHz) attenuation is negligible however signal loss occurs due to diffusion. The skin depth is, as derived previously in Equation 2.27, given by

$$\delta = \sqrt{\frac{2}{\omega\sigma\mu}} = 503\sqrt{\frac{1}{f\sigma}} \ , \tag{2.59}$$

taking the angular frequency to be $\omega = 2\pi f$ where f is the frequency in Hz, σ is the conductivity in S/m and μ is the magnetic permeability assumed to be $\mu_0 = 4\pi \times 10^{-7}$ H/m. Often a realistic estimate at which depth d an EM response could be detected is taken as $d = \delta/5$ (Reynolds, 2011).

The intercoil spacing s influences the depth of sensitivity of the measurement. Much like in conventional resistivity surveys wherein increased electrode spacing increases the total volume of sensitivity, when the intercoil spacing is increased, the volume of sensitivity of the device increases as well. The secondary magnetic field induced in the subsurface and measured at the Rx coil is a function of intercoil spacing s, among other important factors which will be discussed below.

The GCMs response to the conductivity in the subsurface depends not only on skin depth, and the intercoil spacing s but also relies heavily on the orientation of the Tx and Rx coils. There are typically two coil orientation modes, which are referred to with respect to the orientation of the coils, as horizontal co-planar (HCP) and vertical co-planar (VCP) coil configurations. These two coil configurations are demonstrated in Figure 2.7.

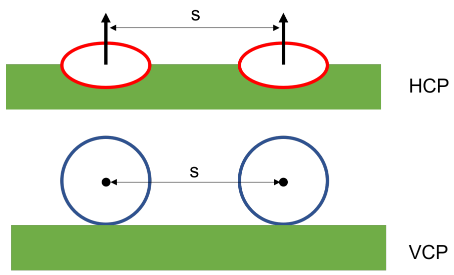

Figure 2.7: Common GCM coil configurations. The intercoil spacing is denoted s. HCP: horizontal coplanar. VCP: vertical coplanar.

2.3.1. LIN conditions

Moving-source dual-coil systems, such as the CMD-MiniExplorer used in this investigation, measure both quadrature and in-phase components and are all based on the principles of operation first introduced by McNeil (1980). The theory, important considerations and assumptions which are integral to the operation of these instruments will be discussed in the following paragraphs.

The quantity which is measured in dual-coil systems is the ratio of the secondary magnetic field S at the receiver, to the primary magnetic field P. As first shown by Keller and Frischknecht (1966) the field ratios for two coil configurations, HCP and VCP, are given by

$$(\frac{S}{P})_{HCP} = \frac{2}{(\gamma s)^2}\{9 - [9 + 9\gamma s + 4(\gamma s)^2 + (\gamma s)^3]e^{-\gamma s}\} \tag{2.60}$$

$$(\frac{S}{P})_{VCP} = 2[1 - \frac{3}{(\gamma s)^2} + [3 + 3\gamma s + (\gamma s)^2]\frac{e^{-\gamma s}}{(\gamma s)^2}] \ , \tag{2.61}$$

where,
$\gamma = \sqrt{i\omega\mu_0\sigma}$,
$\omega = 2\pi f$,

and the conductivity of a homogeneous half-space is given by σ. The γ variable is a complex function of frequency, f, and conductivity, σ, and the field ratios for both configurations are functions of the variable γ (Equation 2.60 and 2.61). Under certain conditions the expressions in Equation 2.60 and 2.61 simplify considerably.

A consequence of the skin depth δ relation presented in Equation 2.59 is that in addition to the skin depth decreasing with increasing conductivity and frequency, the rate of phase change with distance into a half-space increases with decreasing skin depth. When the incident wave diffuses into a homogeneous half-space the phase varies linearly with distance into the half-space. If the skin depth is large (i.e. the operating frequency and ground conductivity are small) then the receiver coil can be placed at a relatively large distance away from the transmitter before the S magnetic field is greater than quadrature phase with respect to magnetic field P. However, if the skin depth is small even with the receiver placed very near to the transmitter, an additional phase shift might be present with respect to S and P.

Thus, the parameters which impact whether or not the measured field S is in quadrature phase with the primary P, is the ratio between the intercoil spacing s and the skin depth δ. This ratio is denoted by B, and is known as the induction number. Equation 2.59 can be rearranged into a function of the variable γ shown here:

$$\delta = \sqrt{\frac{2}{\omega\sigma\mu_0}} = \frac{\sqrt{2i}}{\gamma} . \tag{2.62}$$

Rearranging for γ we obtain an expression relating the quantity to the induction number, B

$$\gamma s = \sqrt{2i}\frac{s}{\delta} = \sqrt{2i}B . \tag{2.63}$$

If $B <<< 1$, i.e. if $|\gamma s| <<< 1$ then the field ratios from Equation 2.60 and 2.61 simplify to the following expression:

$$(\frac{S}{P})_Q \approx \frac{iB^2}{2} = \frac{i\omega\mu_0\sigma s^2}{4} , \tag{2.64}$$

wherein the magnitude of the quadrature component of the secondary magnetic field is proportional to ground conductivity. The phase of the secondary magnetic field is thus assumed to be shifted from the primary magnetic field by 90 °, and thus is the in-phase quadrate. The primary assumption being that the self and mutual inductances are negligible, and no additional significant phase shifts are present in S with respect to P.

Under the same low induction number (LIN) assumptions, Kaufman and Keller (1983) demonstrated that there is in addition to Equation 2.64, a small in-phase component to the secondary magnetic field which is given by

$$(\frac{S}{P})_I \approx \frac{8B^3}{15} = \frac{2\sqrt{2}}{15}s^3(\omega\mu_0\sigma)^{3/2} . \tag{2.65}$$

It's very important to note that Equation 2.65 has a dependence on B^3 whereas Equation 2.64 has a dependence on B^2, meaning that for small values of B the in-phase component of the field S, will be much smaller than the quadrature phase component.

In order to ensure that B is much less than unity, s must remain much less than δ. Given a fixed value for s based on the instrument properties, the effective depth of penetration under the LIN conditions also becomes fixed. The choice of operating frequency by manufacturers is thus selected based on probable ground conductivity in order to ensure that

$$\omega << \frac{2}{\mu_0\sigma s^2} , \tag{2.66}$$

is always satisfied. Thus under the LIN approximation the apparent conductivity which is read by the instrument is given by

$$\sigma_a = \frac{4}{\omega\mu_0 s^2}(\frac{S}{P})_q \ . \tag{2.67}$$

The quantity $\frac{S}{P}_q$ is the quadrature component of the ratio between the secondary magnetic field S and primary magnetic field P. This simplification shown above in Equation 2.67 is derived from the inference that the condition $B <<<1$ is the same as the assumption that the magnetic coupling between loops can be ignored, because the operating frequency is sufficiently low. Therefore, current flowing through a loop is assumed to meet two conditions: one, that the current in the loop is independent of the current flowing through all other loops because the are not magnetically coupled, and two, the current flowing through a loop is only a function of the primary magnetic flux associated with that loop and of the conductivity in the subsurface (McNeill, 1980).

Impulse response function

In multi-separation instruments the ability to apply different coil configurations and intercoil spacing provides a degree of control with respect to the discrimination of depth. Imagine the situation wherein we have the dual-coil instrument sitting on the surface of a homogeneous half-space. Assuming that the LIN model described above holds true (which is a large assumption), the relative contribution of a thin semi-infinite horizontal layer at a normalized depth z (z = depth / s) to the secondary magnetic field measured at the receiver is referred to as the impulse response function ϕ (Reynolds, 2011). The impulse response for the quadrature component in HCP and VCP coil orientations are given by

$$\phi_{HCP}(z) = 2 - \frac{4z}{(4z^2+1)^{1/2}} \tag{2.68}$$

and

$$\phi_{VCP}(z) = \frac{4z}{(4z^2+1)^{3/2}} \ . \tag{2.69}$$

The impulse response function for the in-phase component in the HCP and VCP orientations are given by

$$\phi_{HCP}(z) = \frac{12z}{(4z^2+1)^{5/2}} \tag{2.70}$$

and

$$\phi_{VCP}(z) = \frac{12z(3-8z^2)}{(4z^2+1)^{7/2}} \ . \tag{2.71}$$

Using this function the secondary magnetic field at the Rx coil from any layer at the position z in the subsurface can be calculated. This function is possible given two assumptions: all current flow is horizontal and all current loops are independent of other current loops, i.e. the LIN approximation must hold; the apparent conductivity is linearly proportional to the quadrature component of the secondary magnetic field. The impulse response function looks very different for the two different coil configurations. The quadrature impulse response function for the HCP and VCP orientations for the CMD-MiniExplorer are presented in Figure 2.8, under the assumption that the LIN conditions are met. Here the manufacturers have used depth measurements rather than normalized depth z, given the 3 intercoil spacings measured using the CMD-MiniExplorer. The expected penetration depths for each Rx coil, given the intercoil spacing is provided by the manufacturer. These quantities are listed in Table 2.1.

As can be seen in Figure 2.8, the response recorded in HCP orientation is less sensitive to features in the very near surface, and thus in theory the near surface contributes less to the response at the Rx coil. The maximum relative contribution in HCP configuration occurs at a normalized depth of z = 0.4. For the CMD-MiniExplorer, for all Tx-Rx pairs in HCP orientation maximum relative contribution comes from the top 0.5 m. Whereas for the VCP configuration the relative response decreases with layer depth, achieving a maximum contribution at the surface, z = 0, making the system very sensitive to near surface objects.

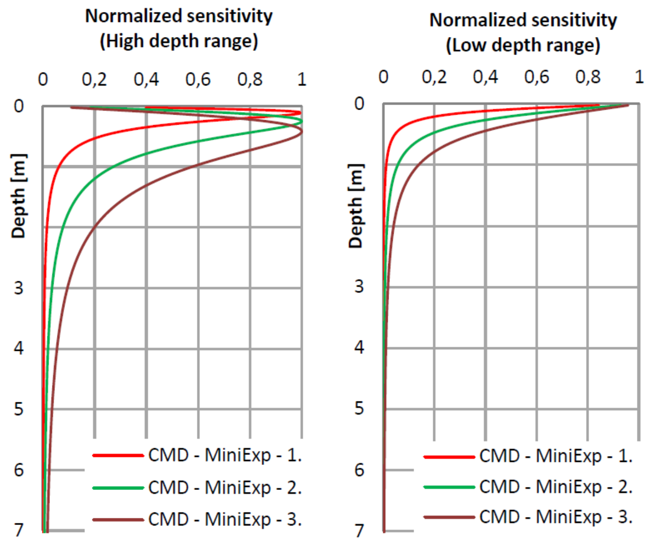

Figure 2.8: Normalized sensitivity with depth for HCP (high depth range) and VCP (low depth range) configurations for the CMD-MiniExplorer GCM. The impulse response function for HCP (left) and VCP (right) is shown for all three intercoil spacings s (1 - 0.32 m, 2 - 0.71 m, 3 - 1.18 m). Obtained from GF Instruments (2016).

Table 2.1: Sensitivity of CMD-MiniExplorer with depth according to Impulse Response Function. Obtained from GF Instruments (2020).

Coil configuration	Intercoil spacing	Depth range	Peak contribution from depth
HCP	0.32 m	0.5 m	0.128 m
	0.71 m	1.0 m	0.284 m
	1.18 m	1.8m	0.472 m
VCP	0.32 m	0.25 m	0 m
	0.71 m	0.5 m	0 m
	1.18 m	0.9 m	0 m

Limitations

LIN mode instruments are intended to provide direct estimates of the apparent conductivity, which is taken as equivalent to the true conductivity of a half-space. However, as shown by Beamish (2011), beyond a low-conductivity limit (e.g. $\leq$12 mS/m) these instruments exhibit non-linear departures from the apparent conductivity associated with the LIN condition. These departures are a function of coil configuration, instrument elevation above the ground and the prevailing conductivity in the subsurface. As a result it is insufficient to determine the validity of the LIN conditions for a given measurement based on the induction number alone, rather the instrument elevation, coil configuration and required accuracy of the measurements must be jointly considered. Beamish (2011) demonstrated that with increasing instrument elevation, there exists a significant deviation from apparent conductivity. The sensitivity to these elevation changes increases with larger prevailing conductivities. As introduced previously, the LIN conditions are based on the assumption that the measurements occur at zero elevation, however all instrument coils are encased by some protective material, forcing some offset from direct contact with the ground. The presence of a layer of air which has $\sigma_a = 0$ has a significant effect on the measured response.

As mentioned above, multi-separation instruments, such as the CMD-MiniExplorer, are intended to function within the LIN conditions however, intrinsically depart from the condition with increasing intercoil spacing. As the intercoil spacing increases, and the frequency of the transmitted wave remains fixed, the condition of $s << \delta$ begins to lose validity. This is related to a geometrical effect of the EM measurement system and not due necessarily to variations in conductivity with depth (Beamish, 2011). Another important thing to note regarding the LIN approximation is that for a given frequency and intercoil spacing s, as the prevailing terrain conductivity increases, the LIN approximation given in Equation 2.64 breaks down. Thus, in order to obtain an estimate of the subsurface conductivity which is consistent with LIN regardless of elevation, configuration and prevailing conductivity, a correction procedure must be applied to the measured data. The correction procedure determines the theoretical response for a homogeneous half-space, using Equation 2.60 and 2.61, for the apparent conductivities measured by the instrument. These "true conductivities" calculated with the theoretical equations rather than the LIN approximation are then used to correct the measured values.

Modelling ground response

For two HCP and VCP loops lying on the earth's surface the exact value of the field ratio between the secondary magnetic field S and the primary magnetic field P at the receiver is given by Equation 2.60 and Equation 2.61 respectively. However, in the majority of applications the loops are being held above the earth's surface, and thus the results of Equation 2.60 and Equation 2.61 are an approximation. This approximation becomes invalid very quickly, and thus a general expression must be used instead when considering dual-coil systems raised above the ground, for HCP the response is given by

$$\hat{G}_{zz}^{mm,r}(x^r - x^s, \omega) = \frac{1}{4\pi i\omega\mu_0} \int_{\kappa=0}^{\infty} \frac{R_0^{TE} \exp(-\Gamma_0 |z^r + z^s|)}{\Gamma_0} J_0(\kappa r)\kappa^3 d\kappa \ , \tag{2.72}$$

where $\hat{G}_{zz}^{mm,r}$ is the Green's function for the scattered field where x^r is the center of the receiver loop and x^s the center of the source loop (Slob, personal comm.). The source and reciver positions are given by z^r and z^s. R_0^{TE} is the reflection response at the surface. Γ_0 is the vertical wavenumber, κ is the radial wavenumber, and r is the source-receiver distance. $J_0(\kappa r)$ is the Bessel function of the first kind and order zero. The general expression for VCP configuration is

$$\hat{G}_{zz}^{mm,r}(x^r - x^s, \omega) = \frac{1}{4\pi i\omega\mu_0} \int_{\kappa=0}^{\infty} R_0^{TE} \exp(-\Gamma_0 |z^r + z^s|) J_1(\kappa r)\kappa d\kappa \ , \tag{2.73}$$

where $J_1(\kappa r)$ is the Bessel function of the first kind and order one. In the case of VCP loops, $x^r - x^s = 0$ given that the centre of the source and receiver loops are in the same plane of the loops. These expressions can be used to calculate the true ground response when the coil loops are positioned above the earth's surface, and just as with the LIN correction, can be used to correct the apparent conductivity measurements collected with GCMs. This correction procedure allows for the acquisition of apparent conductivity measurements in the subsurface which are consistent, regardless of elevation, configuration and prevailing conductivity in the subsurface, which is especially important when comparing results between studies which use different GCMs, in contrasting environments and at different elevations above the surface.

3 Methods

3.1. Survey site

In this investigation at the ARISTA test facility, three burials were surveyed with geophysical methods. The position of these burials is depicted in the map presented in Figure 3.1. The burials were dug individually and in a standardized way to a size of 1 m x 2 m and to a depth of 0.6 m. They were initially dug for a taphonomic study in which the bodies were exhumed and observed 13 weeks ($\sim$ 90 days) following initial burial (PDI). The burial date and the date of full exhumation and reburial are listed in Table 3.1 for each burial, in addition to the age, or days since initial burial (PDI) on the day of each survey. Digital probes for monitoring of sub-surface conditions were buried with the bodies, though it is unknown whether they have been removed since or are still present (Nienaber, personal comm.). The position of the bodies upon first burial was in anatomical position (lying on their back). Upon reburial the bodies were placed in different positions, in different locations in the grave, for example directly against the side of the grave, or lying on their side (Nienaber, personal comm.). The specific situation of each burial is not known exactly.

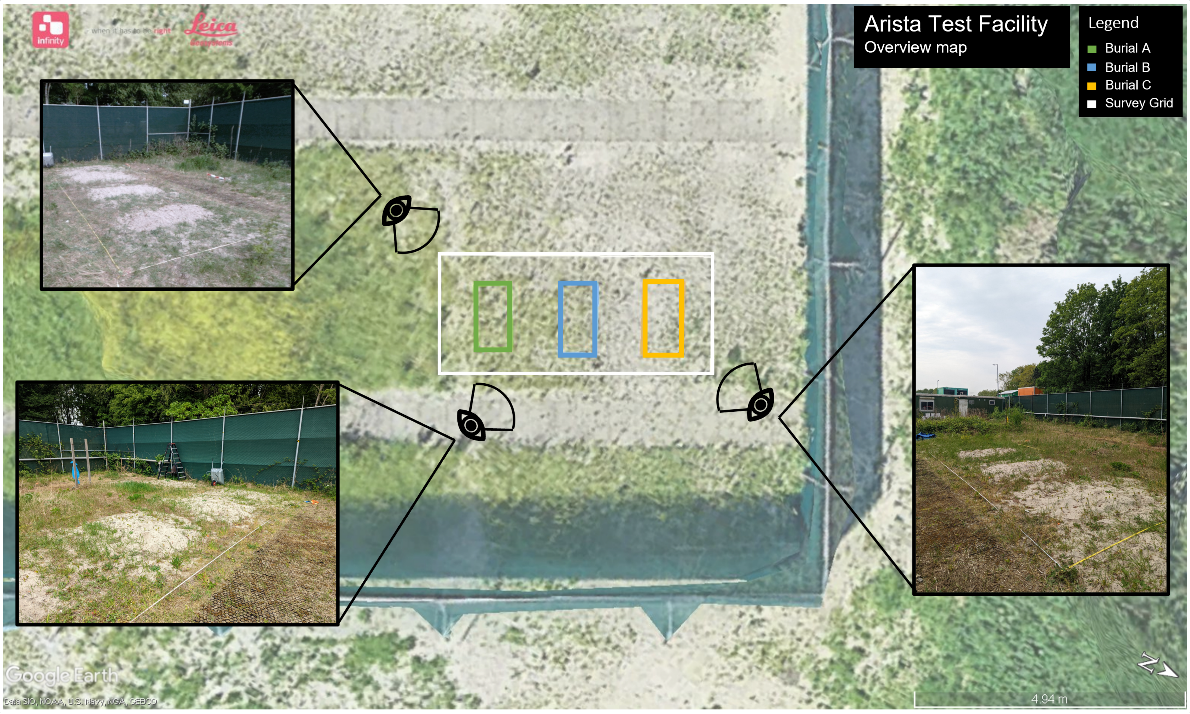

Figure 3.1: Overview Map of the ARISTA facility where GPR and GCM surveys were performed in this work. The three burials of interest for this study are marked in Green - burial A, Blue - burial B and Orange - burial C. Inset images provide a visual of the burials in their present state, wherein the grave-fill can be clearly differentiated from the surrounding soil.

In addition to the exhumation and reburial on the dates listed in Table 3.1, the burials were excavated a number of additional times for visual observation and sampling. In particular, burial C in orange on the right of Figure 3.1 was excavated several times and used for training purposes. In one instance the edge of burial C collapsed or widened due to repeated excavation, this is visible on the surface, as demonstrated in Figure 3.1. The burials were dug in an undisturbed deposit, meaning that the base of the burials consists of undisturbed compacted soil, made up of the marine sand which was brought into

Table 3.1: Burial, exhumation and reburial dates and the relative ages since first burial on survey days.

Burial ID	Burial	Exhumation and reburial	Day 1	Day 2	Day 3	Day 4
C	Sept. 24th 2021	Dec. 23rd 2021	228	243	251	263
B	Oct. 15th, 2021	Jan. 13th 2022	207	222	230	242
A	Nov. 3rd, 2021	Feb. 2nd 2022	188	203	211	223

the site when the land was reclaimed. The grave-fill is the soil excavated from the burial. As a result of the multiple excavations, the grave-fill soil is clearly distinguishable from the surrounding soil, it is less compacted and consists of a mix of different horizons, organic topsoil and marine sand. In addition, no vegetation is present on top of the burials due to agitation of the soil. The bottom and sides of the grave constitute the original soil, and the grave-fill is a mix thereof as well as the presence of a cadaver.

In addition to surveys at ARISTA, preliminary zero-measurement data was collected at a police facility in Almere wherein cadavers are planned to be buried. Due to unforeseen issues with the project planning, the timeline did not match up with the timeline of this thesis, and thus only zero-measurement data was obtained. However this data did contribute to the understanding of GPR acquisition parameters, and will be discussed later in this chapter. Zero-measurement surveys were collected in three 7 x 5 m grids at the Almere test site using the same GPR and GCM survey settings as used in this investigation.

3.2. Survey Instruments and Design

3.2.1. Instrumentation

Figure 3.2: CMD-MiniExplorer GCM equipped with a GPS unit obtaining continuous measurements (left) and Leica GS18 I used to obtain point locations and images (right) at the ARISTA test site on Day 1.

CMD-MiniExplorer

The CMD-MiniExplorer from GF Instruments was used in this investigation. This instrument is a three depth probe, which can be used in either HCP or VCP configuration with depth ranges 0.5 / 0.25 m, 1.0 / 0.5 m, 1.8 / 0.9 m. The probe is attached to a holder which allows the user to walk with the probe directly above the ground surface ($\sim$ 5 cm). The CMD-MiniExplorer was used while connected to a GPS unit to collect GPS referenced data in a continuous measurement setting. Figure 3.2 contains images of the CMD-MiniExplorer operating in the field.

NOGGIN
The NOGGIN with SmartCart from Sensors & Software Inc. was used in this investigation, with the 250 MHz and 500 MHz shielded antennas. This system was used to obtain common-offset survey grids. The odometer setting was used to collect data. The NOGGIN antennas are located in a single shielding unit with a baseplate, which has the dimensions 63 x 41 x 23 cm for the 250 MHz and 38 x 23 x 15 cm for the 500 MHz. Figure 3.3 contains images of the NOGGIN operating in the field.

pulseEKKO
The pulseEKKO with SmartTow from Sensors & Software Inc. was used in this investigation, with the 250 MHz and 500 MHz shielded antennas. The system was used to obtain common-source lines, in addition to common-offset lines. The odometer, and hand tow settings were used to collect data. The 250 MHz transducer footprint is 30 cm x 30 cm, and the 500 MHz transducer footprint is 15 cm x 15 cm. Figure 3.3 contains images of the pulseEKKO operating in the field.

Leica GS18 I
The Leica GS18 I is a GNSS RTK Rover with visual positioning. The rover works by gathering the site in images, and then allows the user to measure points from them, either directly in the field or later, using the Leica Infinity software. The GS18 I rover was used on Day 1 to quickly and accurately characterize the positions of the four corners of the survey grid. An image of the Leica in use is presented in Figure 3.2. The point positions, and their measurement accuracy are included in Appendix C for reference, and future works. In addition to points, a number of images were collected with the GS18 I to be used for improved positioning of the grid.

Figure 3.3: Top: The pulseEKKO GPR with SmartTow being used for common-source data collection on Day 3. The left image is the 500 MHz antenna and the right image is the 250 MHz antenna. Bottom: The NOGGIN 250 MHz with SmartCart being used to collect 3.5 x 8 m grid on Day 2.

3.2.2. Day 1: Dry Grid
On May 10th, 2022, the first survey was performed at the ARISTA facility. This will be referred to as Day 1. On Day 1, two common-offset GPR grid surveys were carried out using the NOGGIN over the

Table 3.2: GPR common-offset survey acquisition parameters Day 1, 2 and 4.

Property / Setting	Value for 250 MHz	Value for 500 MHz
Line spacing	0.25 m	0.25 m
Walking direction	unidirectional	unidirectional
Frequency	250 MHz	500 MHz
Time window	42.9 ns (2 m depth)	43.1 ns (2 m depth)
Velocity	0.1 m/ns	0.1 m/ns
Sampling interval (pts/trace)	400 ps	200 ps
Stacks	DynaQ	DynaQ
Sample spacing	0.05 m	0.05 m
Antenna separation	0.250 m	0.155 m

Table 3.3: CMD-MiniExplorer survey acquisition parameters Day 1 and 2.

Property / Setting	Value - Day 1	Value - Day 2
Line spacing (dL)	0.5 m	0.5 m and 0.25 m
Walking direction	snaking back and forth	snaking back and forth
Measurement time	0.3 s	0.3 s
Coil configuration	HCP and VCP	HCP and VCP

three burials, one with a 250 MHz antenna and the second with a 500 MHz antenna. The survey grid is schematically shown in Figure 3.4 and the acquisition parameters are listed in Table 3.2. Additionally, GPR airwave measurements were obtained by flipping the antennas up to the sky and measuring a single line through the air. This was completed for both the 250 MHz and 500 MHz antenna.

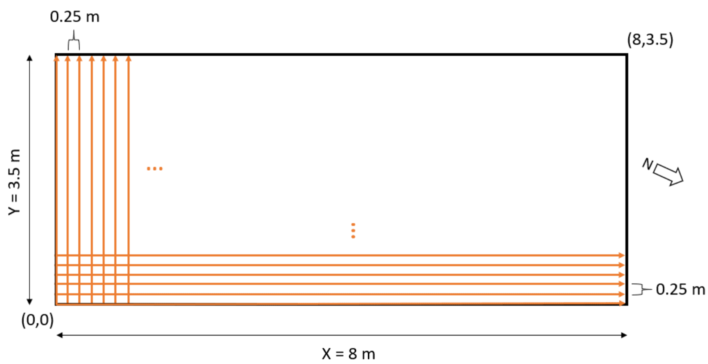

Figure 3.4: GPR common-offset survey grid used on Day 1 and 2. Both x- and y-lines, shown in orange, are collected with 0.25 m separation, across the entirety of the grid. The dimensions of the grid are x = 8 m and y = 3.5 m.

In addition to the GPR surveys, two GCM surveys were performed, one in HCP configuration and the second in VCP configuration. GCM surveys were performed over the same area as the GPR surveys. The survey grid is shown in Figure 3.5 and the acquisition parameters are listed in Table 3.3.

The conditions on the Day 1 survey were very dry, it had not rained in the region for over one week. The grave-fill material on the surface was noticeable dry and very loose, forming small hills over the burial locations as seen in Figure 3.2.

3.2.3. Day 2: Wet Grid

On May 25th, 2022, or what will be referred to as Day 2, a second geophysical survey was conducted. The Day 2 survey was identical to Day 1 with the exception of the soil conditions. On Day 2 the soil was noticeably damp from a rain event which occurred 1-2 days prior. As a result the grave-fill was more compact and darker in color. The color difference in the grave-fill is substantial when comparing Figure 3.2 from Day 1 and the bottom row of Figure 3.3, from Day 2.

In addition, on Day 2 GCM surveys were conducted using both a 0.5 m spacing, as on Day 1, and a 0.25 m spacing. The acquisition parameters for Day 2 are listed in Table 3.3. An additional observation

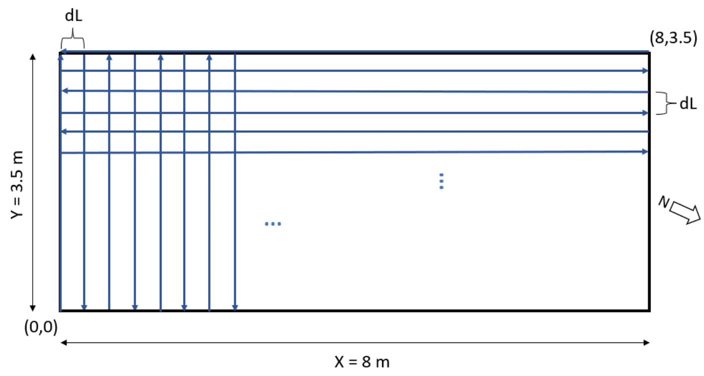

Figure 3.5: CMD-MiniExplorer Survey Grid used on Day 1 and 2. Survey lines, shown in blue, were collected with dL = 0.5 m on Day 1 and dL = 0.25 m on Day 2, where dL is the distance between lines. The lines were collected continuously and in serpentine, alternating directions in x and y. The dimensions of the grid are x = 8 m and y = 3.5 m.

to note on this day was the presence of other individuals performing work next to the survey area. These individuals used a number of electronics, which may have impacted the geophysical surveys on Day 2, in particular GCM surveys. These individuals were located along the y=0 line of the survey grid.

3.2.4. Day 3: Common-source lines

On June 2nd, 2022, or what will be referred to as Day 3, a third survey was completed at ARISTA with a pulseEKKO GPR in both common-source and common-offset configurations. Common-source data was collected along three different lines of interest, for both the 250 MHz and 500 MHz antenna. The details of these common-source lines are outlined in Table 3.4, and the locations of these lines on the grid are presented in Figure 3.6. The common-source lines were collected by first positioning the transmitting antenna at the zero position, with the receiving antenna placed as close as possible to the transmitting antenna. Then, the receiving antenna was pulled away from the transmitting antenna until a maximum offset was reached. The maximum offset varied between lines, but was approximately 4-5 m for lines perpendicular to the burials and 2-3 m for lines parallel to the burials. This process was then repeated once more, except with the transmitting antenna positioned exactly 0.82 m (250 MHz) or 0.29 m (500 MHz) from the first position. This process is shown schematically in Figure 3.7.

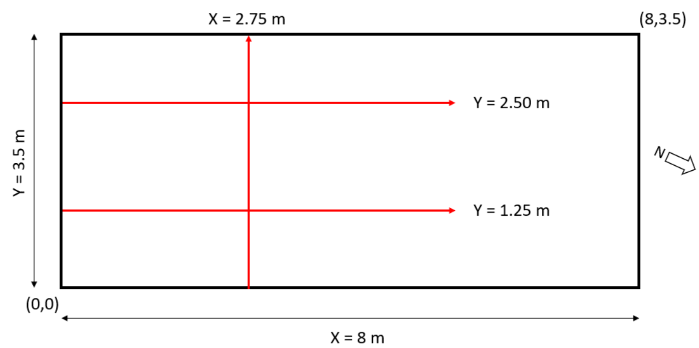

Figure 3.6: GPR common-source line positions shown in red on Day 3. The lines were collected along common-offset lines at positions x = 2.75 m, y = 1.25 m and y = 2.50 m. The length of the lines varied, the length for lines oriented parallel to the x-axis ranged from 4-5 m and along the y-axis 2-3 m.

Following this acquisition, 8 common-offset lines were obtained along lines of interest using both the 250 Hz and 500 MHz antennas. The line positions are shown in Figure 3.8 and the acquisition parameters are listed in Table 3.5. The conditions at the site on Day 3 were comparable with Day 2. The grave-fill soil was notably damp and compacted, however it had been over 1 day since the area had seen substantial precipitation. Indications of the increased moisture in the soil are present in the images in the top row of Figure 3.3 wherein the colour of the grave-fill is substantially darker than the images in Figure 3.2 taken on Day 1.

Figure 3.7: Schematic demonstrating the acquisition of common-source line data. Tx = transmitter, Rx = receiver. (a) Acquisition at starting position 1. (b) Acquisition at starting position 2.

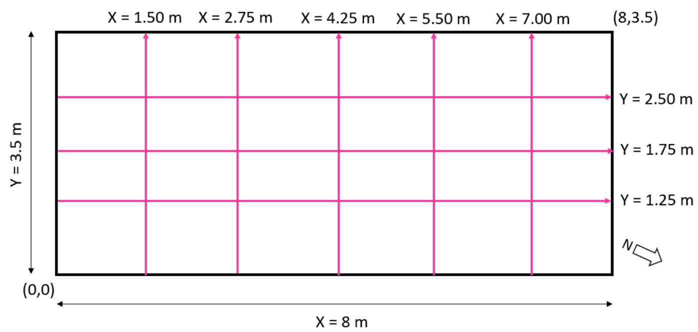

Figure 3.8: GPR common-offset line positions on Day 3. Common-offset lines, shown in pink, were obtained along 3 x-lines 8 m in length and 5 y-lines 3.5 m in length. The positions of the selected lines are depicted here.

Table 3.4: GPR common-source line data acquisition parameters Day 3.

Property / Setting	**Value for 250 MHz**	**Value for 500 MHz**
Frequency	250 MHz	500 MHz
Time window	44 ns	42.4 ns
velocity	0.1 m/ns	0.1 m/ns
sampling interval (pts/trace)	400 ps	200 ps
Stacks	DynaQ	DynaQ
Sample spacing (dR)	0.05 m	0.05 m
First Tx position (Tx1 (i))	0 m	0 m
First Rx position (Rx1 (i))	0.82 m	0.29 m
Second Tx position (Tx2 (i))	0.82 m	0.29 m
Second Rx position (Rx2 (i))	1.64 m	0.58 m

Table 3.5: GPR common-offset line acquisition parameters Day 3.

Property / Setting	Value for 250 MHz	Value for 500 MHz
Frequency	250 MHz	500 MHz
Time window	44 ns	42.4 ns
velocity	0.1 m/ns	0.1 m/ns
sampling interval (pts/trace)	400 ps	200 ps
Stacks	DynaQ	DynaQ
Sample spacing	0.05 m	0.05 m
Antenna separation	0.38 m	0.23 m

3.2.5. Day 4: Angled Grids

On June 14th, 2022, or what will be referred to as Day 4, the fourth and last survey was conducted over the area of interest at ARISTA. This survey involved the acquisition of GPR data with the NOGGIN 250 MHz and 500 MHz in angled grids. These two grids are oriented at 45° to the larger grid from Day 1 and Day 2. The angled survey grids are shown in Figure 3.9 and the acquisition parameters are the same as on Day 1 and 2, and are listed in Table 3.2.

The conditions on Day 4 were substantially drier than on Day 2 and Day 3, as the last rainfall occurred approximately 1 week prior. The grave-fill appeared dry and loose, but less so when compared to Day 1. Images of the two survey grids, and the surface soil conditions are shown in Figure 3.10.

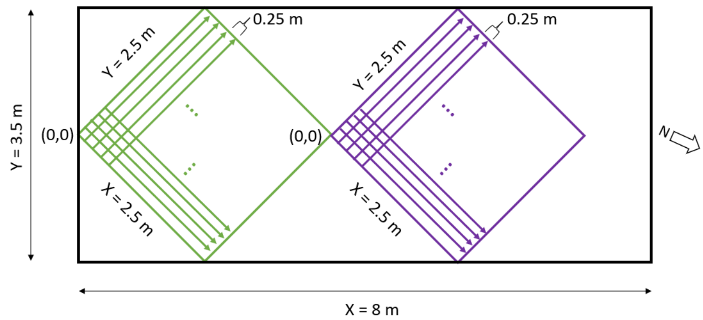

Figure 3.9: GPR common-offset angled grid configuration on Day 4. Sq1 is shown in green, and Sq2 in purple. The dimensions of both grids are 2.5 m x 2.5 m. The lines were obtained along x- and y-directions in one direction, with 0.25 m line spacing. Sq1 and Sq2 are oriented at 45° to the original common-offset grid from Day 1 and 2 shown in black with dimensions 8 m x 3.5 m.

3.3. Data processing

3.3.1. Ground Penetrating Radar

Processing and display in EKKO_Project 6

Some initial GPR processing was completed in EKKO_Project 6 software, both to prepare the data for additional processing and analysis in MATLAB as well as to generate timeslices. The following paragraphs summarize the processing steps applied to the data, while the exact settings and input parameters used for data processing in EKKO_Project 6 are listed in Table 3.6. In EKKO_Project 6 a number of processing steps are applied automatically once the data has been imported into the program. Thus, the first step is to remove the automatic processing done by the software. This is done by simply selecting the appropriate lines in line-view and adjusting the Gain/Filter settings such that none are applied to the data.

The first step in the data processing flow applied to GPR line data is to ensure the alignment of time-zero for each trace. During data collection the program automatically selects the position in time where the first break occurs on the first trace of every line. The first trace is examined for the first large deflection, which can be either a positive peak or a negative trough. This first-break corresponds to the arrival of the direct-airwave at the receiver. In the software the picking is often done quite sufficiently, thus in this case manual re-picking was unnecessary, however, it is an important check to ensure high enough precision has been obtained by the instrument.

Figure 3.10: Images of the two common-offset angled grids on Day 4. Images were taken from on top of a ladder with the camera facing south-east. On the left is Sq1, the green grid from Figure 3.9 and on the right is Sq2, the purple grid from Figure 3.9.

Table 3.6: EKKO_project 6 processing settings applied to line data and used in timeslice generation.

Line Processing	**Parameters**
Declip	Clip level (mV) = 48.0
Dewow	Window Width (pulse widths) = 1.33
Grid Processing Step	Parameters
Background Subtraction	Off
Slice Processing	**Parameters**
Time	On
Slice Resolution	0.05 m
Dewow	On
Envelope	On
Migration	Off
Slice thickness	1.00 ns
Overlap	0%
Depth Limit	Max
Interpolation limit	Auto
Amplitude Equalization Gain	Auto

Declipping was performed on line data prior to display and processing in MATLAB in order to prevent signal clipping from impacting the shape of the GPR signal response. For data which has exceeded the recording dynamic range of the GPR receiver electronics, the receiver outputs a single maximum value which is set to record until the signal returns to the recording range of the receiver. The result is often flat tops in the peaks of the positive and negative going signals. Declipping identifies points which have been clipped, which is often slightly less than the anticipated hardware limit of 50 mV, and recovers the original signal before signal clipping occurred.

The next processing step, one which is in almost every case applied to GPR data, is *Dewow*. As discussed previously, low frequency components of EM fields do not propagate, but rather diffuse into the ground, thus the low end of the frequency spectrum exhibits an inductive response rather than a propagation response. The 'wow' is the slow decaying transient field which follows the larger transmit pulse emitted by the instrument. The data is high-pass filtered, *Dewow*, to remove the unwanted low frequency component.

Often, gain is applied to 2D GPR profiles due to the natural decrease in radar signal strength with time, or equivalently with depth, in the subsurface. In order to boost signal amplitude at later times, a gain function can be applied. However in this investigation gain was not applied to radargrams given that a response was already detected in the raw data without applying gain, thus preserving relative and potentially valuable amplitude information.

Timeslice data was generated in EKKO_Project 6 software for all grid datasets collected in this work, utilizing identical settings to ensure fair comparison. The timeslice data processing settings are summarized in Table 3.6 and will be discussed shortly below. Timeslices are generated by averaging all amplitude values within the thickness range measured in nanoseconds. Timeslice processing was done in time rather than depth in order to remove the dependency of a potentially inaccurate ground velocity assumption. The thickness of the slices was set to 1.00 ns. Line processing which was applied to the data included Dewow, as described previously, as well as Envelope. The process of enveloping takes the original signal which is comprised of positive and negative lobes and converts it into all positives, removing the oscillatory nature of the wavelet. The result is that the data is presented in its true resolution. The grid processing in EKKO_Project 6 generates timeslices through interpolating data between the gaps in the GPR lines. Finer line spacing results in fewer interpolation artifacts in the timeslices. Amplitude Equalization Gain was also applied to compensate for weaker signals at depth. This is helpful when comparing the relative signal strength of targets at different timeslices. Auto setting was used, which calculates an appropriate attenuation, maximum gain and starting gain for the grid based on the average decay curve of the GPR signal strength over time.

Airwave removal

One method which can be used in signal processing of the retrieved GPR response is deconvolution. The goal of all deconvolution processes is to better elucidate the signal from the noise. In this case we aim to perform inverse filtering on the GPR traces in order to remove the response of the direct-airwave and in the process remove the inherent time-shift in the data by deconvolving each trace to a zero-delay wavelet. The time-delay is equivalent to a phase lag. The process by which a wavelet, say a single trace in a radargram, is compressed to a zero-lag spike is called spiking deconvolution. Filters which achieve this goal are the inverse and least-squares inverse filters; here inverse filtering is applied (Yilmaz, 2001).

First we redefine the ground's response, $g(t)$, without any contribution from the direct-airwave as a new impulse response given by

$$g_a(t) = f(t) * r(t) \ , \tag{3.1}$$

where $f(t)$ is a filter and $r(t)$ is the received signal. The goal is to remove the airwave from every trace $r(t)$ to obtain $g_a(t)$ through inverse filtering. To determine $f(t)$ we can redefine Equation 2.43 where we imagine that the only unwanted component of the signal measured in the radargram impulse response $r(t)$, is the airwave impulse response $a(t)$. Thus, in Equation 2.43 $w(t)$ is substituted for $a(t)$. Substituting $g_a(t)$ from Equation 3.1 above into $g(t)$ from Equation 2.43, we obtain

$$r(t) = f(t) * r(t) * a(t) \ . \tag{3.2}$$

Eliminating $r(t)$ from both sides of the equation, and solving for the filter operation $f(t)$ we obtain the function presented here:

$$f(t) = \delta(t) * \frac{1}{a(t)} \ . \tag{3.3}$$

Thus, the filter which is required to obtain $g_a(t)$, the desired output from the received response $r(t)$ is the mathematical inverse of the airwavelet $a(t)$. Equation 3.3 implies that the inverse filter $f(t)$ converts the airwavelet to a series of spikes beginning at t = 0 which form the airwave response. Thus, the inverse filter converts the radargram made up of $r(t)$ into a series of zero-lag spikes which define the response without the airwave present.

In this case the input wavelet is the average airwave trace. The spiking deconvolution operator is the inverse of the input wavelet. If the wavelet approaches that of a sufficiently minimum phase wavelet then we obtain a stable inverse which is also minimum phase. A stable inverse is one which contains filter coefficients which form a convergent series, ie. the coefficients decrease in time. In order to ensure that the average airwave trace behaves as a minimum-phase wavelet, a taper is applied. Measurements were taken with the GPR antenna pointing up to the sky to obtain a number of traces with the airwave isolated. Then, in the frequency-space domain the airwave data was summed across all traces, and divided by the number of traces to obtain a single average wavelet, $a(t)$. In order to remove it from the data, and improve the signal-to-noise ratio (S/N), the data was divided into the airwavelet in the frequency-space domain. This is the deconvolution in the frequency domain of the radargram $r(t)$

convolved with the filter, ie. $1/a(t)$. Following this deconvolution, a taper was applied to the data in order to remove unwanted ringing.

Average Background Subtraction

Average background subtraction techniques are some of the most common operations applied to GPR data in order to perform spatial filtering. Average background subtraction involves the calculation of the average pulse along the line, followed by the subtraction of this average pulse from every individual trace in the time-space domain. In some situations average background subtraction can be a very effective way of improving the visibility of weaker reflections. Often this method is applied in an attempt to highlight shallow reflections which are otherwise completely covered by the direct-wave. Though it is perhaps the most classic and simplistic technique for direct-wave suppression and background-noise attenuation, it has several disadvantages. It has the effect of removing horizontal linear features which run parallel to the acquisition line. It may also damage the shape of hyperbolic events, leading to incorrect interpretation of the reflection targets.

Electromagnetic Interferometry and Adaptive Subtraction

Electromagnetic interferometry (EI) was applied to three sets of common-source lines, one set collected using 250 MHz antenna and the other two with 500 MHz antenna. These lines were selected in order to estimate the direct-wave for both antennas, as well as for two different line orientations across the survey area. The output of the cross-correlation and summation over the two common-source lines in each set, is a single trace which represents an estimate of the direct-wave arrival in the data. However, given that this estimate still contains contributions from different reflection arrivals due to the cross-correlation procedure described above, a taper was applied to the direct-wave estimate in order to further isolate the direct-wave arrival. Following tapering, the direct-wave estimate is considered to be a good representation of the direct-wave throughout the dataset, assuming a relative homogeneity of the survey region.

Adaptive subtraction is performed following the prediction of the direct-wave signal by EI, a data driven technique (Liu et al., 2018; Balestrini et al., 2020). In this work we wish to estimate a shaping filter f which can minimize the objective function

$$D_{refl} = D - fD_{dw} , \tag{3.4}$$

using a least-squares fit (Liu et al., 2018). In Equation 3.4, D is the raw data, D_{dw} is the direct-wave applied to D, and f is the estimated shaping filter. To obtain the GPR data with the direct-wave subtracted D_{refl}, the convolution in time of the matching filter f with D_{dw} is subtracted from the raw data D, as shown in Equation 3.4. Here the regularized nonstationary regression technique is applied such that the matching filter behaves smoothly nonstationary.

In the process of adaptive subtraction parameters such as the filter length, time and space windows, are varied to obtain the optimal subtraction results. The three variables which we adjust in order to improve the results of the adaptive subtraction are *nshift*, *rect1* and *rect2*. The *nshift* value specifies the number of shifted windows which are tested in the time domain to match the starting position of the direct-wave to the raw data. The *rect1* and *rect2* variables specify the length of the filter window in time and space. These variables were systematically tested for lines acquired using the 250 MHz and 500 MHz antenna in order to best improve the visibility of reflection responses otherwise obstructed by the direct-wave. Testing was done through first setting the *nshift* to the maximum number of time samples, for each frequency. Then the value of *rect1* and *rect2* were varied from 10 - 40, in increments of 5, with a variety of combinations to test the effects of these parameters on the success of the technique in removal of the direct-wave. The parameter *rect1* specifies the length of the filter window in time and *rect2* the filter length in space. Following approximate filter size selection, the value of *nshift* was varied to obtain the best adaptive subtraction result, from 10 to the maximum value in increments of 10. The goal of parameter testing was to preserve the continuity and smoothness of the radargrams best while successfully removing the contribution of the direct-wave.

Resampling in dx

The choice of sample spacing (distance between measurements) or dx, is an important GPR survey acquisition parameter as it determines whether the target will be resolved under certain environmental conditions. Zero-measurements at the Almere site were taken with dx =0.05 m for all grid surveys except for one, which was set to dx =0.02 m. This unintended error provided the opportunity to demonstrate whether a choice of dx =0.05 m provides sufficient resolution through resampling of the dx =0.02 m data and comparison with the original data.

The resampling was performed by transforming the dx =0.02 m data to the frequency-wavenumber domain, and isolating wavenumbers from -10 $< k <$ 10 which corresponds to a sample spacing of dx =0.05 m. These operations are theoretically within signal theory, meaning that no data is aliased during the resampling if the data obtained with sample spacing dx =0.02 m is over sampled from a theoretical point of view. In the frequency-wavenumber domain this would mean that only zeros would be present in the wavenumbers between 10 $< k <$ 25, and -25 $< k <$ -10. In other words, the resampling is ideal if all of the information in the data sampled with $dx = 0.02$ m is contained within the wavenumbers from -10 $< k <$ 10.

The results of the resampling are presented in Figures A.1a to A.1c. The amplitudes which are present in the frequency-wavenumber domain which are outside of the k =(-10,10) interval are very small, with amplitudes less than 0.3% of the maximum value in the case of the line portrayed in Figure A.1a to A.1c, and a similar behaviour is expected from all lines in the acquired grid. This concludes that the choice of sample spacing dx =0.05 m is sufficient.

3.3.2. Ground Conductivity Meter

Gridding and display in Surfer

Gridding of the raw quadrature and in-phase response recorded by the CMD-MiniExplorer was performed in Surfer software. Kriging was selected as the gridding method to generate contour maps based on randomly spaced XYZ quadrature and in-phase data. In Kriging, each grid node positioned at X,Y is given a value Z, based on the known data points which are neighboring the node and each data point is weighted based on its distance from the node. The point Kriging with no drifts and circular search ellipse were used. The radius of the search ellipse was positioned over the collected grid. A linear variogram was selected with no nugget effects.

LIN correction

Beyond quite a low conductivity limit, most instruments exhibit a non-linear departure from true apparent conductivity with the LIN condition. This departure introduces bias and spatial distortion, and differs in extent depending on the coil configuration, instrument height and the prevailing conductivity (true conductivity) in the half-space (Beamish, 2011). Here we present a correction procedure, following a similar method to Beamish (2011); in order to obtain the same correct conductivity recording irrespective of the instrument, the prevailing conductivity in the subsurface and the measurement height.

This correction is carried out by computing the expected mutual impedance response from both coil configurations used in this investigation, HCP and VCP, given the observed apparent conductivities. The expected mutual impedance for the HCP and VCP configuration can be calculated exactly using the expression presented in Equation 2.60 and 2.61. Taking these mutual impedance values and inserting them back into the LIN equation, Equation 2.67 is used to obtain the apparent conductivities, mapping the true impedance values onto the measured values using the LIN approximation. The correction factor is then computed by dividing the measured apparent conductivities by the mapped apparent conductivities. In Figure 3.11 the correction factors are depicted for three different intercoil spacings, in both HCP and VCP orientations over the same homogeneous half-space, with conductivities ranging from 10^{-4} S/m to $10^{0.5}$ S/m. As can be seen, the correction factor is very close to 1.0 for all intercoil spacings at all conductivity values, however there is a clear increase in deviation at higher true conductivity values. This deviation is larger for larger coil offsets and for the HCP configuration in comparison to the VCP configuration. The deviation from LIN behavior is a non-linear bias which results in incorrect high values of half-space apparent conductivities.

A simple correction procedure to obtain the corrected apparent conductivities is performed by dividing the measured apparent conductivities by the correction factor. Though in this particular investigation, due to the correction factor remaining very close to unity, the variation between the corrected and measured apparent conductivities is very small. The LIN correction procedure provides an estimate of the subsurface conductivity consistent with LIN regardless of prevailing conductivity in the subsurface.

Elevation correction

The effect on the measured response due to the presence of some layer of air between the measurement device and the ground surface is significant. Here, we demonstrate the correction required to account for the instrument being held above the surface of the earth by a few centimetres, rather than placed directly on the earth's surface as is assumed when applying the LIN condition to measurements.

The elevation correction was determined through the analytical evaluation of Equation 2.72 for the HCP configuration and Equation 2.73 for VCP configuration. The Fast Hankel Transform filter table was used to extract the values of J_0 and J_1 and perform Fourier Bessel transform. Just as in the LIN correction described above, the response measured by the loops in the air over a horizontally layered conductive medium as a function of frequency is then mapped to the LIN approximation, using Equation 2.67. Thus a correction factor can be computed by dividing the true conductivity by the value calculated under the LIN approximation. The results of the correction are presented for a simulated array of conductivity values ranging from 10^{-4} S/m to $10^{0.5}$ S/m, at 5 cm and 20 cm elevation in Figure 3.11.

For the HCP configuration at 5 cm elevation the intercoil spacing pair which requires the greatest σ_a correction is the smallest separation, 0.32 m. The other coil combinations do not appear to be much at all affected by the correction from the elevation above the surface. The VCP response at 5 cm requires the largest correction factor for the smallest intercoil followed by the middle and larger separations. However, unlike the HCP response, each of the coil pairs in the VCP response were significantly impacted by the position of the instrument 5 cm above the surface. At 20 cm elevation these effects are further pronounced, for the HCP configuration now the 0.71 m separation show increased correction factor requirements as compared to the corrections at 0 m, and 5 cm. As for the VCP, a similar phenomenon occurs as the elevation increased to 20 cm the correction factor of each separation also demonstrated an increase. Though interestingly the variation across conductivity values begins to level off, the correction factor becoming nearly constant at high elevations above the ground.

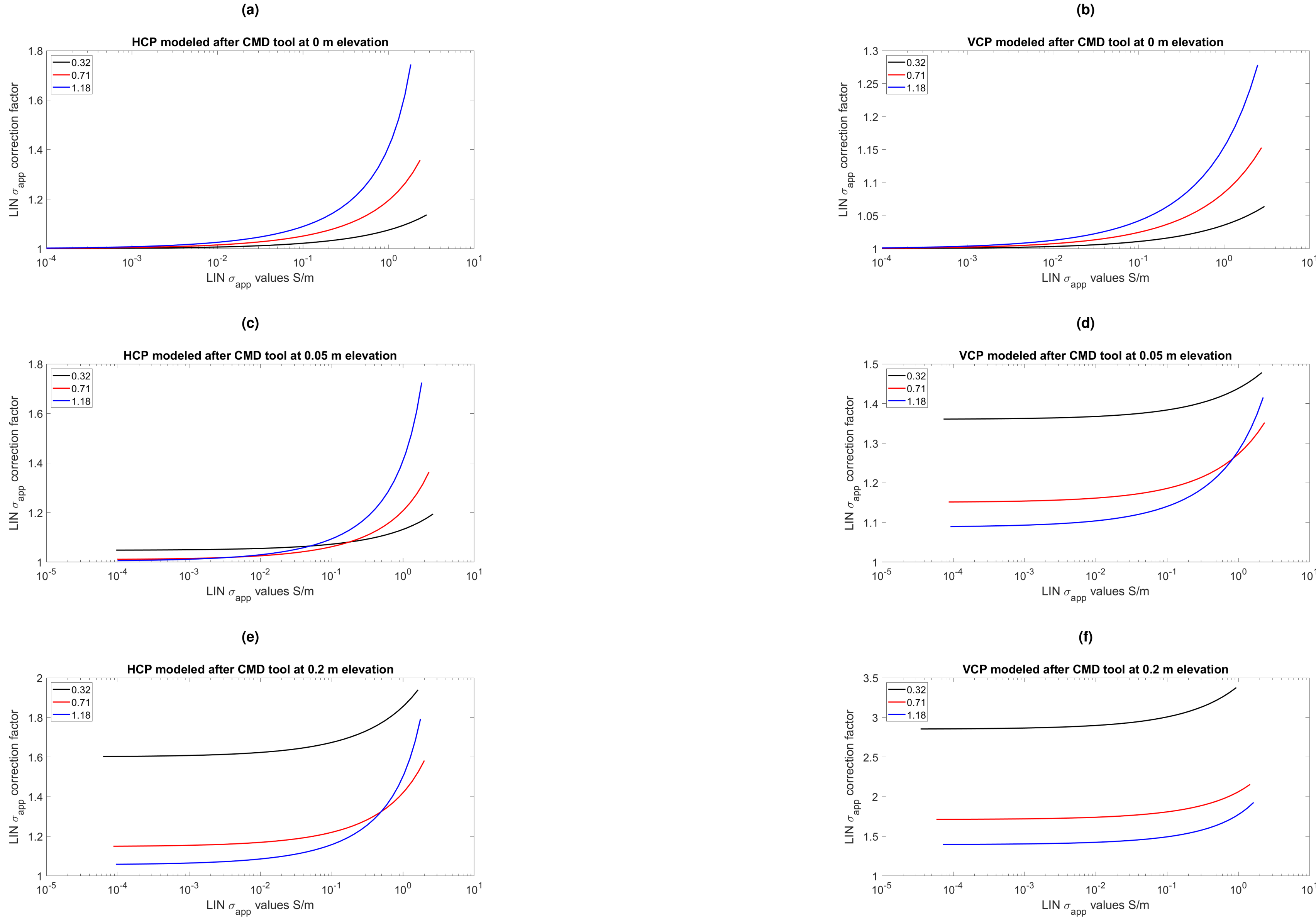

Figure 3.11: Correction procedure applied for range of σ_{app}. (a-b) Correction factor required to remove deviation from LIN approximation for the 3 intercoil spacings in HCP and VCP configuration with the CMD-MiniExplorer. (c-d) Correction factor required to remove effect of elevation from 0.05 m above the ground surface and (e-f) 0.2 m above the ground surface.

4
Results: GPR

4.1. Acquisition and Survey Parameter Settings

4.1.1. Antenna selection

In Figure 4.1 GPR lines collected on Day 2 with the NOGGIN 250 MHz and 500 MHz antenna are presented, for Line x7 perpendicular and intersecting all burials, Line y6 parallel and intersecting burial A, and Line y22 parallel and between burials. Both the 250 MHz and 500 MHz lines depict similar features in the 2D profiles. The 500 MHz radargram for Line x7, Figure 4.1c, has more hyperbolic reflection events across the profile, and overall more ringing reflections are present when compared to the 250 MHz radargram for the same line in Figure 4.1b. In Line x7, 500 MHz data hyperbolic reflections with maximum at 1.0$\times 10^{-8}$ s are present at 1.25 m, 4 m and 6.75 m, while in the 250 MHz data the only clear hyperbolic reflection is located at approximately 1.25 m consistent with the arrival times in the 500 MHz data. In Line x7 Figure 4.1b, there are clear travel time shifts in the direct-wave arrival at 1.25 m - 2 m, 3.75 - 4.75 m and 6 - 7 m, features which are less pronounced in the 500 MHz data. In Line y6 there is a strong horizontal, linear feature which appears in both the 250 MHz, Figure 4.1e, and 500 MHz data, Figure 4.1f, starting at approximately 1 m and extending to approximately 3 m at 1.25$\times 10^{-8}$ s. This feature has greater continuity in the 250 MHz data. A hyperbolic feature at 1 m intersects the direct-wave at 0.5$\times 10^{-8}$ s in Line y6 250 MHz data, which is indistinguishable in the higher frequency data. In Line y22, the data for both frequencies shows a clear, nearly continuous linear feature which extends the length of the line at 1.25$\times 10^{-8}$ s. In Line y22 there are little to no disruptions to the direct-wave of the same magnitude as in the other two lines which intersect burials.

In Figure 4.2 Day 1 timeslices for the 250 MHz and 500 MHz data are compared at 2 ns and 6 ns. In the 250 MHz data there are three very clear, high amplitude rectangular anomalies at 2 ns. Comparatively at 6 ns the 250 MHz antenna images low amplitude rectangular anomalies consistent with the position of the left-most rectangular anomaly in the 2 ns data, and a small portion of the center rectangular anomaly. At 2 ns and 6 ns in the 500 MHz data one anomalous rectangular region appears on the left side of the grid clearly at 2 ns, and very faintly at 6 ns. At 2 ns in both the 500 MHz and 250 MHz data rectangular anomalies are characterized by high amplitudes, and at 6 ns the anomalous regions are characteristically low amplitude, outlined by high amplitude linear anomalies.

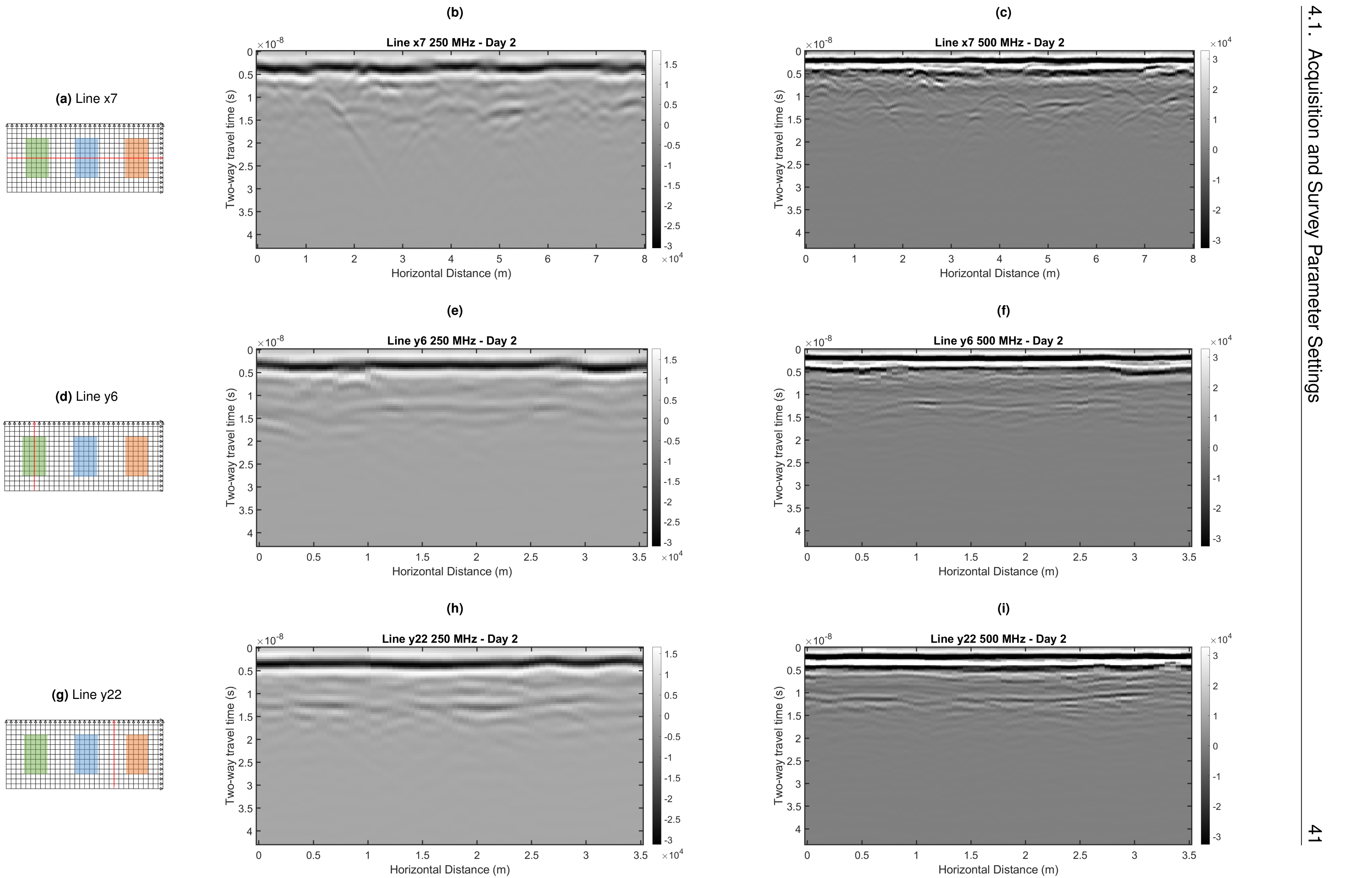

Figure 4.1: Comparing GPR lines acquired on Day 2 with NOGGIN 250 MHz antenna (middle column) and 500 MHz antenna (right column). The diagrams in the left-column depict the line (red) within the survey grid corresponding to the radargrams in the middle and right columns. (a-c) Line x7 perpendicular and intersecting all burials, (d-f) Line y6 parallel and intersecting burial A, (g-i) Line y22 parallel and between burials.

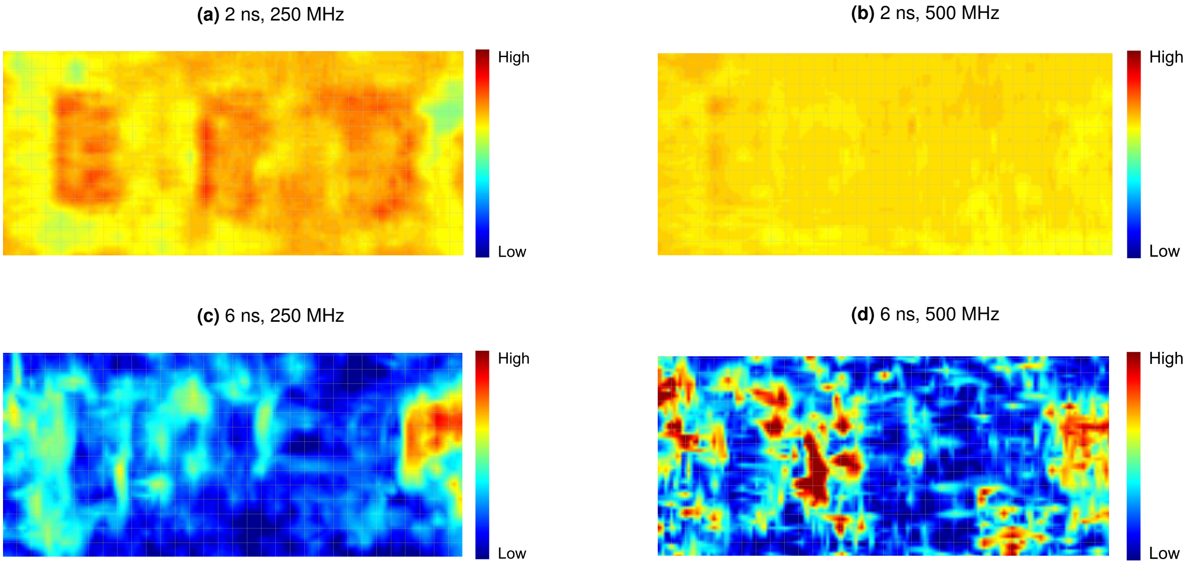

Figure 4.2: Selected Day 1 grid timeslices at 2 ns and 6 ns from 250 MHz (left column) and 500 MHz (right column) antennas. Data is enveloped to distinguish high and low amplitude reflections in EKKO_project software, the colour-bar shows the range of amplitudes from high to low.

4.1.2. Instruments

In Figure 4.3 radargrams are presented in the time-space (x-t) and frequency-space (x-f) domain acquired with the NOGGIN 500 MHz and pulseEKKO 500 MHz along Line x5, perpendicular and intersecting all burials. Though similar features are present in radargrams produced by the two instruments in the x-t domain, the direct-wave arrival in the NOGGIN data is of much higher amplitude and more continuous, with fewer distortions across the length of the profile as compared to the pulseEKKO. In the pulseEKKO data there are clear shifts in two-way travel times along the high amplitude anomaly at the earliest travel times, whereas for the NOGGIN these arrivals are fairly constant and smooth. An additional difference between the instrument recordings is that in the x-t domain the pulseEKKO scale bar is skewed towards the negatives, while the NOGGIN is centered at 0 amplitude. In the x-f domain the NOGGIN line contains contributions from higher frequencies, with the energy clearly distributed further away from the central frequency 500 MHz, with contributions from as high as 2500 MHz. The pulseEKKO has the majority of the signals energy concentrated at 500 MHz with very little contributing beyond 1000 MHz.

4.1.3. Angled grid

In Figure 4.4 250 MHz and 500 MHz 2D radargrams acquired from the angled grids on Day 4 are shown. These lines each intersect part of a single burial, A, B or C as is shown in the left-column of Figure 4.4. Features in the radargrams are much fainter in the 250 MHz data compared to the 500 MHz data. In Sq2 Line x1 and Sq2 Line x8, when the instrument intersects the position of burial B and burial C, the result is a wide hyperbolic feature peaking at 1.0 $\times 10^{-8}$ s. This feature is present in both the 250 MHz and 500 MHz data, however, in the 500 MHz data there is also significant distortion in the direct-wave above the position of the hyperbolic feature. In the 500 MHz data for Sq1 Line x7 Figure 4.4c the direct-wave is highly distorted at a horizontal position of 0.5 m along the profile, which appears to form a hyperbolic event. For the 250 MHz antenna presented in Figure 4.4b this distortion is imperceptibly faint.

For many of the other lines in the angled grids the distinguishing feature which coincides with the burial presence is either the disruption of a flat lying horizon at 1.1$\times 10^{-8}$ s - 1.25$\times 10^{-8}$ s, or the presence of a high amplitude flat feature at 1.1$\times 10^{-8}$ s - 1.25$\times 10^{-8}$ s. For reference, a few additional lines are presented in Figure A.7 in Appendix A.

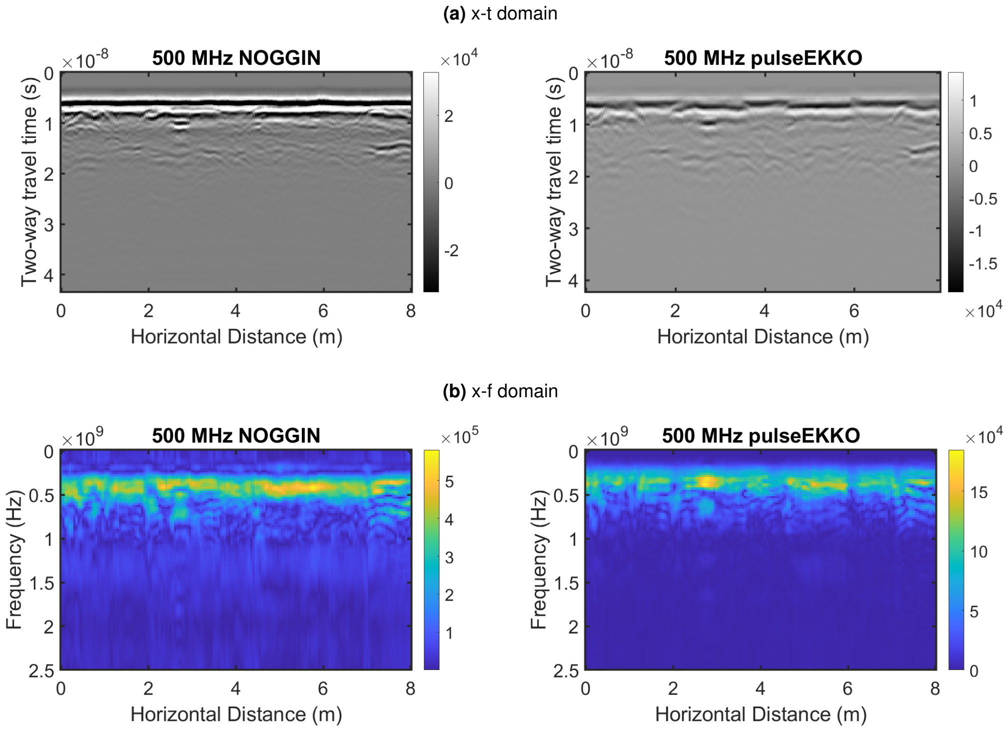

Figure 4.3: GPR measurements along Line x5 (perpendicular and intersecting all burials) using the NOGGIN 500 MHz and pulseEKKO 500 MHz displayed in x-t domain and x-f domain. The colour-bars present the amplitude of the recorded signal.

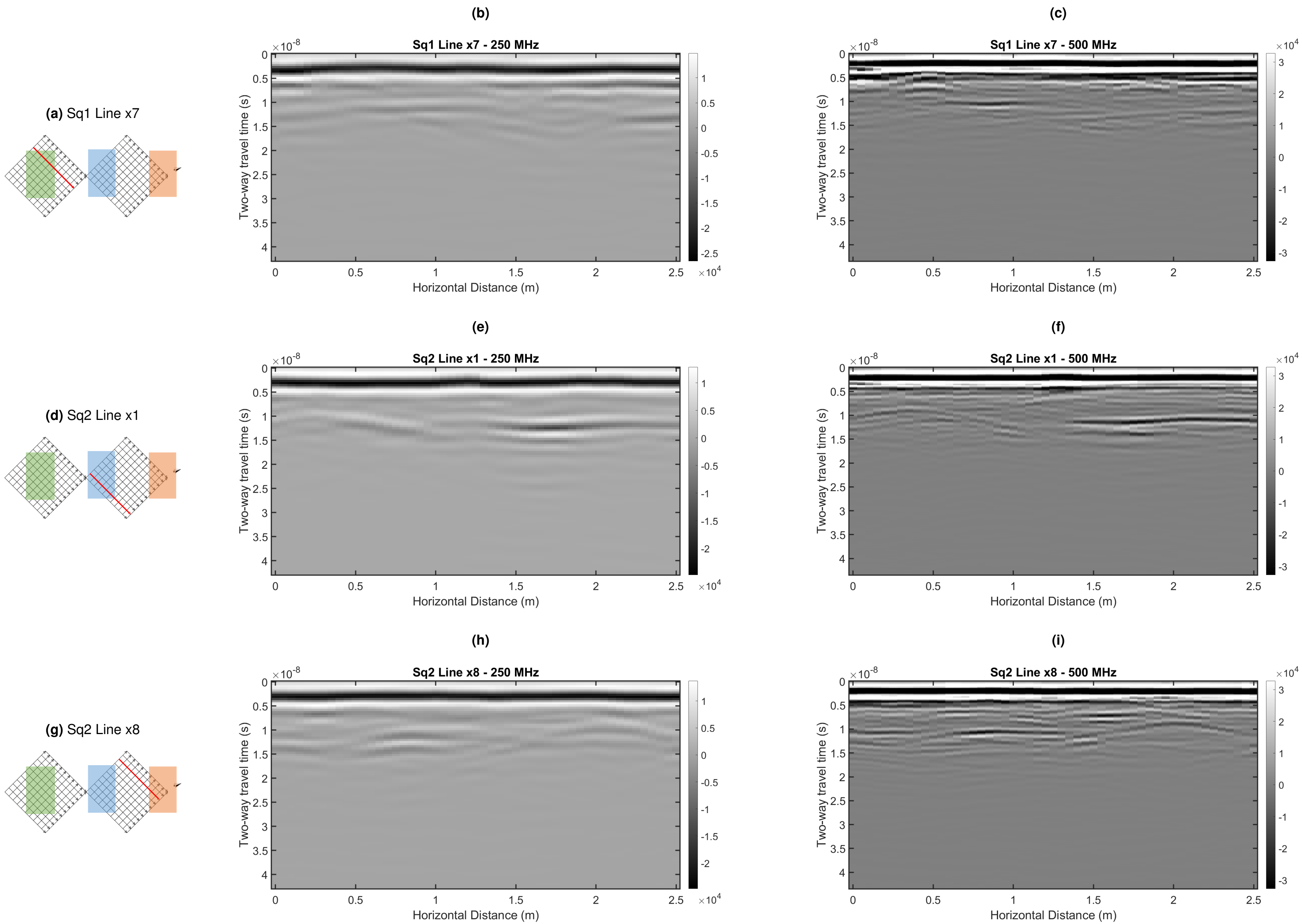

Figure 4.4: Angled grid GPR lines with NOGGIN 250 MHz antenna (middle column) and 500 MHz antenna (right column). The diagrams in the left-column depict the line (red) within the survey grid corresponding to the radargrams in the middle and right columns. (a-c) Sq1 Line x7 intersecting burial A, (d-f) Sq2 Line x1 intersecting burial B, (g-i) Sq2 Line x8 intersecting burial C.

Timeslices of interest from the angled grids acquired with both 250 MHz and 500 MHz NOGGIN antennas are presented in Figure 4.5. In the first timeslice, at 1 ns, both the 250 MHz and 500 MHz faintly image a rectangular anomaly on the left, in Sq1. For the 250 MHz data the leftmost rectangular silhouette becomes very clear in the 2 ns timeslice, and faintly in the 500 MHz data 2 ns timeslice. The rectangular anomaly doesn't reappear again until 6 ns, and then at 10 - 12 ns in both the 250 MHz and 500 MHz data. For this leftmost rectangular anomaly, from both frequencies, the response is characterized primarily by a high amplitude anomaly with respect to background features. While for anomalies which appear in Sq2, on the right, the response is much more faint, with patterns appearing in the form of the absence of an anomaly. This is also in agreement with 2D GPR line observations in Figure 4.4 and Figure A.7 wherein lines in Sq1 have reflection features which appear as a high amplitude flat anomalies at approximately 11.0 - 12.5 ns, in addition to at earlier times in the distortion of the direct-wave. Whereas in Sq2, anomalies appear as the absence of a high amplitude flat event at approximately 11.0 - 12.5 ns. Rectangular anomalies in Sq2 appear very faintly in the 250 MHz first at 2 ns, with the border of the rectangles recorded as high amplitude events.

4.2. Survey Environment

The clearest distinction between the recorded response in wet versus dry conditions is shown in the 250 MHz data presented in Figure 4.6. The 500 MHz data is placed in Appendix A in Figure A.8 for reference. In Figure 4.6 GPR data collected on Day 1 and Day 2 with 250 MHz antenna is compared for Line x10 (perpendicular and intersecting all burials) Figure 4.6b-4.6c, Line y11 (parallel and between burials) Figure 4.6e-4.6f and Line y28 (parallel and intersecting burial C) Figure 4.6h-4.6i. In Line x10 there is a change in the arrival time of the direct-wave, with earlier arrivals occurring between 1.25 - 2 m, 3.5 - 4.5 m and 5.25 - 7 m. These jumps in the two-way travel time, and their positions along the length of the profile, are much clearer and more distinct in the Day 2 wet data presented in Figure 4.6c. Additionally, hyperbolic features are distinguishable directly under the positions of the earlier signal arrival times at $1.20{\times}10^{-8}$s in both wet and dry data. Line y11, which runs between burials, in parallel, demonstrates a horizontal linear horizon at $1.25{\times}10^{-8}$s in Day 2 data which is much more continuous and of higher amplitude than the same feature response in Day 1 data. Lastly, Line y28 is presented in Figure 4.6h and 4.6i which intersects a single burial, burial C, in parallel. In both Day 1 and Day 2 data the position of the burial is consistent with the absence of a linear horizontal feature at 1.0 - $1.25{\times}10^{-8}$s, from 1 - 3 m, and the presence of a hyperbolic reflection centered at 2.25 m, with it's peak touching the bottom of the direct-wave at $0.5{\times}10^{-8}$ s. These features are evident in both Day 1 and Day 2 data.

In Figure 4.7 timeslices from Day 1 and Day 2 collected with the NOGGIN 250 MHz antenna are displayed. The 500 MHz data is placed in Appendix A in Figure A.9 for reference. The timeslices which are presented are those in which anomalous features were identified. In general the timeslices from Day 2 produce much clearer anomalous features, in nearly all of the timeslices with the exception of the 2 ns timeslice. Both the Day 1 and Day 2 data exhibit similar patterns at respective times, in particular at 11 ns and 12 ns the response is very similar, with a high amplitude background feature extending from the right of the grid towards the center. However, in general the "wet" environment on Day 2 generated data which demonstrates less cluttered and cleaner timeslices, which allow the anomalous features to be highlighted. This is evident in timeslice 12 ns (Figure 4.7l) wherein there is a clear linear high amplitude response on the left of the grid in Day 2 data, whereas the signature is much less localized in the Day 1 data (Figure 4.7k). This same effect is evident in the 6 ns timeslice as well, wherein clear rectangular shapes are present in the Day 2 data (Figure 4.7f), and only a single shape emerges on the left side of the grid in the Day 1 data (Figure 4.7e). Interestingly, on the right hand side of the Day 2 grid at 6 ns in Figure 4.7f it appears as though the right hand rectangle is extending up towards the left in a less structured form. These details are not apparent in the Day 1 data. Rectangular anomalies appear in the form of high amplitude signatures (e.g. Figure 4.7f) as well as in the form of the absence of a response (e.g. Figure 4.7h), across the timeslices.

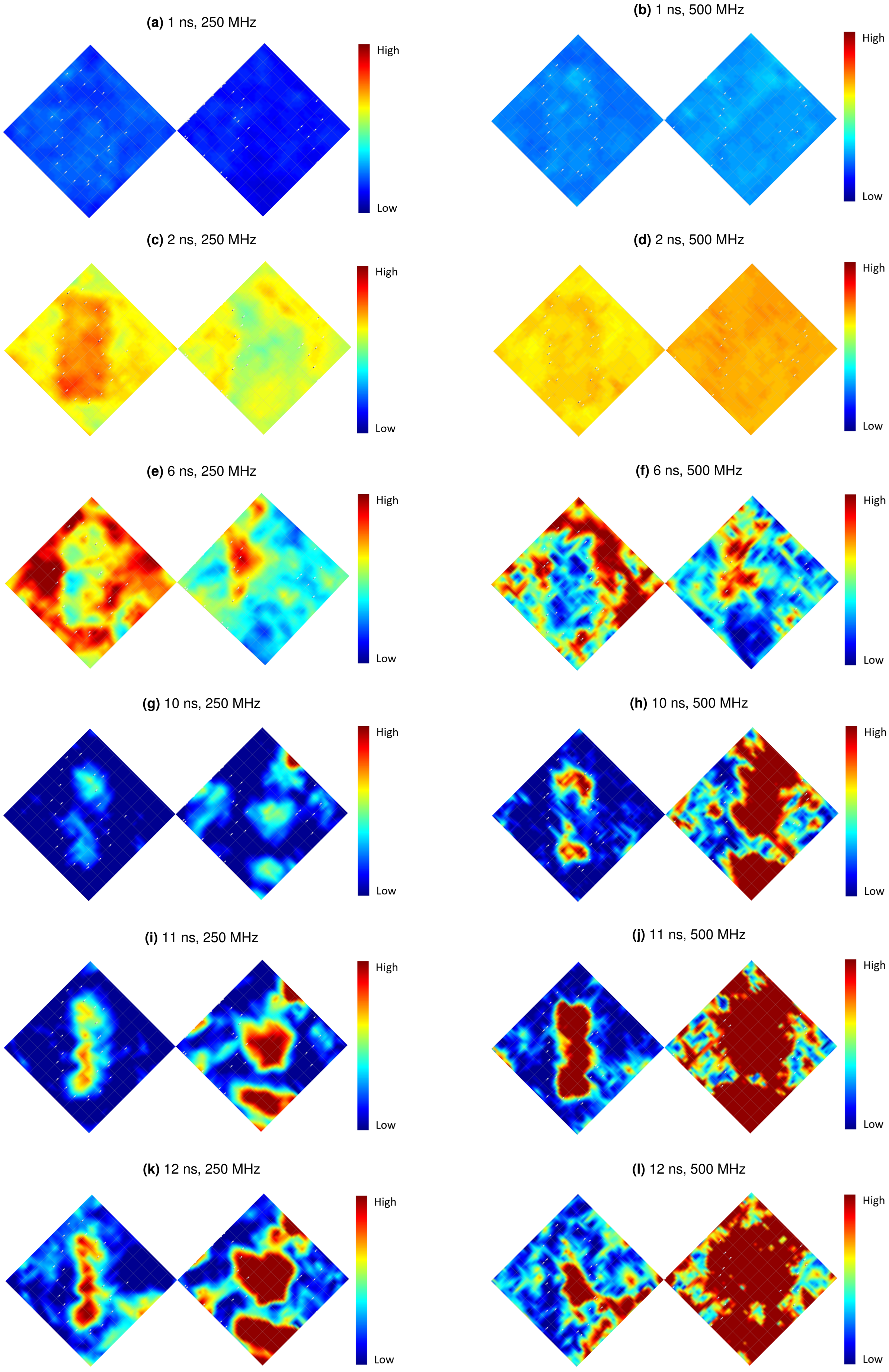

Figure 4.5: Selected angled grid timeslices from the 250 MHz (left column) and 500 MHz (right column) antennas. Data is enveloped to distinguish high and low amplitude reflections in EKKO_project software, the colour-bar shows the range of amplitudes from high to low. White points indicate the approximate position of the burials from visual inspection on the surface.

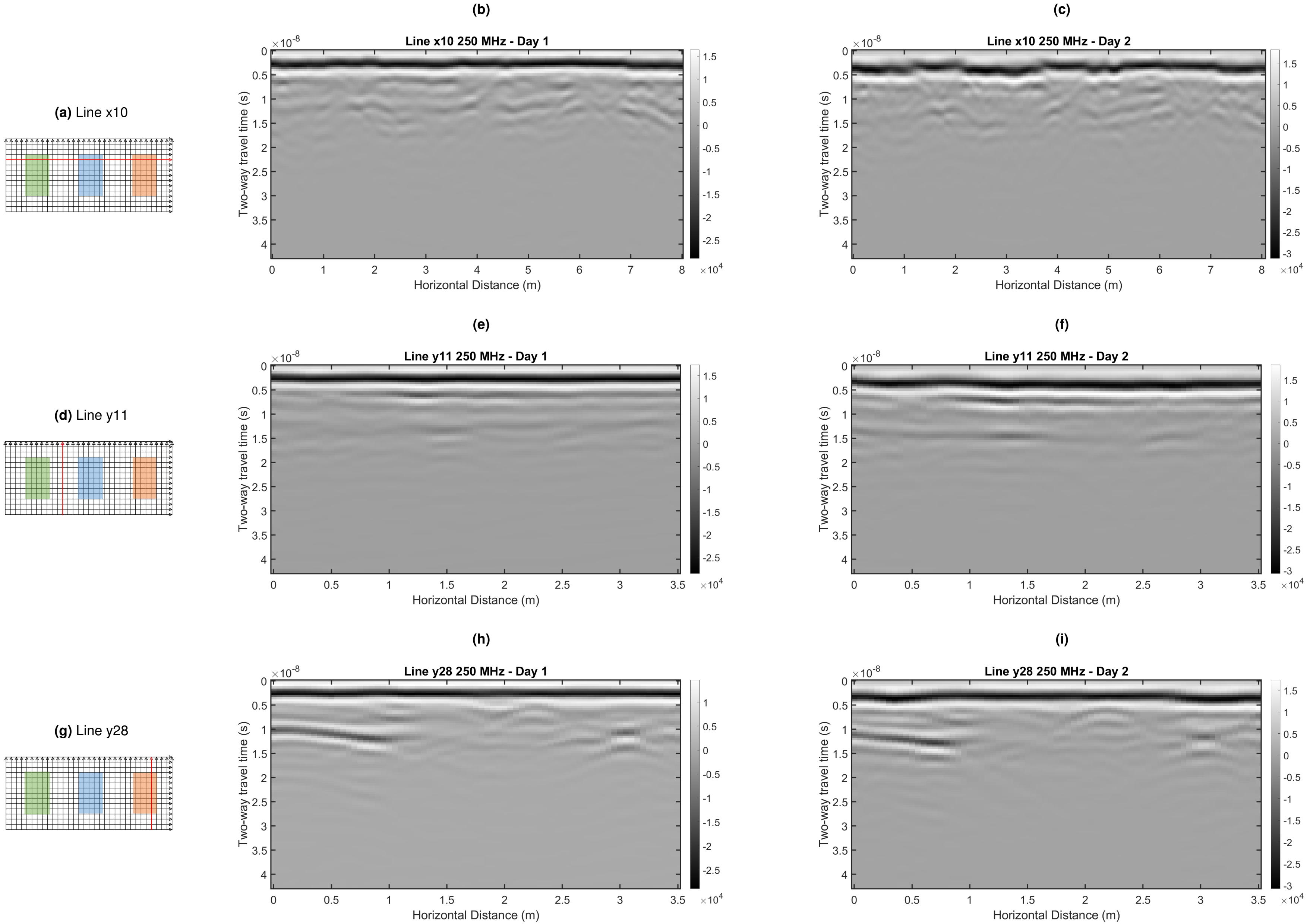

Figure 4.6: Comparing GPR lines acquired on Day 1 in dry conditions (middle column) versus Day 2 in wet conditions (right column) with the NOGGIN 250 MHz antennas. The diagrams in the left-column depict the line (red) within the survey grid corresponding to the radargrams in the middle and right columns. (a-c) Line x10 perpendicular and intersecting all burials, (d-f) Line y11 parallel and between burials, (g-i) Line y28 parallel and intersecting burial C.

4.3. Processing techniques

4.3.1. Airwave removal

A 2D GPR profile in the time-space domain which has been deconvolved with the airwave exhibits a number of changes, as is demonstrated in Figure 4.8. The airwave, which was measured using the NOGGIN 250 MHz antenna, is presented in Figure A.2a. The $a(t)$ wavelet with and without the taper applied can be found in Figure A.2b. The airwave measured using the 500 MHz antenna was unusable due to extensive ringing effects.

The first difference observed in Figure 4.8 is that the amplitudes have increased by a factor of 200, which is a result of the deconvolution process. In addition, the range of values has shifted from negative towards positive. This is an effect wherein the deconvolution has sharpened a mexican hat wavelet into a single pulse. Following deconvolution the source signal is zero phase, meaning that it is time symmetric. As a result there is some signal occurring at the bottom of the profile which corresponds to some negative time. There is no evidence of increased resolution of reflection events due to the sharpening of the wavelet.

4.3.2. Average background subtraction

In Figure 4.9c and Figure 4.9d results from the average background subtraction procedure performed on Line y28 250 MHz data and Line x7 500 MHz data are shown alongside raw data in Figures 4.9a and 4.9b. The average trace which was subtracted from the raw data to obtain Figures 4.9c and Figure 4.9d is presented in Appendix A Figure A.3. In the raw data for Line y28 there is a hyperbolic event which intersects the direct-wave at 0.75$\times 10^{-8}$ s and 2.1 m, this anomaly is partially obstructed by the direct-wave. In the raw data for Line x7 differences in arrival times of the signal can be distinguished, which manifests in such a way that the linear continuation of the direct-wave is disturbed. The character of the reflection events which are causing the distortion of the direct-wave are obstructed and cannot be distinguished due to the presence of the direct-wave. In Figure 4.9c the direct-wave is suppressed, and features below 0.5$\times 10^{-8}$ s are retained from Figure 4.9a. The wide parabola at 0.75$\times 10^{-8}$ s and 2.1 m is better resolved from the background, and a linear feature is present connecting the high amplitude horizontal linear features at 1.25$\times 10^{-8}$ s. In Figure 4.9d the direct-wave is fainter than in Figure 4.9b, however it is still present, and no new features can be distinguished at depth or in the near-surface. The continuity of the horizontal and hyperbolic reflections occurring at 1.25$\times 10^{-8}$ s is more pronounced and connected after background average subtraction, this is evident in Figure 4.9d.

4.3.3. Electromagnetic Interferometry and Adaptive Subtraction

In Figure 4.9e and Figure 4.9f results from the adaptive subtraction of the direct-wave estimated using EI performed on Line y28 250 MHz data and Line x7 500 MHz data are shown. The common-source lines were obtained along Line x10 for both the 250 MHz and 500 MHz antenna results presented in Figure 4.9e and Figure 4.9f, and the resulting direct-wave estimates obtained through EI are presented in Figure A.4 in Appendix A. Additional adaptive subtraction results for lines x10, y6 and y22 acquired with 250 MHz and 500 MHz antenna are included in Appendix A Figure A.5 and Figure A.6.

The parameter values for the quantities *nshift*, *rect1* and *rect2* used to obtain the adaptive subtraction results in this work were determined through systematic testing, and were maintained constant for all lines acquired with the same antenna, 250 MHz or 500 MHz respectively. Testing was done through first setting the *nshift* to the maximum number of time samples for each frequency and adjusting the values of *rect1* and *rect2*. The effect of lengthening *rect1* resulted in the direct-wave estimate being matched to random features at later times in the profile. Shortening *rect1* prevented this from occurring, though a very small value of *rect1* resulted in some loss of information along the y-direction. The effect of lengthening *rect2* resulted in increased smoothness in the x-direction, though large contributions from the direct-wave remained in many of these cases. Conversely, shortening *rect2* often resulted in discontinuities and choppy features in the x-direction, though the direct-wave was removed to a high degree. Finding a compromise between smoothness in the x-direction while ensuring the successful removal of the direct-wave through adjusting the values of *rect2* had the greatest effect on the adaptive subtraction result. Once the approximate ideal filter size was determined the value of *nshift* was varied and selected, such that the starting position of the direct-wave estimate was matched accurately to the raw data. The values selected in this work for the 250 MHz lines were *nshift* = 40, *rect1* = 25 and *rect2* = 20 and for the 500 MHz lines were *nshift* = 60, *rect1* = 35 and *rect2* = 15.

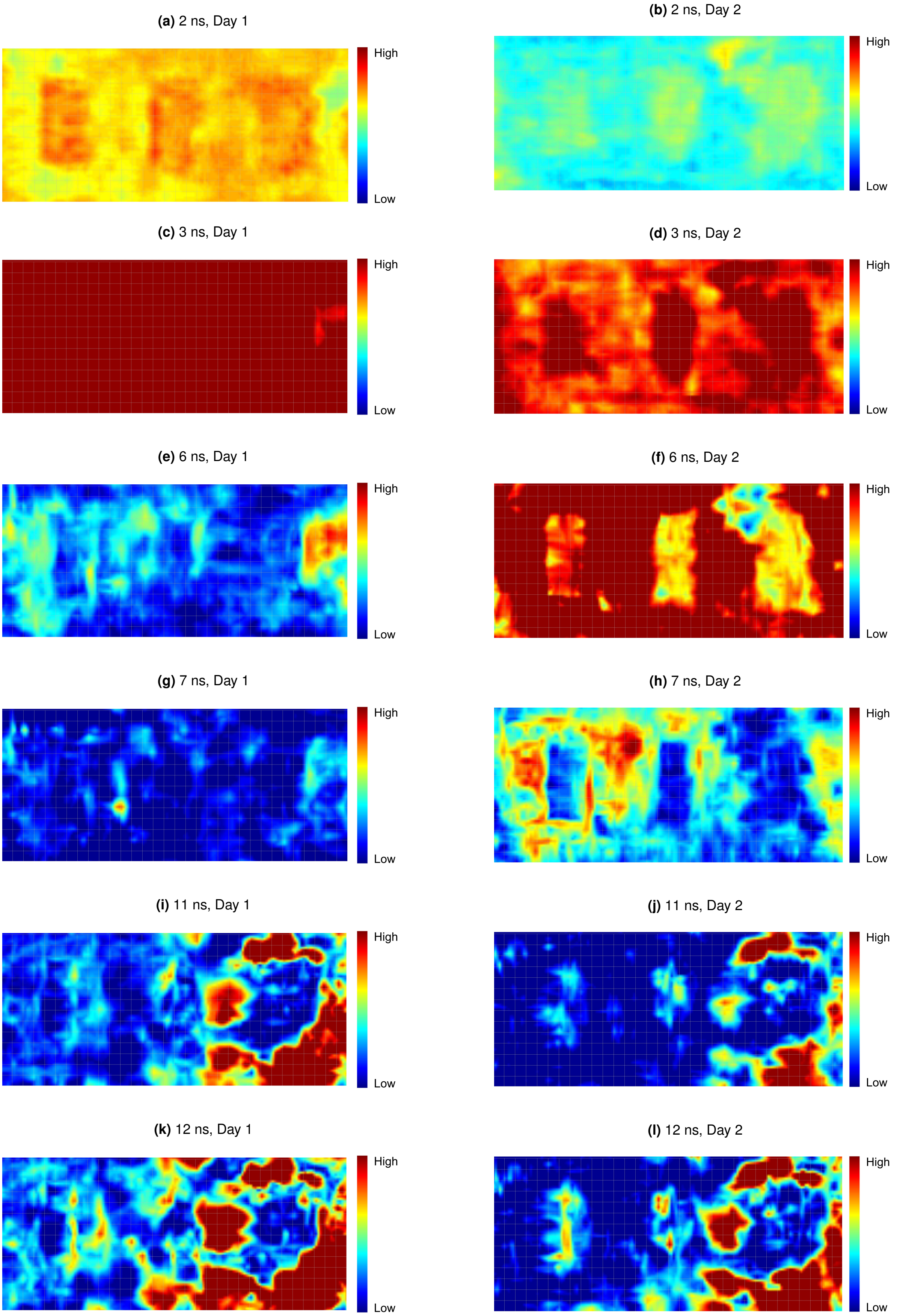

Figure 4.7: Comparing timeslices from Day 1 in dry conditions (left column) and Day 2 in wet conditions (right column) acquired with NOGGIN 250 MHz. Data is enveloped to distinguish high and low amplitude reflections in EKKO_project software, the colour-bar shows the range of amplitudes from high to low.

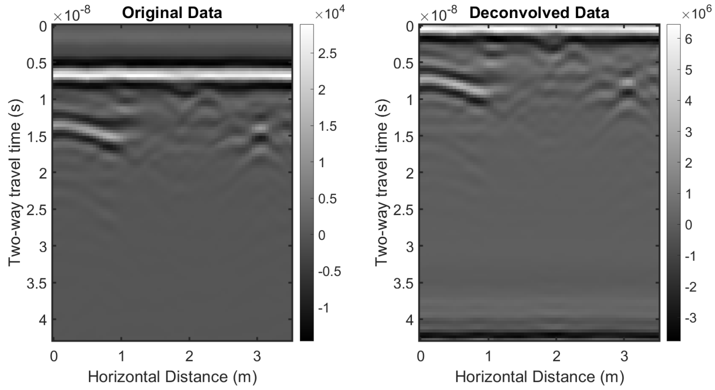

Figure 4.8: Line y28 250 MHz data with inverse filter spiking deconvolution (airwave removal) applied (right) alongside raw "original" data (left).

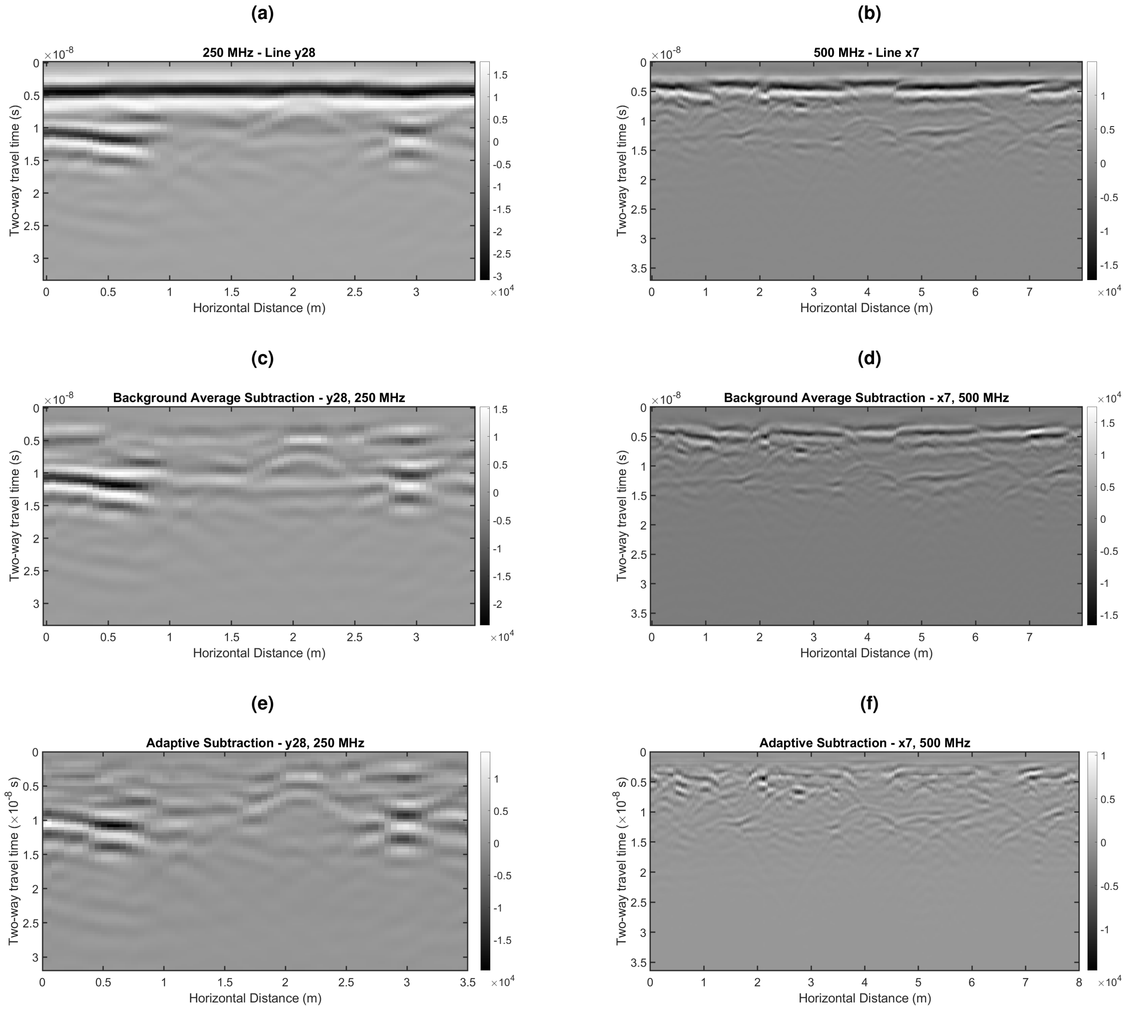

Figure 4.9: Comparing (a-b) raw data to the application of (c-d) average background subtraction and (e-f) adaptive subtraction on 250 MHz (left column) and 500 MHz (right column) GPR line data collected on Day 3. Two different lines are displayed, 250 MHz Line y28 (left column) parallel and intersecting one burial, and 500 MHz Line x7 (right column) perpendicular and intersecting all burials.

In Figure 4.9e the direct-wave has been subtracted from the data, improving the contrast between the hyperbolic event at 0.75$\times10^{-8}$ s and 2.1 m, and the background noise. The shape of the hyperbola is sharpened, with steeper limbs. Figure 4.9e does not exhibit the same continuity as in Figure 4.9c between the two high magnitude horizontal anomalies at 1.25$\times10^{-8}$ s. Overall the continuity between traces is reduced. In Figure 4.9f the direct-wave which was clearly present in both Figure 4.9b and 4.9d is subtracted to a high degree. Features which were disturbing the direct-wave can be clearly distinguished at x = 1.5 m, 4.25 m and 6.75 m. These features are characterized by sloping parabola limbs at 0.45$\times10^{-8}$ s in addition to parabolic and horizontal reflections positioned at 1$\times10^{-8}$ s, with little to no continuity. There is a much higher level of detail in the near surface following adaptive subtraction, in both Figure 4.9e and Figure 4.9f, features are present which are indistinguishable in the raw and average background subtracted data.

In Figure 4.10 the results of adaptive subtraction from direct-wave estimates obtained from common-source lines made along Line y11 (parallel and between burials), applied to Line y22 (parallel and between burials) and Line x5 (perpendicular and intersecting burials) are compared alongside the results of adaptive subtraction from direct-wave estimates made along Line x10 (perpendicular and intersecting burials), applied to Line y22 and Line x5. The common-source lines obtained along Line y11 for the 500 MHz antenna and the resulting direct-wave estimates obtained through EI are presented in Figure A.4 in Appendix A for reference. There are no clear observable differences between the estimated direct-wave subtraction taken from the same line orientation i.e. Figure 4.10a Line y11 subtracted from Line y22, versus opposite line orientations ie. Figure 4.10c Line x10 subtracted from Line y22. Both are successful in the removal of the direct-wave to a high degree.; however, differences do exist. The difference between Figure 4.10a and Figure 4.10c, and Figure 4.10b and Figure 4.10d is shown in Figure 4.10e and 4.10f respectively. The amplitude of the difference in Figure 4.10e is <10% the maximum amplitude in the radargrams, and the difference in Figure 4.10f is <25% the maximum amplitude in the radargrams. In Figure 4.10e and 4.10f there does appear to be some pattern which results from the subtraction of the two radargrams, though no clear features can be distinguished from them. Variations do exist as well between the direct-waves estimated from Line y11 versus Line x10, as shown in Figure A.4.

(a) Direct-wave estimate from Line y11 subtracted from common-offset Line y22.

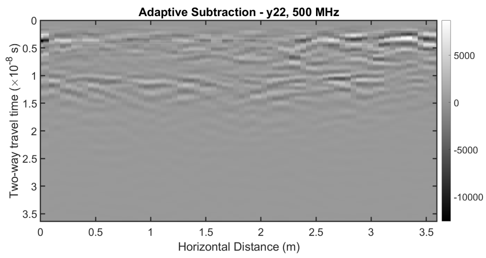

(b) Direct-wave estimate from Line y11 subtracted from common-offset Line x5.

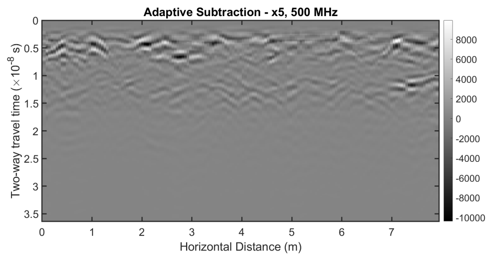

(c) Direct-wave estimate from Line x10 subtracted from common-offset Line y22.

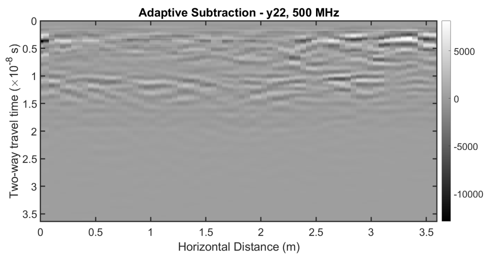

(d) Direct-wave estimate from Line x10 subtracted from common-offset Line x5.

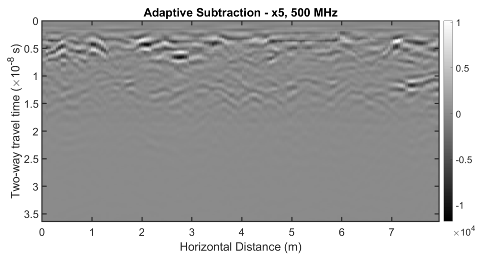

(e) Difference, Line y22

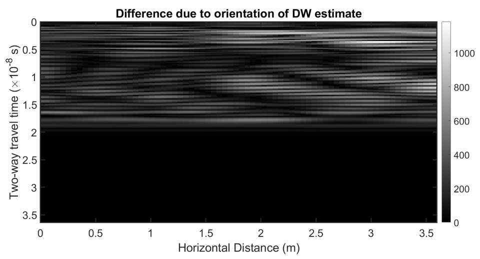

(f) Difference, Line x5

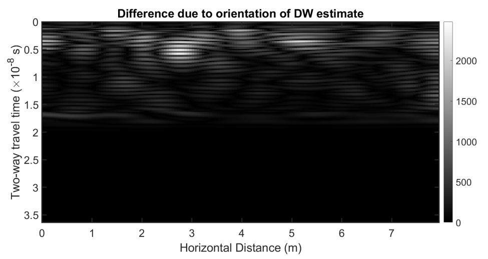

Figure 4.10: Comparing the efficacy of the adaptive subtraction of direct-wave estimates from common-source gathers acquired along the same or opposite direction to the common-offset line being processed. (a) Line y11 (dw) and Line y22 (radargram) are the same direction, (b) Line y11 (dw) and Line x5 (radargram) are opposite directions (c) Line x10 (dw) and Line y22 (radargram) are opposite directions (d) Line x10 (dw) and Line x5 (radargram) are the same direction. In (e-f) the difference between adaptive subtraction results on (e) Line y22 and (f) Line x5 using direct-wave estimate from common-source gathers acquired along Line y11 and Line x10. The absolute value of the difference was taken. DW = direct-wave. Acquired using 500 MHz pulseEKKO antenna.

5
Discussion: GPR

How can the detectability of simulated clandestine burials be influenced by acquisition and survey parameter settings?

A very important consideration in the acquisition of GPR data for the detection of clandestine burials, is the selection of central antenna frequency. Comparing data acquired with a 250 MHz antenna and 500 MHz antenna, has revealed that in this environment there are a number of benefits and drawbacks of both. First, the 500 MHz data provides a higher resolution look at the near surface, this manifests in the form of clear and continuous hyperbolic features positioned at a two-way travel time of approximately 1.0×10^{-8} s (10 ns) consistent with the burial positions, as shown in Figure 4.1c, Line x7 acquired with the NOGGIN. Assuming an approximate subsurface radar wave velocity of 0.1 m/ns, the position of the material contrast resulting in these hyperbolic features is at a depth of 0.5 m, consistent with the center of the burials. That being said, larger and more easily distinguishable hyperbolas are present in the 250 MHz Line x7 data in Figure 4.1b at a position consistent with burial A. Additionally, the clear travel-time jumps in Figure 4.1b over the burial positions are an obvious indication of the presence of the simulated clandestine burials. These travel-time jumps do not exist as prominently in the 500 MHz data due to the very high amplitude direct-wave contribution, which obscures many of the early arrivals. It might appear as though the jumps in two-way travel time in the 250 MHz data are a result of abrupt changes in topography over the burials. However, the result of topography would be unlikely to result in the observed features, but rather the shift of features horizontally due to adjacent rays traversing the same swath of ground. The 250 MHz data might be exhibiting some effects of topography when compared to the 500 MHz data due to increased penetration depth increasing the likelihood of adjacent rays crossing, however there does not appear to be significant distortion in subsurface features within the data. In this case, the distinguishing attributes in the shallow subsurface are unlikely to be affected by topographic effects as the topography variation was minimal and the travel-time shifts are significant.

Hyperbolic features at 0.5 $\times10^{-8}$ s (5 ns) in Line y6 Figure 4.1e, indicating the onset of burial A, are not detected in the 500 MHz data. Assuming a subsurface velocity of 0.1 m/ns these hyperbolic events are due to material contrasts at 0.25 m, the expected depth to the top of the cadaver. Comparing Line y6 intersecting burial A and Line y22, between burials, both the 250 MHz data and 500 MHz data show a distinction between the linear horizontal feature at 1.25×10^{-8} s (12.5 ns) in Line y22 consistent with a soil horizon, assuming a subsurface velocity of 0.1 m/ns at 0.625 m depth, and Line y6 which exhibits discontinuities at the onset (1 m) and the end (3 m) of burial A along the line. Overall it appears that the 250 MHz data, though imaging with lower resolution, provides a cleaner, easier to interpret image than the 500 MHz data. A single hyperbolic event or continuous horizontal reflecting feature indicates the location of the burials in the 250 MHz data, features which might be missed due to cluttered images and discontinuous features in 500 MHz data.

The same is observed comparing the two antennas in timeslice data from Figure 4.2. The 500 MHz data is cluttered with reflections and the amplitude of the direct-wave obscures early events prohibiting the identification of burials, characterized in timeslices by rectangular anomalies. These observations differ from some previous studies which recommend the use of high frequency antennas (400-500 MHz) to detect clandestine burials due to high resolution and shallow depth of penetration (Schultz, 2007; Schultz and Martin, 2011; F. Hansen, 2019). However, other works have also found the use of lower frequency antennae (110 - 250 MHz) superior for detecting burials, limiting extensive clutter in the detected response (Nobes, 1999; Pringle, Jervis, Hansen, et al., 2012), as was shown to be a large benefit in this work.

In addition to antenna central frequency, the choice of GPR instrument has been found to have some implications for the level of success achieved in the detection of clandestine burials. Data collected by the pulseEKKO and NOGGIN showed very high consistency of features along each line, validating the reflection events which are being presented in this work. However, there were some differences in the two datasets, primarily in the 500 MHz data, as presented in Figure 4.3 for comparison. In Line x5, and all other lines collected with the NOGGIN, the direct-wave exhibits a high amplitude and as a result obstructs the reflection events arriving at the receiver between two-way travel times of 0.25$\times 10^{-8}$ s (2.5 ns) and 0.75$\times 10^{-8}$ s (7.5 ns). There is evidence that some reflections are distorting the direct-wave, but the character of these reflections is lost. Conversely, in the same line collected by the pulseEKKO, very clear jumps in the arrival times of the first arrivals, coinciding with the burial positions, can be identified as the direct-wave is fainter in amplitude. The skewing of the pulseEKKO data towards negative values indicates that the direct-wave is less significant, thus the image lacks balance in the amplitude values. The source of these differences is likely shielding and mounting of the antennas. The pulseEKKO antenna is much larger, suggesting that the shielding may be superior with this instrument. In addition, given that the pulseEKKO is dragged along the ground rather than pushed in the SmartCart like the NOGGIN, the ground coupling of the pulseEKKO is likely better. The antennas on the NOGGIN are attached to a baseplate which on uneven ground might result in tilting and lifting up from the ground surface, reducing ground coupling and making the recordings vulnerable to high amplitude direct-wave contributions. These effects are also evident in the frequency plot in Figure 4.3b, wherein the NOGGIN data has contributions from much higher frequencies, and has a less concentrated signal around the central frequency than the pulseEKKO, indicating that the NOGGIN antenna is less sufficiently shielded from high frequency content. Thus, in theory the pulseEKKO is the preferred instrument for data acquisition in this environment. However, given the many advantages of the speed of acquisition using the NOGGIN with SmartCart, for use in police investigations, the NOGGIN is much more advantageous.

On survey Days 1, 2 and 3 data was collected perpendicular and parallel to the known positions of the burials, as discussed above. However, in a real forensic investigation where by definition the positions of clandestine burials is unknown, the likelihood of intersecting burials at 90° is very low. Thus, the importance of studying the detection of simulated clandestine burials through oblique intersection is of high importance and interest. The findings from the radargrams in Figure 4.4 are representative of the other lines in the grid which can be found in Figure A.7 in Appendix A, demonstrating that both the 250 MHz and 500 MHz antenna can detect the simulated clandestine burials to some degree at oblique angles. Over burial A the response from Line x7 in Figure 4.4b is a high amplitude linear feature at 1.25 $\times 10^{-8}$ s (12.5 ns), and in the 500 MHz data the burial response also appears as a strong distortion in the direct-wave arrivals at 0.5 $\times 10^{-8}$ s (5 ns). For burials B and C the detection of the burial is characterized by the termination of the high amplitude horizontal event and the presence of a wide hyperbolic feature peaking at 1 $\times 10^{-8}$ s (10 ns), assuming a velocity of 0.1 m/ns has a source at 0.5 m depth. These depths are consistent with the position of the cadavers which are expected to be positioned between 0.3 m to 0.6 m below the surface. When looking at adjacent lines intersecting burial A, a side-by-side pattern emerges which suggests that the linear flat feature moves with the position of the burial across the grid. However, this might be a difficult feature to distinguish without knowing the position of the burials beforehand, looking at the radargrams alone.

The timeslices presented in Figure 4.5 image the position of burial A with high efficacy, but burials B and C to a much lesser extent. The 250 MHz antenna images burial A effectively at earlier times, with the 500 MHz data suffering from more noise and clutter in the signal. As mentioned previously burial A is characterized by a horizontal high amplitude anomaly of length 1 m at approximately 0.625 m depth in radargrams, while the other two burials were characterized by the absence of this horizontal anomaly, and the presence of a faint wide hyperbola peaking at approximately 0.5 m depth. The variability of characteristic GPR response shown here highlights the importance of the use of both radargrams and timeslices for analysis. Examining 2 ns timeslice, for the 250 MHz, the border of the burial has a zig-zag effect due to the intersection of the GPR lines with the grave border, in Day 1 and 2 surveys this edge is straight, and thus the zig-zag border is characteristic of oblique intersection with the burial. Likely burial A is easier to detect in timeslices due to the burial being covered entirely by the survey grid, thus improving the interpolation of reflection events in the timeslice data. Given that burial A is 20, and 40 days younger than burial B and C respectively, there may be a difference in contrast between the grave-fill and surrounding soil due to time since burial (PDI). In the literature, numerous authors have found evidence to suggest that overtime detection of simulated clandestine burials decreases due to a decrease in contrast between grave-fill and surrounding soil (Pringle et al., 2020; Schultz and Martin,

2012) though this was observed over the course of years, not months. What is important to note is that the characteristic response of the burials varies, and may take on a range of different anomaly forms. The importance of high data coverage when searching for clandestine burials is highlighted by the observations in Figure 4.5 wherein the identification of burial B and C is much more difficult, while burial A is evident and the response easier to characterize.

The GPR radargram characteristic response from simulated clandestine burials reported in the literature range from 1/2 hyperbolic reflections (J. D. Hansen et al., 2014), to full hyperbolic reflections for lines perpendicular to burials and long dense reflections for lines parallel to burials (Schultz and Martin, 2011). In timeslices, Molina et al. (2016) recorded burials which appear as rectangular shaped anomalies. The response from simulated clandestine burials in this work contributes to the list of possible reflection events resulting from clandestine burials in GPR, while also supporting the results presented in previous literature. Due to the absence of buried artefacts in clandestine burials, based on the results presented in this work, and supported by previous work (Van Schoor et al., 2017), it is thought that the largest contribution to the burial anomaly is the disturbed burial zone, and not the cadaver itself. Hyperbolic reflections which were recorded at 0.25 - 0.5 m depth might be resulting from the presence of the cadaver inside the burial. However, in order to fully confirm this suspicion, future work must compare the detection of an empty burial versus one containing a cadaver in an environment characteristic to The Netherlands.

How does the survey environment affect the detectability of simulated clandestine burials?

A feature which was found across all radargrams, and which acted as a marker for the detection of the burials in a number of cases, is the linear, horizontal high amplitude feature at 1.25 $\times 10^{-8}$ s (12.5 ns). This feature functioned to highlight the position of the burials by both it's presence (Figure 4.6e, Line y11) and absence (Figure 4.6h, Line y28). It is present between burials, and within burials, and thus is not thought to be solely the result of the contrast between the grave-fill and surrounding soil alone. Assuming a subsurface velocity of 0.1 m/ns the depth of this horizon is at 0.625 m. The source of this feature running across the majority of the GPR data is potentially from when the land was made, marking the point from which the region was drained and filled with sediment from nearby lakes consisting of sand and peaty soil. It's possible that this horizon might also be due in part to the water-table, which was identified at 0.7 m in previous soil investigations at the site (Buijs and Skinner, 2021); however the discontinuity of the horizon in some radargrams (e.g. Figure 4.6i) limits the validity of this interpretation. This phenomenon has been observed in other works, wherein a break in soil horizon, or disturbed grave-fill generates prominent horizontal reflections in radargrams (Johnston, 2021; Molina et al., 2016) highlighting the position of simulated clandestine burials. In order to substantiate the source of this horizon, future works should perform extensive soil analysis to identify the presence of these horizons at the site. Regardless of it's source, this reflection horizon allows for the position of burials to be elucidated both from it's continuity along lines which do not intersect the burials, and it's discontinuity along lines which do intersect one or more of the burials.

Looking at the influence of rainfall events on the data, it is clearly evident in both the radargrams and timeslices that the presence of moisture in the subsurface, even days after rainfall (Day 2), increases the detectability of simulated clandestine burials with GPR in this environment. The presence of moisture in the soil accentuates the contrast between the two materials, resulting in the highlighting of burials under wet conditions. Velocity analysis of the hyperbolas in dry data, Day 1 Line x7 and wet data, Day 2 Line x7 were performed in order to substantiate claims that there is an increase in soil water content as a result of precipitation events resulting in a decrease in radar velocity in the subsurface. In Figure 5.1 the analysis is shown, demonstrating the decrease in radar velocity in the grave-fill with increased water content.

In the wet data, Line y11 between burials in Figure 4.6f, the linear horizon has an increased contrast with the background and appears more continuous, allowing for the ability to distinguish lines which do not intersect burials, and lines which do, much more easily. For Line x10, Figure 4.6c, the shifts in direct-wave arrival times are more pronounced in Day 2 data when compared to Day 1 data in Figure 4.6b, suggesting an increase in radar velocity contrast between the grave-fill and surrounding soil following rainfall events. This contrast allows for undeniable identification of the presence of each burial in Line x10, and others running perpendicular and intersecting all burials.

(a) Day 1, velocity = 0.124 m/ns

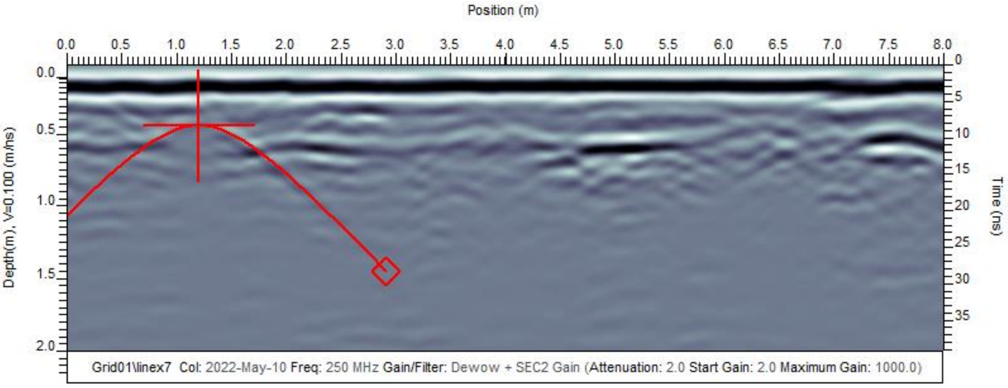

(b) Day 2, velocity 0.112 m/ns.

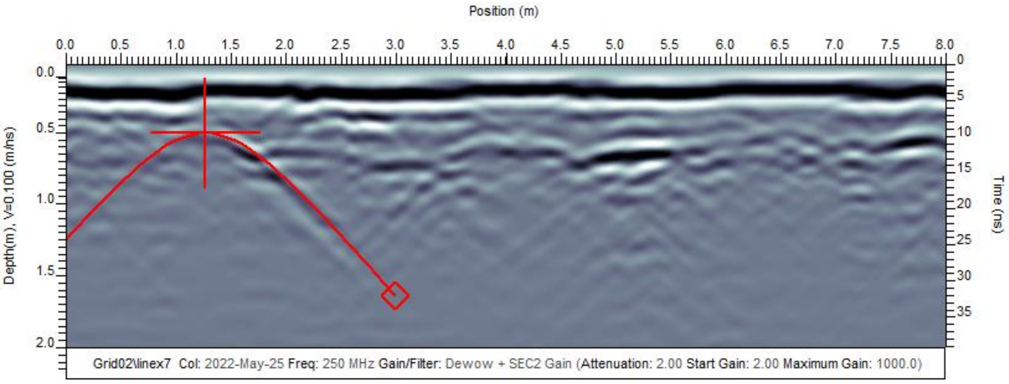

Figure 5.1: Velocity analysis performed on Line x7 with 250 MHz antenna on Day 1 (dry) and Day 2 (wet) in Ekko_project6.

The clear jumps in two-way travel time of the first arrivals in Figure 4.6c and to a lesser extent in Figure 4.6b are due to the difference in radar wave velocity in the grave-fill versus the surrounding material. In the dry data the contrasting properties of the soil are primarily related to the differences in compaction, and thus contrasting pore space and air content in the two soils. In the wet data a larger contrast exists due to the addition of soil moisture content. Air has very low permittivity and water very high, thus a strong contrast exists between soils which have variable soil water content, resulting in high reflectivity at these boundaries, as was derived in Section 2. Additionally, the grave-fill and the surrounding soil are different textures. The grave-fill, being loose sand, which is distinctively less densely packed then the surrounding sandy-loam soil with vegetation. It is already known that the two materials have contrasting air content, from visual inspection as well as we can detect their variations with GPR (Figure 4.6b). So, the different soils also must have variations in soil water holding capacity. The addition of water to the soil through rainfall will thus result in an increase in reflectivity between the grave-fill and the surroundings, because differences in water holding capacity provide a larger contrast than the difference related to solely air filled pore space volume. Infiltration rate is also higher for coarse materials like the loose sand, so the water could potentially drain out more quickly from this material, while it remains longer in the other soil, resulting in a contrast in material properties days after rain. In addition, increased water content may increase conductivity and thus attenuation of the signal, which may explain the added ringing in Day 2 data (Figure 4.6c), though there is no significant loss of penetration. The wet data in timeslices (Figure 4.7) has an advantage in the detection of the burials over the dry data, due to the increase in contrast between the grave-fill and the surrounding soil. Some previous works observed a similar phenomena, with rainfall events acting to improve the contrast between burials and the surrounding soil (Schultz and Martin, 2012), while others found that in an environment dominated by clay-rich loam, heavy rainfall events had a masking effect on the detectability of burials with GPR (Van Schoor et al., 2017). In such an environment drainage is expected to be limited, which is substantially different to the soil environment at ARISTA wherein predominantly porous sand is present. Thus, invariably, the extent to which the addition of soil moisture aids in the detection of simulated clandestine burials depends on the environment and drainage characteristics of the soil.

How can the data be improved through processing and visualization techniques, and what is the influence of these steps on the successful detection of simulated clandestine burials?

The result of airwave removal, provided in Figure 4.8 is the generation of a zero lag spike across the radargram. This is beneficial in the sense that it is much easier to interpret the two-way travel time to the object, given that the signals time delay is removed. One frequent consequence of this process is the sharpening of the wavelet, resulting in increased resolution of subsurface reflection features; however in this result we do not see evidence of this effect. Overall, removal of the airwave has very little effect on the data quality rather simply acting as an easy method to transform the data into zero-lag traces. It is unhelpful in unmasking information near the surface which is obstructed by the direct-wave.

In Figure 4.9 the results of average background subtraction are presented for two lines, with 250 MHz data Figure 4.9c and 500 MHz data Figure 4.9d. Average background subtraction is fairly successful in removal of the direct-wave in the y28, 250 MHz data. This is likely due to the fact that for this line, the direct-wave is very constant across the profile, so the average trace is successful in capturing the signature of the direct-wave. In the 250 MHz data average background subtraction improves the visibility of the hyperbolic feature which is positioned over the burial. However, the top of the hyperbola has been clearly damaged by this process. In comparison in Line x7, 500 MHz average background subtraction has very little effect on the direct-wave, dimming its amplitude only minimally and removing it in part at the earliest arrival times. In the near surface however, no new features are revealed through average background subtraction. The shift in signal arrival times, which is likely due to the change in soil compaction over the burials centered at 1.50 m, 4.25 m and 7.00 m, is still evident in the background average subtracted data, although with lesser contrast. Given these dramatic shifts in arrival times in Figure 4.9b, the variation in the shape of the direct-wave is not captured by the average trace, resulting in a dimming of the event rather then the removal.

Adaptive subtraction on the other hand was successful in the removal of the direct-wave contribution in both Line y28, 250 MHz Figure 4.9e and Line x7, 500 MHz Figure 4.9f. In Line y28 the hyperbolic event at 2.25 m is distinguished with ease, and appears to have little to no damage due to direct-wave removal. However, as a result of the selection of window length in the x-direction which is sufficient to remove the direct-wave, the continuity between traces has suffered. This is apparent in the discontinuity between the high amplitude nearly horizontal events from 0 - 1 m and 3 - 3.5 m. In Line x7 adaptive subtraction results in the removal of the direct-wave contribution, revealing the nature of the travel-time shifts at 0.25 - 0.5 $\times 10^{-8}$ s (2.5 - 5 ns), and providing a much more detailed image of the near surface features, which are plentiful. There appears to be hyperbolic reflections occurring at the onset and end of each burial as the GPR intersects it. This is evident by the limbs of hyperbolic reflections dipping down towards each other on either side of the burial position. This is in particular clear for the burials positioned at 1.5 m and 4.25 m. In addition, faint hyperbolic features deeper in the profile at 1.25$\times 10^{-8}$ s (12.5 ns) centered on the positions of the burial are also imaged well in the data processed with adaptive subtraction. The level of detail revealed by adaptive subtraction is significant, and the nature of the features which appear may reveal information on the burials. Distinguishing events which are a result of burial characteristics, versus those which might be contributions from different reflection arrivals due to the cross-correlation procedure described above, is an important consideration for future works. The detailed analysis of these features is outside of the scope of this work, and does require future attention.

The direct-wave was estimated based on common-source gathers collected along Line x10, perpendicular and intersecting burial A and B, for both the 250 MHz and 500 MHz data, and Line y11, parallel and between the burials for the 500 MHz data only. The assumption that a direct-wave estimate collected in a particular orientation in the grid is successful when adaptively subtracted from all lines in the grid is crucial to the success, and efficiency of adaptive subtraction. In Figure 4.10 the results of adaptive subtraction using direct-wave estimates from a common-source gather (Line x10) with opposite orientation applied to Line y22, is compared against the results from a direct-wave estimate collected from a common-source gather (Line y11) with same orientation and applied to Line y22. The same was done for common-offset Line x5. The results suggest that there is no significant difference in the success of adaptive subtraction in this environment if the direct-wave estimate is collected in a line perpendicular, or parallel to the common-offset line being processed. The difference between the adaptive subtraction results produced by the two direct-wave estimates in the two different orientations was determined for Line y22 in Figure 4.10e and for Line x5 in Figure 4.10f. The difference between the resulting radargrams have absolute amplitudes <10% and <25% respectively of the max amplitudes in the radargrams; thus suggesting that the variations caused by the orientation of the common-source gather with respect to the common-offset lines is unobservable in the radargrams in Figure 4.10. Therefore the assumption of homogeneity across the grid, allowing for the use of the direct-wave estimate from a single line regardless of orientation to all lines in the grid, is valid. However, it should be noted that Figure 4.10e and 4.10f do suggest that some reflection features might be missing from one of the two adaptive subtraction results, given the seemingly non-randomness of their difference. The effect of this may be examined in further detail in the future by comparing the result of direct-wave estimates under many different soil conditions, and determining what might affect the measure of the direct-wave and to what extent this assumption of homogeneity is valid across a survey grid.

Though adaptive subtraction results in the distinction of new details and features, the raw data (e.g. Figure 4.9b) provides higher contrast features which may contribute to a clearer and more rapid detection of the locations of the simulated clandestine burials due to the striking variations in the first arrivals. Given that only a small collection of GPR lines were collected for the purpose of performing and testing adaptive subtraction with the pulseEKKO, timeslices of the processed data could not be computed. Thus, the only comparison to raw and background average subtracted data can be made with radargrams, limiting the conclusions which can be drawn about the suitability of adaptive subtraction and average background subtraction for this purpose.

6
Results: GCM

6.1. Processing techniques

The apparent conductivity measured at the receiver versus the true conductivity for the 3 intercoil spacings in both VCP and HCP configuration on Day 1 are shown in Figure 6.1a - 6.1c. The same plots for Day 2 data can be found in Appendix B Figure B.1 and B.2. Figure 6.1d is a plot of the induction number for the three intercoil spacings plotted against the true conductivity values. The induction number was computed using the array of true half-space conductivities for each of the three intercoil spacings in the HCP configuration. In all three surveys conducted at ARISTA there are similar trends which can be observed in the deviation of apparent conductivity from true conductivity and the induction number. First, for the two smallest intercoil spacings the apparent conductivity is in very high agreement with the true conductivity across all of the survey grids. However at an intercoil spacing of 1.18 m the apparent conductivity measured by the instrument begins to deviate from the true conductivity, the instrument recording values which are larger than the true values as the true conductivity increases. The HCP configuration exhibits a larger departure from the true conductivity than the VCP in all cases. The induction number plot also demonstrates very similar findings for the three surveys. The induction number increases with true conductivity and with intercoil spacing, further substantiating the previous observations that as intercoil spacing increases, the measured apparent conductivity deviates from the true conductivity, meaning that the LIN approximation begins to fail.

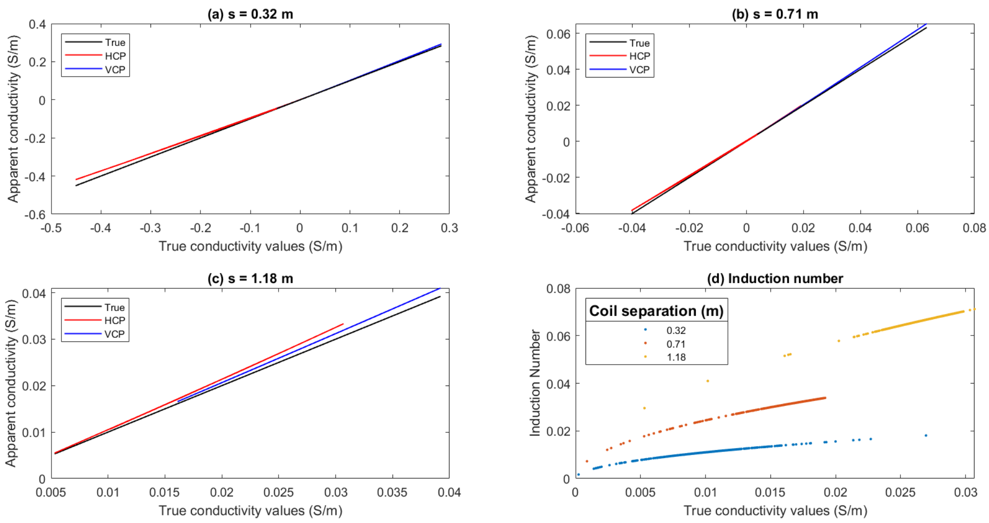

Figure 6.1: Day 1 apparent conductivities at 3 intercoil spacings (a) 0.32 m (b) 0.71 m and (c) 1.18 m above a range of true half-space conductivities. The results are shown for both HCP (red) and VCP (blue) configurations. The expected true behavior is shown in black. Plot (d) shows the induction number for the 3 intercoil spacings with increasing true conductivity.

Figure 6.2 depicts the measurement positions of the six CMD-MiniExplorer surveys which were conducted at the ARISTA test site. These plots provide the GPS coordinates and measurement locations for the data which were later used to plot the contour images presented in later figures. Figure 6.2a - 6.2b were conducted on Day 1 with 0.5 m line spacing, Figure 6.2c - 6.2d were conducted on Day 2 with 0.5 m line spacing and Figure 6.2e - 6.2f on Day 2 with 0.25 m line spacing. The approximate locations of the three burials are shown for reference. Its important to note that when looking at the contour maps in future figures, the data was only collected along these regions in the map, causing the information which is presented outside of these lines to be an extrapolation, and thus may not represent reality.

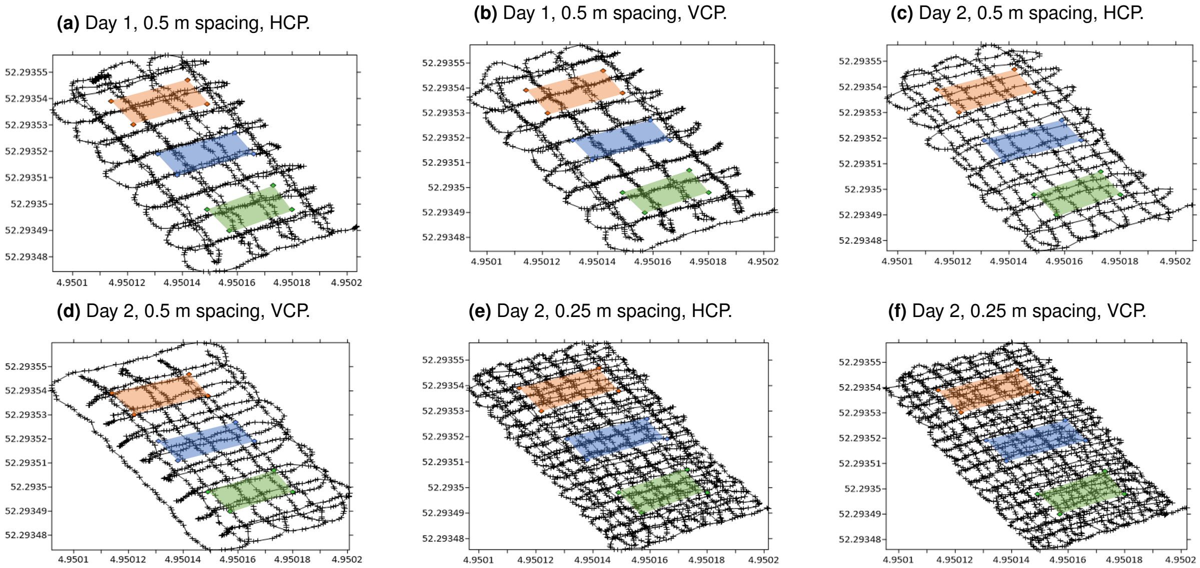

Figure 6.2: Measurement points along the survey grid for CMD surveys completed at ARISTA on Day 1 and Day 2. Approximate burial positions are indicated by shaded rectangles. Burial A in green, burial B in blue and burial C in orange. Longitude is shown on the x-axis, and Latitude on the y-axis in decimal-degrees.

The CMD-MiniExplorer data collected on survey Day 1 and 2 were corrected for LIN assumptions (at 0 m) and elevation corrected (at 0.05 m). In Appendix B, Figure B.3 the correction factors are presented at 0 m and 0.05 m elevation for all three surveys in HCP and VCP configurations from Day 1. The same is found for Day 2 data in Appendix B Figures B.4 and B.5. All datasets follow the same trends as presented in simulated data in Figure 3.11. The in-phase data showed very little departure from quadrature data on Day 1 and Day 2, and thus did not provide further information on the site conditions or aid in the identification of burials, and will not be discussed further.

Figure 6.3 provides the conductivity data from Day 1 using the HCP configuration with no correction applied, LIN correction applied and finally elevation correction at 0.05 m applied for all three intercoil spacings. The largest effect due to the correction procedures is in the s = 1.18 m data; the smaller intercoil spacings appear nearly identical with and without the required corrections. The result of the correction procedure, in particular the LIN correction, on the HCP s = 1.18 m data is an overall decrease in conductivity and increased homogeneity across the map. From the LIN correction to the elevation correction at 0.05 m there are few differences. Note the presence of very large negative values in the s = 0.32 m and s = 0.71 m maps which are not present in s = 1.18 m data. There is evidence of a strongly conducting object in the center-east of each plot which forms a dipole anomaly which is clearly distinguished from background conductivities. In addition, high conductivity regions on the north edge of the plot are present in both the s = 0.71 m and s = 1.18 m data. A high conductivity linear feature along the eastern edge of the plot is also present in both the s = 0.32 m and s = 0.71 m data. Some interesting rectangular-oblong features are also present in the s = 1.18 m corrected data which range in conductivity from 20 - 25 mS/m. These features run perpendicular to the long line of the survey grid (refer to Figure 6.2) and are consistent with the positions of burial A (green markers) and burial B (blue markers). In Figure 6.3 measurements with greater depth penetration, ie. larger s, record fewer negative conductivity values, fewer spurious events and more consistency across the survey area. The equivalent VCP data obtained on Day 1 is presented in Figure B.6, the trends presented in the results of LIN and elevation correction in Figure 6.3 are consistent with Figure B.6, however the data itself contains no valuable information due to extensive noise.

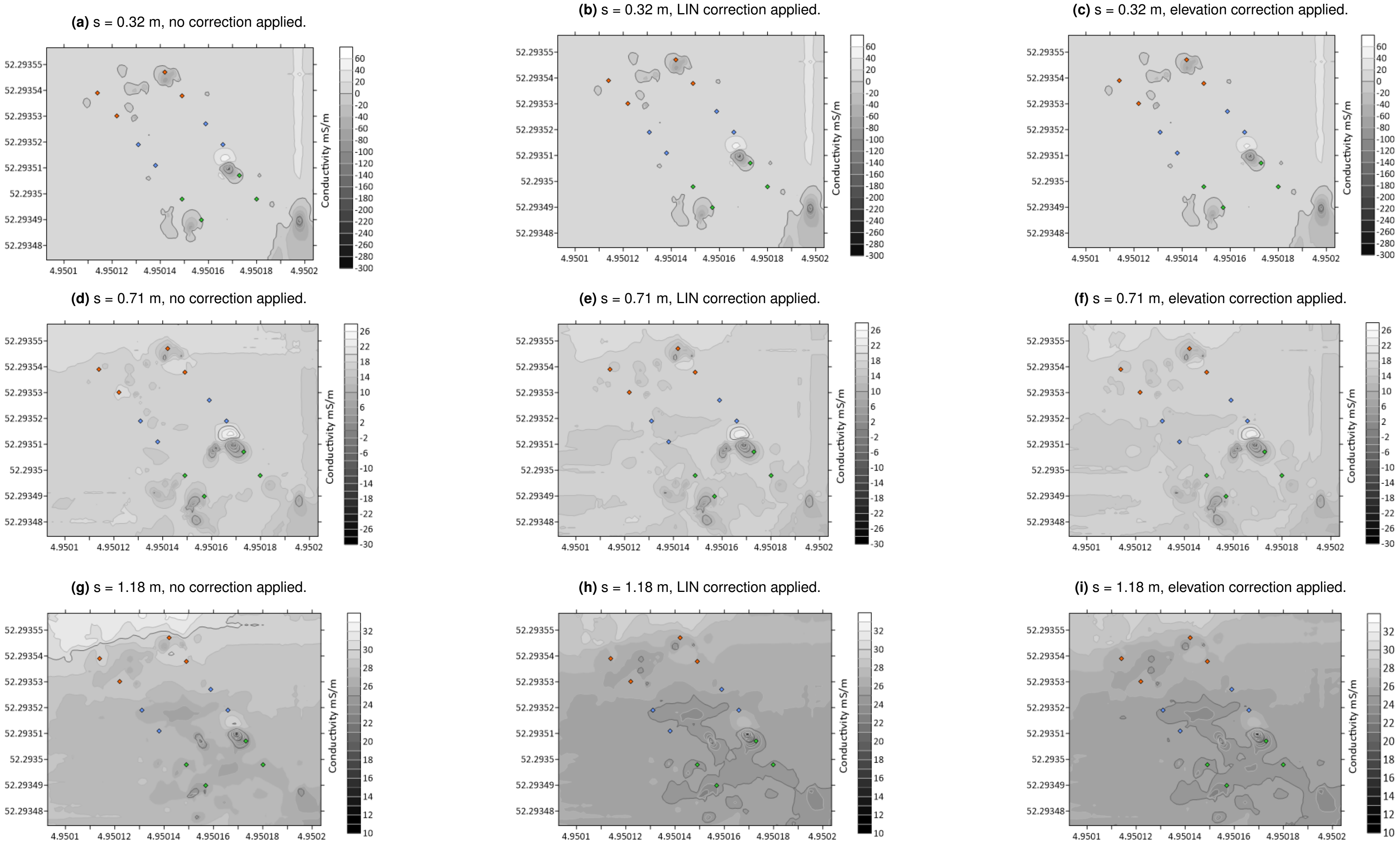

Figure 6.3: Demonstrating the effect of LIN and elevation correction on HCP data acquired on Day 1 at intercoil spacings. Raw data with no correction applied in the left column, LIN corrected data in the middle column and elevation corrected data in the right column. The approximate positions of the burials are denoted by the green (burial A), blue (burial B) and orange (burial C) markers which mark the corners of the burials shown in Figure 6.2. Contour intervals are consistent across the corrections for one intercoil spacing, focusing on the individual effect caused by the correction procedure at a particular depth sensitivity.

6.2. Acquisition Settings

In Figure 6.4 the results of the HCP configuration survey conducted on Day 2 with 0.5 m line spacing is provided alongside the data collected on the same day with 0.25 m line spacing. The results exhibit many similarities, and only a few differences. Primarily, the finer line spacing 0.25 m reveals some smaller details which are not resolved in the 0.5 m data. In both datasets with s = 1.18 m intercoil spacing there is evidence of low conductivity rectangular or elongate objects, which appear to form coherent units running perpendicular to the long edge of the grid. In the 0.5 m data these low conductivity zones line up with burial A, between burial A and B, and with burial B. In the 0.25 m line spacing these low conductivity zones are smaller and consistent with the positions of burial A and B only. In addition to these zones, a circular low conductivities zone can be seen to the left of burial B and C in both 0.5 m and 0.25 m spacing data. A very high conductivity anomaly originating from what appears to be a single point is present to the right of burial A in both datasets. The same comparison is made for VCP configuration in Appendix B Figure B.7, in this case very little differences between the two can be observed, the finer line spacing may be resolving some finer details however no distinguishable anomalies are present.

6.3. Survey Environment

In Figure 6.5 the 0.5 m line spacing data from Day 1, under dry conditions and Day 2, under wet conditions is presented for the HCP configuration. For the most part it appears as though the signals being recorded on either day are very similar; with nearly identical conductivity values across the contour maps with same s and all maps being dominated by anomalies along the perimeter of the grid. The strongest features are located along the north and east border of the plots; the Day 2 data exhibiting some additional high conductivity anomalies on the eastern border when compared to Day 1, and both exhibiting high conductivity linear anomalies on the northern border for all s. In the 1.18 m intercoil spacing data, both wet and dry, there are coherent objects which appear. In the dry dataset these objects consist of two large rectangle shapes, consistent with the positions of burial A and B, and a fainter shape consistent with burial C. While in the wet data three coherent shapes can be identified consistent with the positions of burial A and B, and between burial A and B. In both the wet and dry data the range of conductivity values for these zones is approximately 20 - 25 mS/m. Additionally, there is a strong positive high conductivity anomaly in the far east of the Day 2 data which does not appear in the Day 1 data. The Day 1 data contains the previously mentioned dipole anomaly in the central-eastern location, but it is not precisely consistent with the position and strength of the singular object in the Day 2 data. In Appendix B Figure B.8 the 0.5 m line spacing data from Day 1, under dry conditions and Day 2, under wet conditions is presented for the VCP configuration. Here very little can be observed due to large amplitude single anomalies in both datasets.

(a) s = 0.32 m, corrected conductivity, 0.5 m spacing.

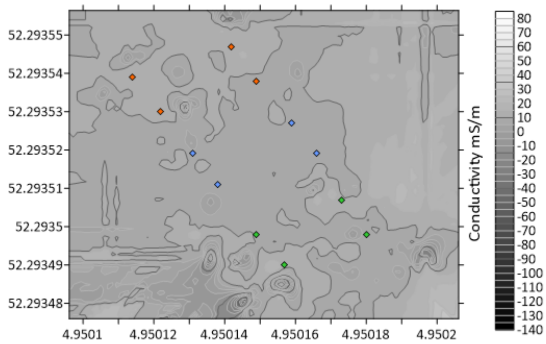

(b) s = 0.32 m, corrected conductivity, 0.25 m spacing.

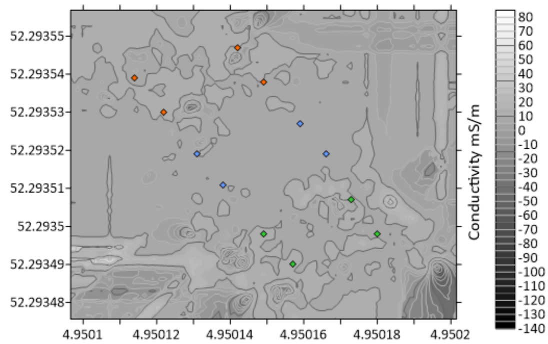

(c) s = 0.71 m, corrected conductivity, 0.5 m spacing.

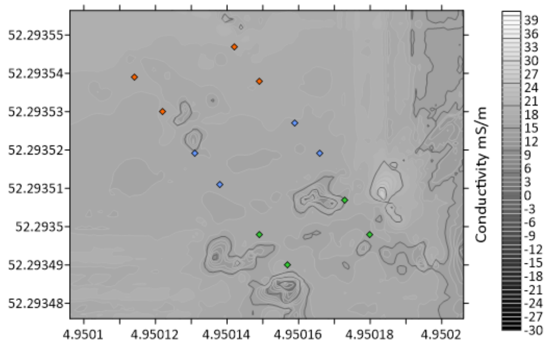

(d) s = 0.71 m, corrected conductivity, 0.25 m spacing.

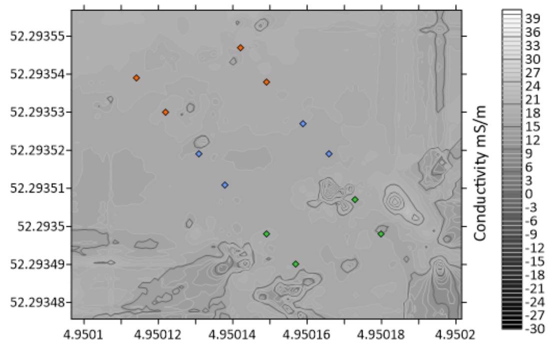

(e) s = 1.18 m, corrected conductivity, 0.5 m spacing.

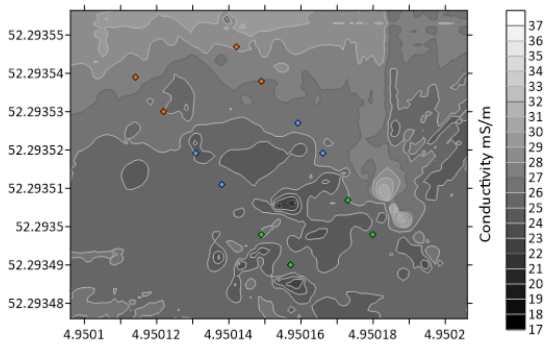

(f) s = 1.18 m, corrected conductivity, 0.25 m spacing.

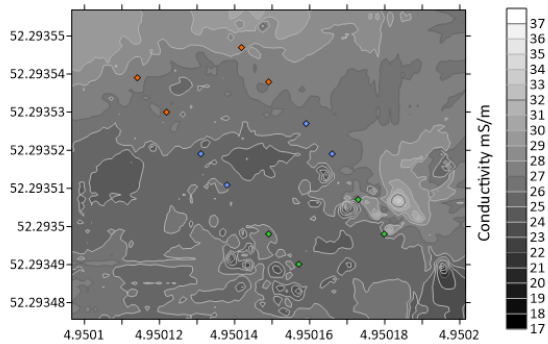

Figure 6.4: Comparison between corrected conductivity collected using 0.5 m versus 0.25 m line spacing in HCP configuration on Day 2. The approximate positions of the burials are denoted by the green (burial A), blue (burial B) and orange (burial C) markers which mark the corners of the burials shown in Figure 6.2. Contour intervals are consistent across the corrections for one intercoil spacing, focusing on the individual effect caused by line spacing at a particular depth sensitivity.

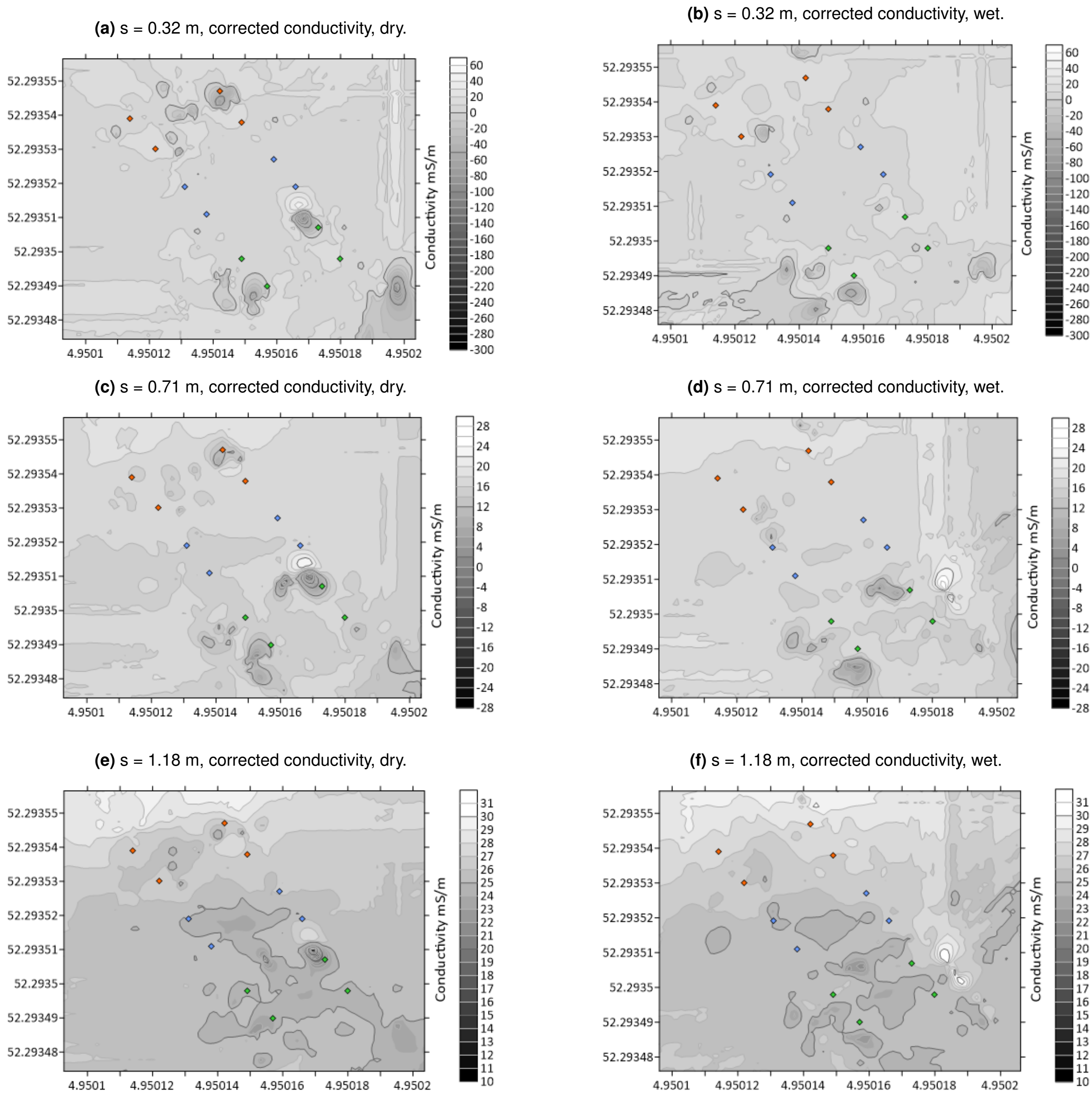

Figure 6.5: Comparison between corrected conductivity collected with 0.5 m line spacing in HCP configuration on Day 1 dry conditions (right column) and Day 2 wet conditions (left column). The approximate positions of the burials are denoted by the green (burial A), blue (burial B) and orange (burial C) markers which mark the corners of the burials shown in Figure 6.2. Contour intervals are consistent across the corrections for one intercoil spacing, focusing on the individual effect caused by soil moisture at a particular depth sensitivity.

7 Discussion: GCM

How can the data be improved through processing and visualization techniques, and what is the influence of these steps on the successful detection of simulated clandestine burials?

The application of the LIN correction and the elevation correction at 0.05 m results in subtle changes to the conductivity contour maps. However, the correction factors are significant, exceeding 1.4 in certain cases (Figures B.3 to B.5). LIN correction affects both the configurations and the different intercoil spacings to various degrees, as was demonstrated in Figure 3.11. The HCP configuration requires greater LIN correction than VCP, and the largest intercoil spacing requires greater correction than smaller spacings, thus these contour maps also present the biggest changes in Figure 6.3. For the HCP configuration a greater deviation from the LIN assumptions is occurring, in particular for those coils which penetrate to larger depths, as illustrated by the growth of induction number in Figures 6.1 and Figure B.1 - B.2. The elevation correction however exhibits somewhat different trends, as presented for simulated data in Figure 3.11 and collected data in Figure B.3 to B.5. The VCP configuration is much more sensitive to the addition of a layer of air, with 0 S/m σ_a between the instrument and the ground surface, in particular for the shortest intercoil spacings. While the HCP response at the two larger intercoil spacings is most sensitive at depths much larger than the first 0.05 m, the contribution from the layer of air is less to the overall ground response. The magnitude of elevation correction is directly related to the instruments sensitivity with depth, thus larger corrections must be applied for settings which are receiving large contributions from the layer of air above the ground surface. For the shortest spacing this correction ranges between 1.35 and 1.48, while for the largest spacing it ranges between 1.1 and 1.35 for the highest conductivity values (see Figures B.3 to B.5). In general, the correction procedures decrease the overall conductivity and increase the homogeneity of the contour maps, as shown in Figure 6.3 for HCP and Figure B.6 for VCP. These changes are very subtle and do not influence the detectability of simulated clandestine graves in this environment.

The magnitude of the correction factors reiterate the importance of performing the measurements at a constant height above the ground, as close to the ground as possible. Increasing the above ground elevation of the coils during measurement would result in inconsistent contributions from the air layer which are difficult to account for, and thus should be avoided. The effects of the air layer are much larger for VCP than HCP configuration, which should also be considered when selecting a configuration to perform measurements. Though perhaps insignificant in the contoured data itself, LIN and elevation correction is an essential exercise for reproducibility of the results, as the values recorded following correction are the true measurements regardless of elevation above the ground, which may differ from user to user.

How can the detectability of simulated clandestine burials be influenced by acquisition and survey parameter settings?

Selection of coil configuration has a significant impact on the sensitivity of the measurements with depth, and thus on the ability of the instrument to detect regions of interest. For the CMD-MiniExplorer under the LIN assumptions, the VCP configuration has a maximum depth sensitivity of 0.9 m, while the maximum for the HCP configuration has a depth of 1.8 m. However, more importantly, under the LIN assumption the peak contribution from depth of the VCP instrument is 0 m, and for the HCP it is 0.472 m, based on Figure 2.8; the impulse response functions. The results of the VCP data, for all intercoil spacings contained no anomalies of interest; likely due to it's sensitivity to surface noise, and limited sensitivity to depths greater than 0.9 m. The HCP data also provided very limited information at s = 0.32 m and s = 0.71 m, with peak contributions at a depth of 0.128 m and 0.284 m respectively. However, low conductivity anomalies, with values ranging between 20 - 25 mS/m in positions consistent with the positions of burial A and B were detected with the largest intercoil spacing in Figure 6.3, 6.4 and 6.5. The largest intercoil spacing, s = 1.18 m, under the LIN approximation contains peak contribution at a depth of 0.472 m. The anomalies which were recorded by this configuration are immediately of interest due to their orientation perpendicular to the long line of the survey grid. The conductivity values in these regions are consistent between burials and measurement days (approximately 20 - 25 mS/m). Additionally, on Day 2 in both the 0.5 m line spacing and 0.25 m line spacing data shown in Figure 6.4, a rounded-circular anomaly with the same conductivity value as the anomalies consistent with burial positions was recorded to the left of burial B and C in the grid. The position of the rounded anomaly is consistent with observations from the surface, suggesting that the grave-fill from burial C extends out from the burial due to partial grave-wall collapse. The presence of these consistent, low-conductivity coherent anomalies across survey days suggests that in the HCP configuration at at intercoil spacing s = 1.18 m the CMD-MiniExplorer may be detecting the variation in soil texture between the grave-fill and the surrounding soil matrix.

These low conductivity anomalies may be the result of higher air content in the grave-fill soil, which results in larger electrical resistivity when compared to the surrounding compacted soil matrix. The HCP configuration with largest intercoil spacing has a peak sensitivity at 0.472 m which is consistent with the positions of the burials, which likely contain the cadaver at a depth from 0.3 m to 0.6 m within the subsurface. As was seen in GPR data, burial A and burial B are detected to a higher degree than burial C, which may be attributed to the grave-fill spreading which was evident on the surface of the site, reducing the contrasting structure of the burial. In previous works, anomalous high and low conductivity zones have been detected with GCMs due to the presence of simulated clandestine burials (Nobes, 1999; Bigman, 2012) depending on the contents of the burial and its contrast with the surrounding soil. Increased conductivities surrounding burials due to the release of high conductivity decompositional fluids have been detected in-situ (Pringle et al., 2010), however the detectability of such a response with GCMs has not been reported. Thus in this environment, under the unique decompositional setting to The Netherlands, burial anomalies recorded by GCMs would be expected to be low-conductivity features. The results from this work do suggest that the CMD-MiniExplorer may have the ability to distinguish grave-fill from surrounding materials in these types of soil environments, however in this investigation these observations are made with limited confidence due to the extensive noise at the site.

The use of a finer line spacing, 0.25 m as compared to 0.5 m, which is examined in Figure 6.4 for the HCP configuration had limited impact on the detectability of targets in this environment. In the presence of extensive noise, the resolvability of anomalies is not increased through a finer line spacing, as very similar features are exhibited for both spacings. The 0.25 m line spacing does appear to resolve low-conductivity, coherent, isolated anomalies at burial positions A and B better when compared to 0.5 m line spacing. Data collected with 0.5 m line spacing exhibits a low-conductivity anomaly of the same form between burial A and B, as within burial A and B, which might be misleading when searching for clandestine burials. However this level of observation is difficult to formulate with certainty given the level of noise at the site. Under different environmental conditions perhaps the finer grid would improve the resolution of anomalies, however the impact of changing line spacing was not successfully elucidated in this investigation.

How does the survey environment affect the detectability of simulated clandestine burials?

The influence of added soil moisture content on Day 2 due to precipitation events prior to data collection was compared to Day 1 data in Figure 6.5 for the HCP configuration. There appears to be very few differences between the two datasets in the s = 0.32 m and s = 0.71 m results, with the exception of the locations of high amplitude negative and positive noise sources. Given that these two datasets were collected on different days, the location of metallic point sources in the environment changed, due to the presence of additional scientific investigations at the site on Day 2. In the s = 1.18 m Day 1 data it does appear as though the positions of the low-conductivity coherent anomalies align better with the positions of the graves than in the Day 2 data; containing less coherent anomalies, and more isolated contours. This might suggest there is some influence from added soil moisture content impacting the detectability of high-resistivity zones, given that the presence of water should increase the conductivity of the soil. If different zones in the grave-fill or surrounding subsurface have variable soil moisture content due to some inhomogeneities, then these zones might be distinguishable by the GCM as isolated low- or high-conductivity anomalies. That being said, the overall background conductivity values recorded on Day 2 do not suggest an increase in conductivity due to added soil moisture. Given that Day 1 and Day 2 data are primarily dominated by noise from metallic objects, this comparison is very difficult to make and the influence of soil moisture on the detectability of simulated clandestine graves cannot be elucidated.

In this investigation the survey environment prevented the characterization of simulated clandestine burials with high confidence. The presence of the metal fence surrounding the site was evidently disrupting conductivity measurements in all collected data, the signature of this noise being the high magnitude anomalies along the north and eastern edges of the grids. Additionally, in Day 2 data the presence of other investigations alongside the site involving many electronics including laptops and cameras impacted the data, as indicated by the high magnitude point anomaly along the eastern side of the grid. In addition, numerous of the contour maps contain a dipole event which skews the conductivity values to very large positive and negative values, in particular at the short and mid intercoil spacing. The source of this anomaly is thought to be a single sensor which was placed in burial B, near the foot of the cadaver for measuring the conditions in the burial. Additional negative high amplitude anomalies scattered throughout the grid related to unrecognized sources prevented the characterization of anomalies at s = 0.32 m and s = 0.71 m in all three surveys. In general the presence of metal objects prevented, in the smaller separations, the detection of more subtle changes in conductivity which would be expected of burials in this environment. The conductivity contrast at the site was not sufficient to detect the positions of the burials; the grave-fill and surrounding soil didn't provide a large enough contrast in material properties to be distinguished confidently at the ARISTA test site.

8
Conclusions and Outlook

In this work the central research question, "Can ground penetrating radar (GPR) and ground conductivity meter (GCM) geophysical surveys be used to identify the location of clandestine burials, and if so what are the geophysical signatures of these features?" was investigated. Geophysical surveys were performed at the ARISTA test site over three simulated clandestine burials containing human cadavers over four survey days. The effect on the detectability of the three burials due to changes in the acquisition parameters, the survey environment and the processing techniques applied was examined for GPR and GCM. A number of conclusions and future recommendations have been drawn and presented below, which summarize the results and findings of this thesis.

The GPR response over a clandestine burial can vary depending on the environmental conditions, central antenna frequency, processing techniques applied and survey grid orientation used. Anomalies which have been identified in radargrams in this work take on many forms. For GPR lines which intersect the burials in perpendicular, burial anomalies appear as jumps in direct-wave arrival times in the shallow subsurface as well as isolated hyperbolic events centered on the burials at later times. These anomalies are thought to originate from contrasting soil properties, primarily related to compaction, between the surrounding soil and the grave-fill. Conversely, the absence of burials is characterized by the presence of a continuous, high amplitude, horizontal reflection event at two-way travel time 12.5 ns (0.625 m, assuming subsurface velocity 0.100 m/ns). This feature is attributed to the base of the man-made soil fill which was added to the site in the 1600s. Lastly, intersecting simulated clandestine burials in parallel resulted in two different responses; the discontinuity of the aforementioned horizon or the presence of a horizontal high amplitude anomaly at the same depth consistent with the position and length (2 m) of the burials. Thus, when searching for clandestine burials the most important features to search for are the disruption, or the uninterrupted presence of existing background features such as a soil horizon, or the direct-wave. GPR timeslices were successful in the detection of simulated clandestine burials with fewer variations in the characteristic burial response as compared to detection with the radargrams. In timeslices burial signatures were characterized by the clear presence or absence of high amplitude rectangular anomalies. In this work, using radargrams and timeslices in conjunction lead to the best detection capabilities with GPR.

A large disadvantage of this work was the limited availability of historical data regarding the burials themselves. There was strong evidence to suggest differences between the three burials. However, given that the nature of the burials; including the positions of the cadavers, their detailed excavation history, and the soil characteristics is not known; the source of the difference in response between burials cannot be confirmed. In future works, the nature of the burials should be highly documented in order to allow for a true characterization of the effects of burial length, post-mortum interval, and burial position in a soil environment characteristic to the Netherlands. In addition, it would be a great advantage to perform zero-measurements in advance of burials. This would allow for the investigation of the source of GPR anomalies to be better elucidated. For instance, to confirm the presence of the high amplitude horizontal anomaly at 10 - 12 ns in the absence of any burials, and compare this response to the response following burial construction. In addition, the use of an empty grave to compare alongside the responses from a burial would inform whether or not the source of the anomalies is the contrast in grave-fill alone, or also due in part to the presence of the cadaver. In this work it is suspected that the grave-fill is resulting in GPR anomalies, due to the size of the anomalies, and their linearity and rectangular shape, however this requires further investigations. The Almere test site is an ideal location to perform future works given that zero-measurement data has already been obtained for three different site locations.

In this work both the 500 MHz antenna and the 250 MHz antenna were successful in the detection of simulated clandestine burials. The 250 MHz radargrams contained less clutter and provided a clearer, higher amplitude individual reflection response to the burials and in timeslices were more consistent in imaging burial rectangular anomalies. Whenever possible these antennas are recommended for use together, however in time-limited investigations it's recommended that the more robust 250 MHz antenna be used for the detection of clandestine burials.

Survey grids intersecting the burials at oblique angles were successful in imaging individual burials to various extents at this site. These results suggest the importance of performing surveys with high coverage over areas of interest to ensure full-coverage of the burial by the survey grid when oblique intersection is likely. However, as mentioned previously, due to the unknown nature of the exact differences between burials, there may be other factors which are influencing the increased detectability of one burial over another, other than grid coverage. In future works the effect of incomplete burial coverage, at oblique angles should be examined over identical burials to remove the unknown influence.

The presence of increased soil moisture at the survey site due to precipitation events resulted in increased contrast between the grave-fill and the surrounding soil matrix, improving the detectability of simulated clandestine burials. Thus, when possible, surveys should be conducted a few days after rainfall events, or the survey area may be wet manually before surveying to highlight material contrasts between the soil matrix and the less condensed grave-fill.

Three processing techniques were examined in this work, airwave removal, average background subtraction and adaptive subtraction with electromagnetic interferometry (AS/EI). Of the three techniques AS/EI was the most successful in elucidating a radar image with enhanced shallow features through direct-wave removal, allowing for the detection of the detailed burial response. In future work the nature of the more detailed reflection responses resulting from AS/EI should be investigated further to distinguish artefacts of the cross-correlation versus true burial response. The parameters for AS/EI can be adjusted further to maximize the continuity of the desired reflection events at depth, while minimizing the contribution from the direct-wave. In this work the results of adaptive subtraction using direct-wave estimates with different orientations were compared and very little difference was perceived in the success of the adaptive subtraction, however this effect should be examined in greater detail, in a variety of environments to determine the success of assuming direct-wave homogeneity. Lastly, performing AS/EI on an entire grid survey would allow for the generation of timeslices, which might provide additional information and improve detectability of simulated clandestine burials with GPR. Removal of the direct-wave through AS/EI revealed finer details in the GPR response, however the contrast between the burial positions and the background response was reduced. Thus for forensic investigations wherein determining the position of the burials is the sole goal, removal of the direct-wave through either average background subtraction or AS/EI is not recommended.

GCM surveys were unsuccessful in the detection of simulated clandestine burials with high confidence at ARISTA in this work due to the presence of significant noise sources: the surrounding metal fence, a suspected measurement sensor and scientific studies occurring nearby. In addition it is possible that the soil environment at the site, which was characterized as homogeneous sand, did not provide a strong enough conductivity contrast to be detected in the presence of significant noise sources. That being said some conclusions can be still be drawn. The HCP configuration was found to be the superior setting for performing CMD-MiniExplorer surveys over simulated clandestine burials in this environment. The best results were obtained using the largest intercoil spacing, with maximum sensitivity at 0.472 m, which corresponds to the expected depth of the burials at this site, and is least impacted by surface noise.

In this work corrections associated with the LIN approximation and elevation of the instrument 5 cm above the ground were significant, however, the corrected data did not reveal additional information in the presence of noise sources. Thus, the effect of these corrections on the detectability of burials cannot be defined with confidence in this setting. Future work using the CMD-MiniExplorer for the detection of clandestine burials would largely benefit from zero measurements, as was collected at the Almere test site, which would allow for the finer examination of variations in apparent conductivity due to the addition of burials, and cadavers therein.

References

Annan, A. (2005). Near-surface geophysics part 1: Concepts and fundamentals, 357–438. *Society of Exploration Geophysicists, New York*.

Annan, A. (2009). Electromagnetic principles of ground penetrating radar. *Ground penetrating radar: theory and applications*, *1*, 1–37.

Balestrini, F., Draganov, D., Malehmir, A., Marsden, P., & Ghose, R. (2020). Improved target illumination at ludvika mines of sweden through seismic-interferometric surface-wave suppression. *Geophysical prospecting*, *68*(1), 200–213.

Beamish, D. (2011). Low induction number, ground conductivity meters: A correction procedure in the absence of magnetic effects. *Journal of Applied Geophysics*, *75*(2), 244–253.

Bigman, D. P. (2012). The use of electromagnetic induction in locating graves and mapping cemeteries: An example from native north america. *Archaeological Prospection*, *19*(1), 31–39.

Bonsall, J., Fry, R., Gaffney, C., Armit, I., Beck, A., & Gaffney, V. (2013). Assessment of the cmd mini-explorer, a new low-frequency multi-coil electromagnetic device, for archaeological investigations. *Archaeological Prospection*, *20*(3), 219–231.

Booth, A. D., & Pringle, J. K. (2016). Semblance analysis to assess gpr data from a five-year forensic study of simulated clandestine graves. *Journal of Applied Geophysics*, *125*, 37–44.

Buijs, L., & Skinner, R. (2021). *Baseline Analysis of the Soil at Forensic Cemetery ARISTA in Amsterdam* (tech. rep.). University of Amsterdam.

Carter, D. O., Yellowlees, D., & Tibbett, M. (2010). Moisture can be the dominant environmental parameter governing cadaver decomposition in soil. *Forensic science international*, *200*(1-3), 60–66.

Connor, M., Baigent, C., & Hansen, E. S. (2018). Testing the use of pigs as human proxies in decomposition studies. *Journal of forensic sciences*, *63*(5), 1350–1355.

Dick, H. C., Pringle, J. K., Sloane, B., Carver, J., Wisniewski, K. D., Haffenden, A., Porter, S., Roberts, D., & Cassidy, N. J. (2015). Detection and characterisation of black death burials by multi-proxy geophysical methods. *Journal of Archaeological Science*, *59*, 132–141.

Ellwood, B. B., Owsley, D. W., Ellwood, S. H., & Mercado-Allinger, P. A. (1994). Search for the grave of the hanged texas gunfighter, william preston longley. *Historical Archaeology*, *28*(3), 94–112.

Fomel, S. (2007). Shaping regularization in geophysical-estimation problems. *Geophysics*, *72*(2), R29–R36.

Fomel, S. (2009). Adaptive multiple subtraction using regularized nonstationary regression. *Geophysics*, *74*(1), V25–V33.

France, D. L., Griffin, T. J., Swanburg, J. G., Lindemann, J. W., Davenport, G. C., Trammell, V., Armbrust, C. T., Kondratieff, B., Nelson, A., Castellano, K., et al. (1992). A multidisciplinary approach to the detection of clandestine graves. *Journal of Forensic Science*, *37*(6), 1445–1458.

Galloway, A., Birkby, W. H., Jones, A. M., Henry, T. E., & Parks, B. O. (1989). Decay rates of human remains in an arid environment. *Journal of Forensic Science*, *34*(3), 607–616.

GF Instruments. (2016). Short guide for electromagnetic conductivity mapping and tomography, 2–3.

GF Instruments. (2020). Cmd: Electromagnetic conductivity meters for multi-layer survey.

Hansen, F. (2019). *The Use of Common-Offset and Multiple-Offset GPR methods for Forensic Investigations* (Doctoral dissertation). Delft University of Technology. Delft.

Hansen, J. D., Pringle, J. K., & Goodwin, J. (2014). Gpr and bulk ground resistivity surveys in graveyards: Locating unmarked burials in contrasting soil types. *Forensic science international*, *237*, e14–e29.

Hayman, J., & Oxenham, M. (2016). *Human body decomposition* (1st ed.). Academic Press.

Hildebrand, J., Wiggins, S., Henkart, P., & Conyers, L. (2002). Comparison of seismic reflection and ground-penetrating radar imaging at the controlled archaeological test site, champaign, illinois. *Archaeological Prospection*, *9*(1), 9–21.

Jervis, J. R., Pringle, J. K., & Tuckwell, G. W. (2009). Time-lapse resistivity surveys over simulated clandestine graves. *Forensic Science International*, *192*(1-3), 7–13.

Johnston, G. (2021). Using GPR to Locate Unmarked Graves Webinar - YouTube. Retrieved December 6, 2021, from https://www.youtube.com/watch?v=rV5Z_6AUMUk

Jones, G. (2008). Geophysical mapping of historic cemeteries. *Technical Briefs in Historical Archaeology*, *3*, 25–38.

Juerges, A., Pringle, J., Jervis, J., & Masters, P. (2010). Comparisons of magnetic and electrical resistivity surveys over simulated clandestine graves in contrasting burial environments. *Near Surface Geophysics*, *8*(6), 529–539.

Kaufman, A. A., Keller, G. V. et al. (1983). Frequency and transient soundings. *Chi-Yu King Roberto Scarpa*, *207*(7).

Keller, G. V., & Frischknecht, F. C. (1966). Electrical methods in geophysical prospecting.

Knobel, Z., Ueland, M., Nizio, K. D., Patel, D., & Forbes, S. L. (2019). A comparison of human and pig decomposition rates and odour profiles in an australian environment. *Australian Journal of Forensic Sciences*, *51*(5), 557–572.

Knödel, K., Lange, G., & Voigt, H.-J. (2007). *Environmental geology: Handbook of field methods and case studies*. Springer Science & Business Media.

Liu, J., Draganov, D., & Ghose, R. (2018). Seismic interferometry facilitating the imaging of shallow shear-wave reflections hidden beneath surface waves. *Near Surface Geophysics*, *16*(3), 372–382.

McNeill, J. D. (1980). Electromagnetic terrain conductivity measurement at low induction numbers.

Megyesi, M. S., Nawrocki, S. P., & Haskell, N. H. (2005). Using accumulated degree-days to estimate the postmortem interval from decomposed human remains. *Journal of Forensic Science*, *50*(3), 1–9.

Milsom, J. (2003). *Field geophysics* (3rd ed.). John Wiley & Sons.

Molina, C. M., Pringle, J. K., Saumett, M., & Evans, G. T. (2016). Geophysical monitoring of simulated graves with resistivity, magnetic susceptibility, conductivity and gpr in colombia, south america. *Forensic science international*, *261*, 106–115.

Molina, C. M., Wisniewski, K. D., Drake, J., Baena, A., Guatame, A., & Pringle, J. K. (2020). Testing application of geographical information systems, forensic geomorphology and electrical resistivity tomography to investigate clandestine grave sites in colombia, south america. *Journal of Forensic Sciences*, *65*(1), 266–273.

Nienaber, W. C., Forbes, S. L., Connor, M., Wescott, D. J., Steadman, D. W., Colman, K. L., & Houck, M. (2022). Forensic taphonomy. *Encyclopedia of forensic sciences* (3rd ed., pp. 1–3416). Elsevier.

Nobes, D. C. (1999). Geophysical surveys of burial sites: A case study of the oaro urupa. *Geophysics*, *64*(2), 357–367.

Oostra, R.-J., Gelderman, T., Groen, W. M., Uiterdijk, H. G., Cammeraat, E. L., Krap, T., Wilk, L. S., Lüschen, M., Morriën, W. E., Wobben, F., et al. (2020). Amsterdam research initiative for subsurface taphonomy and anthropology (arista)-a taphonomic research facility in the netherlands for the study of human remains. *Forensic science international*, *317*, 110483.

Payne, J. A. (1965). A summer carrion study of the baby pig sus scrofa linnaeus. *Ecology*, *46*(5), 592–602.

Pringle, J. K., Cassella, J. P., & Jervis, J. R. (2010). Preliminary soilwater conductivity analysis to date clandestine burials of homicide victims. *Forensic Science International*, *198*(1-3), 126–133.

Pringle, J. K., Giubertoni, M., Cassidy, N. J., Wisniewski, K. D., Hansen, J. D., Linford, N. T., & Daniels, R. M. (2015). The use of magnetic susceptibility as a forensic search tool. *Forensic Science International*, *246*, 31–42.

Pringle, J. K., Jervis, J., Cassella, J. P., & Cassidy, N. J. (2008). Time-lapse geophysical investigations over a simulated urban clandestine grave. *Journal of Forensic Sciences*, *53*(6), 1405–1416.

Pringle, J. K., Jervis, J. R., Hansen, J. D., Jones, G. M., Cassidy, N. J., & Cassella, J. P. (2012). Geophysical monitoring of simulated clandestine graves using electrical and ground-penetrating radar methods: 0–3 years after burial. *Journal of Forensic Sciences*, *57*(6), 1467–1486.

Pringle, J. K., Jervis, J. R., Roberts, D., Dick, H. C., Wisniewski, K. D., Cassidy, N. J., & Cassella, J. P. (2016). Long-term geophysical monitoring of simulated clandestine graves using electrical and ground penetrating radar methods: 4–6 years after burial. *Journal of Forensic Sciences*, *61*(2), 309–321.

Pringle, J. K., Ruffell, A., Jervis, J. R., Donnelly, L., McKinley, J., Hansen, J., Morgan, R., Pirrie, D., & Harrison, M. (2012). The use of geoscience methods for terrestrial forensic searches. *Earth-Science Reviews*, *114*(1-2), 108–123.

Pringle, J. K., Stimpson, I. G., Wisniewski, K. D., Heaton, V., Davenward, B., Mirosch, N., Spencer, F., & Jervis, J. R. (2020). Geophysical monitoring of simulated homicide burials for forensic investigations. *Scientific reports*, *10*(1), 1–12.

Reed, H. (1958). A study of dog carcass communities in tennessee, with special reference to the insects. *American midland naturalist*, 213–245.

Reynolds, J. M. (2011). *An introduction to applied and environmental geophysics* (2nd ed.). John Wiley & Sons.

Römkens, P., & Oenema, O. (2004). *Quick scan soils in the netherlands; overview of the soil status with reference to the forthcoming eu soil strategy* (tech. rep.). Alterra.

Schotsmans, E. M., Márquez-Grant, N., & Forbes, S. L. (2017). *Taphonomy of human remains: Forensic analysis of the dead and the depositional environment*. John Wiley & Sons.

Schultz, J. J. (2007). Using ground-penetrating radar to locate clandestine graves of homicide victims: Forming forensic archaeology partnerships with law enforcement. *Homicide Studies*, *11*(1), 15–29.

Schultz, J. J., & Martin, M. M. (2011). Controlled gpr grave research: Comparison of reflection profiles between 500 and 250 mhz antennae. *Forensic science international*, *209*(1-3), 64–69.

Schultz, J. J., & Martin, M. M. (2012). Monitoring controlled graves representing common burial scenarios with ground penetrating radar. *Journal of Applied Geophysics*, *83*, 74–89.

Simmons, T., Adlam, R. E., & Moffatt, C. (2010). Debugging decomposition data—comparative taphonomic studies and the influence of insects and carcass size on decomposition rate. *Journal of forensic sciences*, *55*(1), 8–13.

Slob, E., Draganov, D., & Wapenaar, K. (2007). Interferometric electromagnetic green's functions representations using propagation invariants. *Geophysical Journal International*, *169*(1), 60–80.

Slob, E., & Wapenaar, K. (2008). Practical representations of electromagnetic interferometry for gpr applications: A tutorial. *Near Surface Geophysics*, *6*(6), 391–402.

Snieder, R. (2004). Extracting the green's function from the correlation of coda waves: A derivation based on stationary phase. *Physical review E*, *69*(4), 046610.

Snieder, R., & Sens-Schönfelder, C. (2015). Seismic interferometry and stationary phase at caustics. *Journal of Geophysical Research: Solid Earth*, *120*(6), 4333–4343.

Van Schoor, M., Nienaber, W. C., & Marais-Werner, A. (2017). A controlled monitoring study of simulated clandestine graves using 3d ground penetrating radar. *Near Surface Geophysics*, *15*(3), 274–284.

Vass, A. A., Barshick, S.-A., Sega, G., Caton, J., Skeen, J. T., Love, J. C., & Synstelien, J. A. (2002). Decomposition chemistry of human remains: A new methodology for determining the postmortem interval. *Journal of Forensic Science*, *47*(3), 542–553.

Yilmaz, Ö. (2001). *Seismic data analysis: Processing, inversion, and interpretation of seismic data* (S. Doherty, Ed.). SEG Books.

A
Ground Penetrating Radar Data

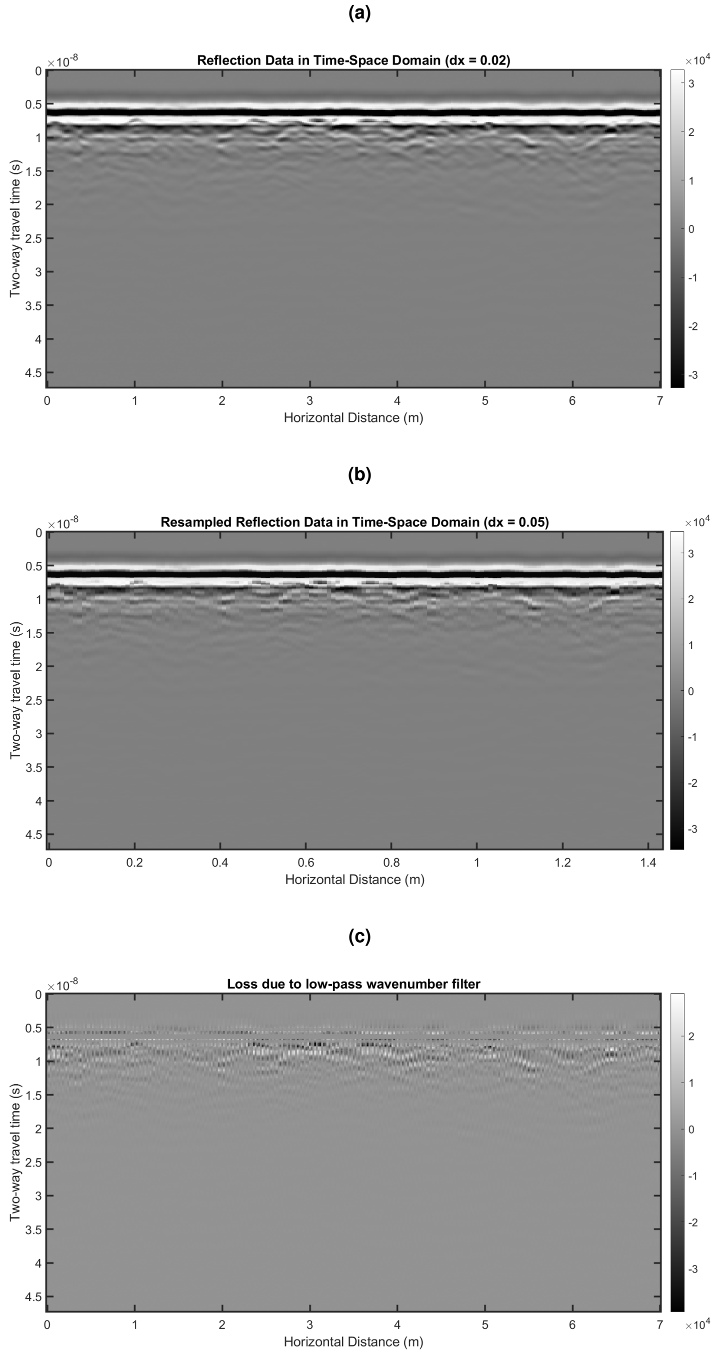

Figure A.1: Results of re-sampling in dx with data collected at the Almere site for zero-measurement data. (a) Reflection data plotted in the xt-domain along a 7 m line with sample spacing dx = 0.02 m. (b) Resampled reflection data plotted in the xt-domain with sample spacing dx = 0.05 m. (c) Amplitude of losses from low-pass wavenumber filtering of (a) to produce (b).

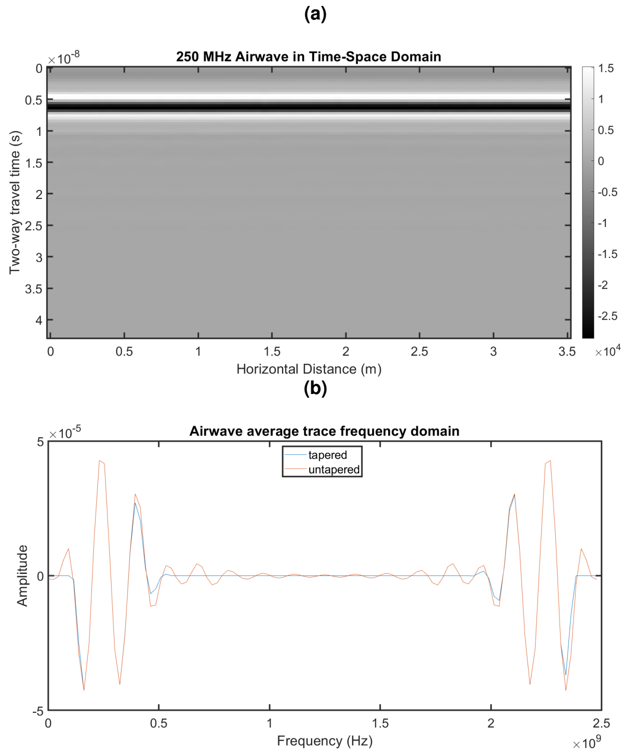

Figure A.2: Airwave removal and processing. (a) 250 MHz airwave measured using the NOGGIN. (b) Average airwave trace with no taper (orange) and with taper (blue), the taper is applied to filter out ringing in the data and isolate the airwavelet.

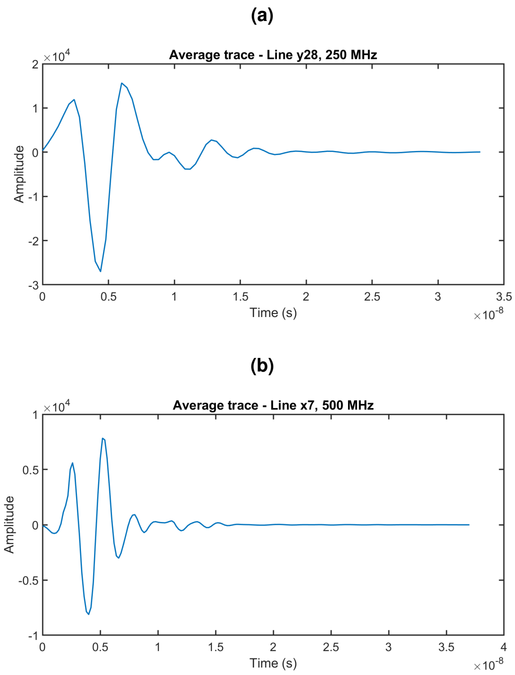

Figure A.3: Average trace computed across (a) Line y28, 250 MHz and (b) Line x7, 500 MHz and used for average background subtraction.

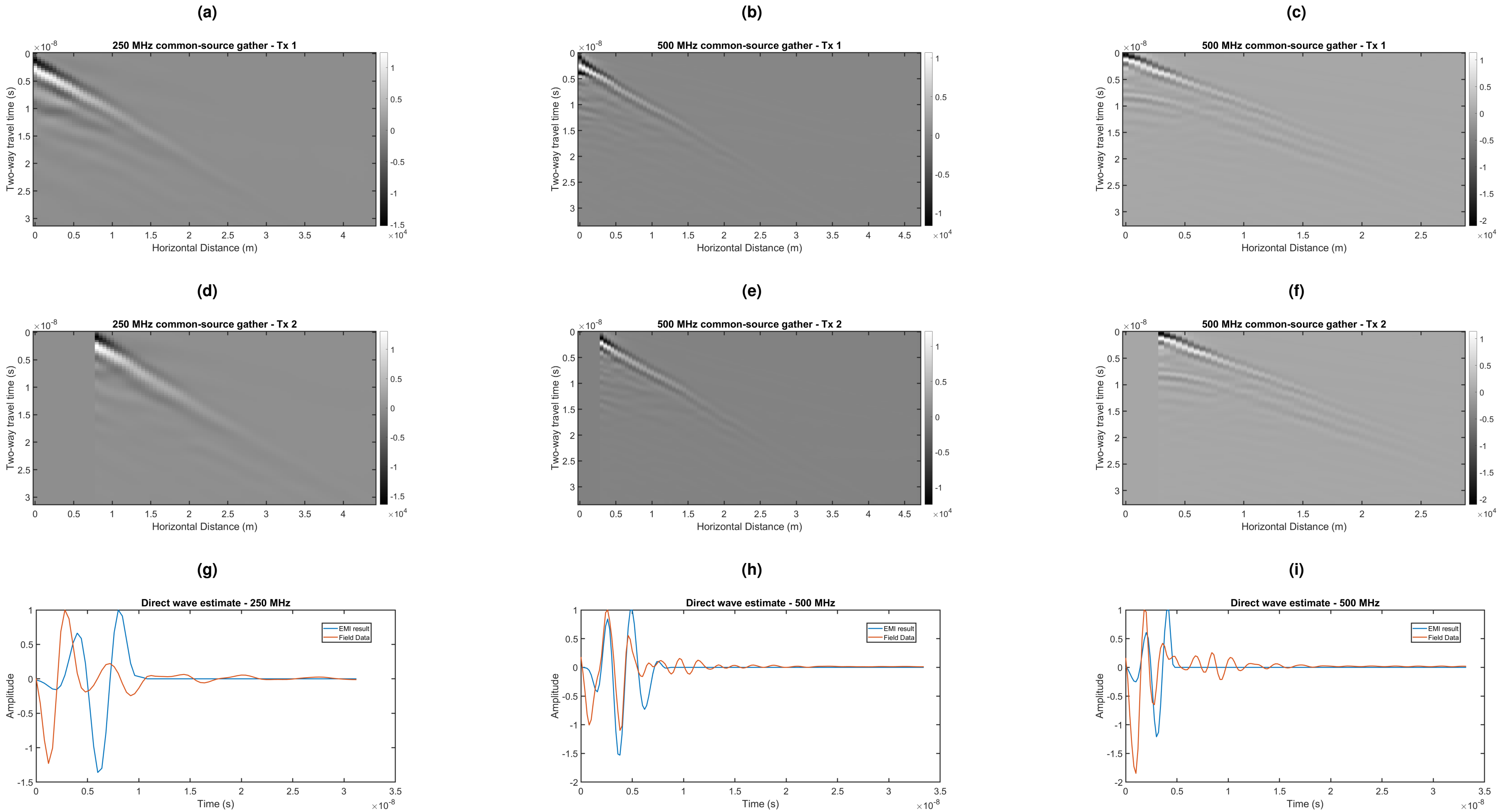

Figure A.4: (a-f) Common-source gathers collected with 250 MHz along Line x10 (left column), 500 MHz along Line x10 (middle column) and 500 MHz along Line y11 (right column) at two different source positions. (g-i) are the direct-wave estimates as a result of EI processing on the above common-source gathers for the 250 MHz x10, 500 MHz x10, and 500 MHz y11, respectively. The field data is the first trace in the common-source gather.

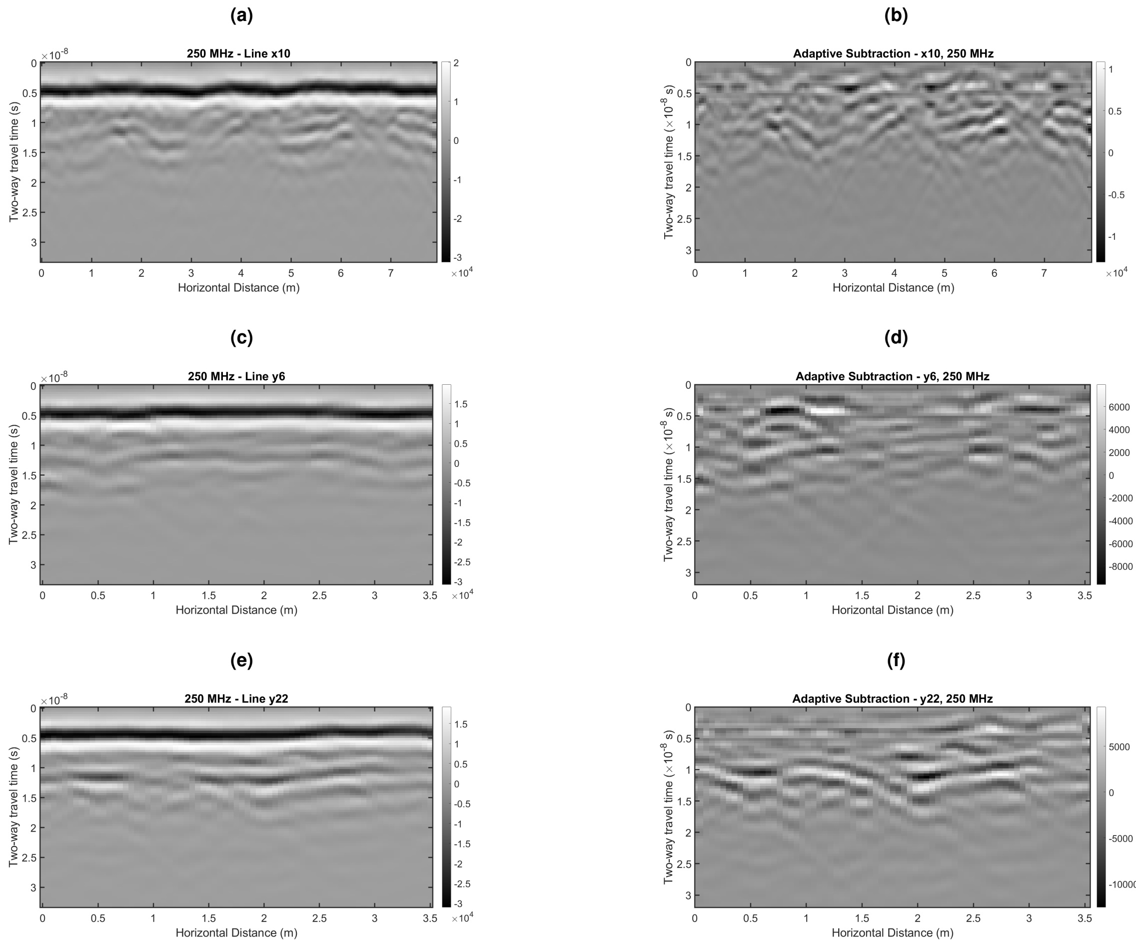

Figure A.5: Comparing raw radargrams (left column) against data with adaptive subtraction applied (right column), acquired with 250 MHz pulseEKKO antenna on Day 3.

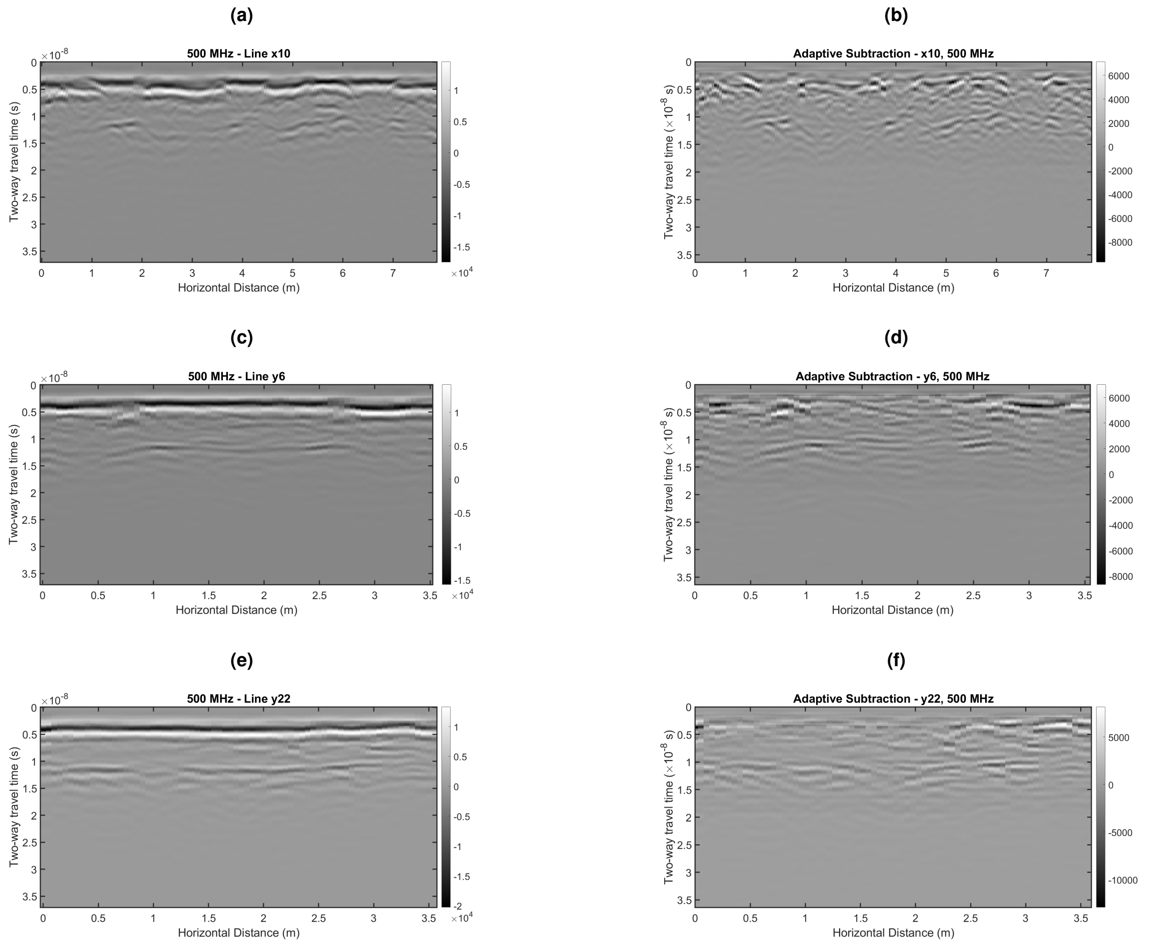

Figure A.6: Comparing raw radargrams (left column) against data with adaptive subtraction applied (right column), acquired with 500 MHz pulseEKKO antenna on Day 3.

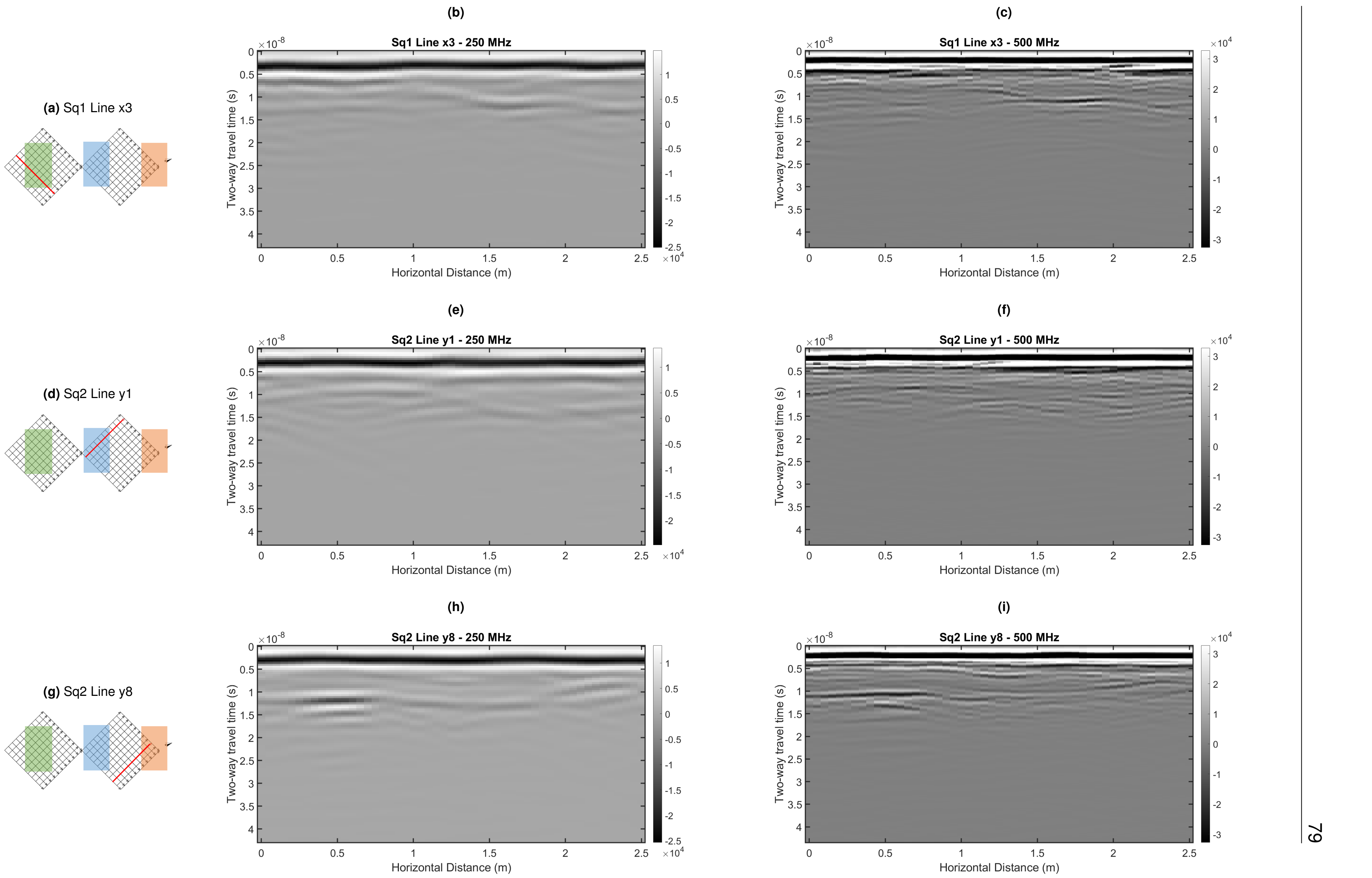

Figure A.7: Angled grid GPR lines with 250 MHz antenna (middle column) and 500 MHz antenna (right column) NOGGIN GPR. (a-c) Sq1 Line x intersecting burial A, (d-f) Sq2 Line y1 intersecting burial B, (g-i) Sq2 Line y8 intersecting burial C.

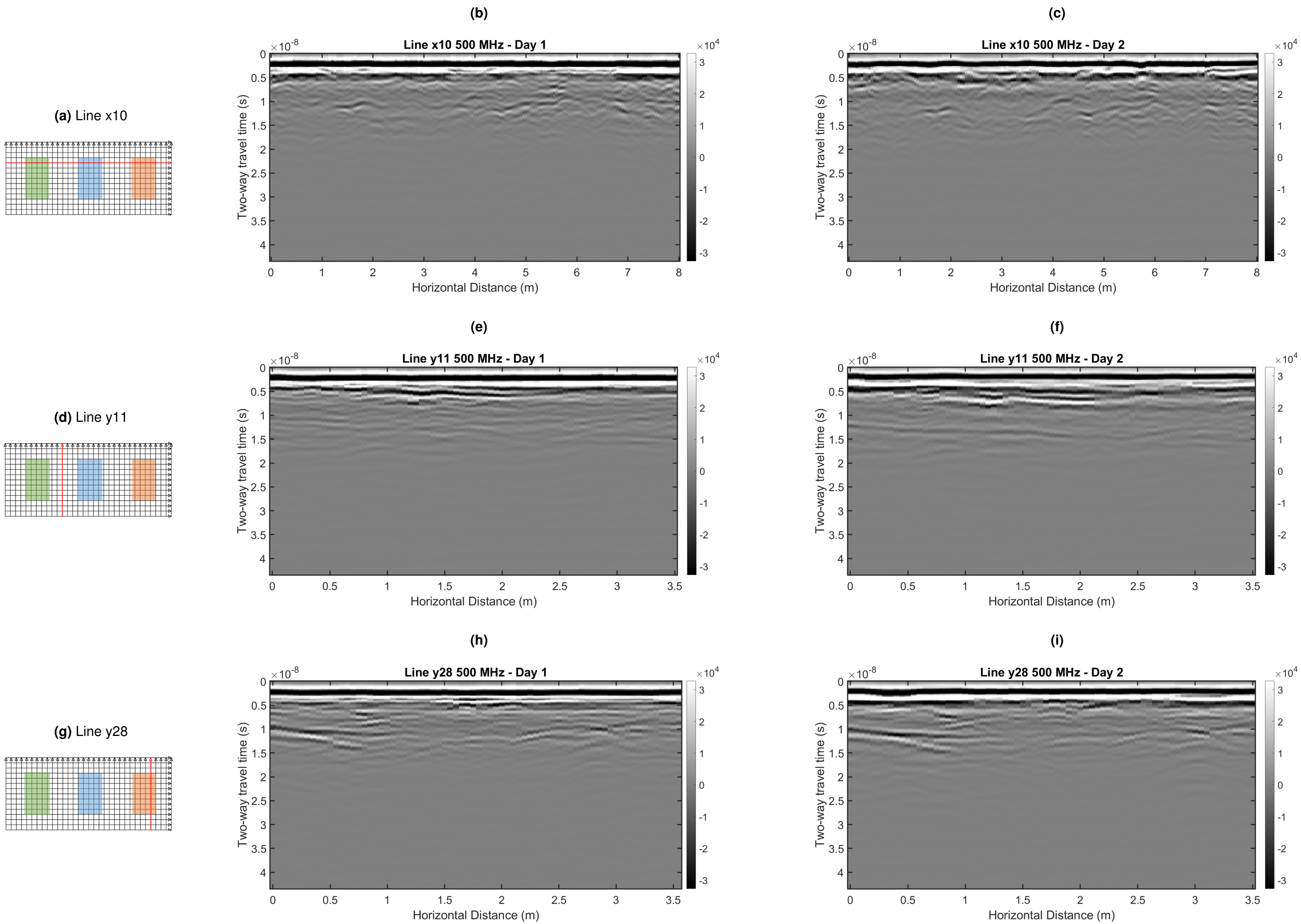

Figure A.8: Comparing GPR lines acquired on Day 1 in dry conditions (middle column) versus Day 2 in wet conditions (right column) with the NOGGIN 500 MHz antennas. (a-c) Line x10 perpendicular and intersecting all burials, (d-f) Line y11 parallel and between burials, (g-i) Line y28 parallel and intersecting burial C.

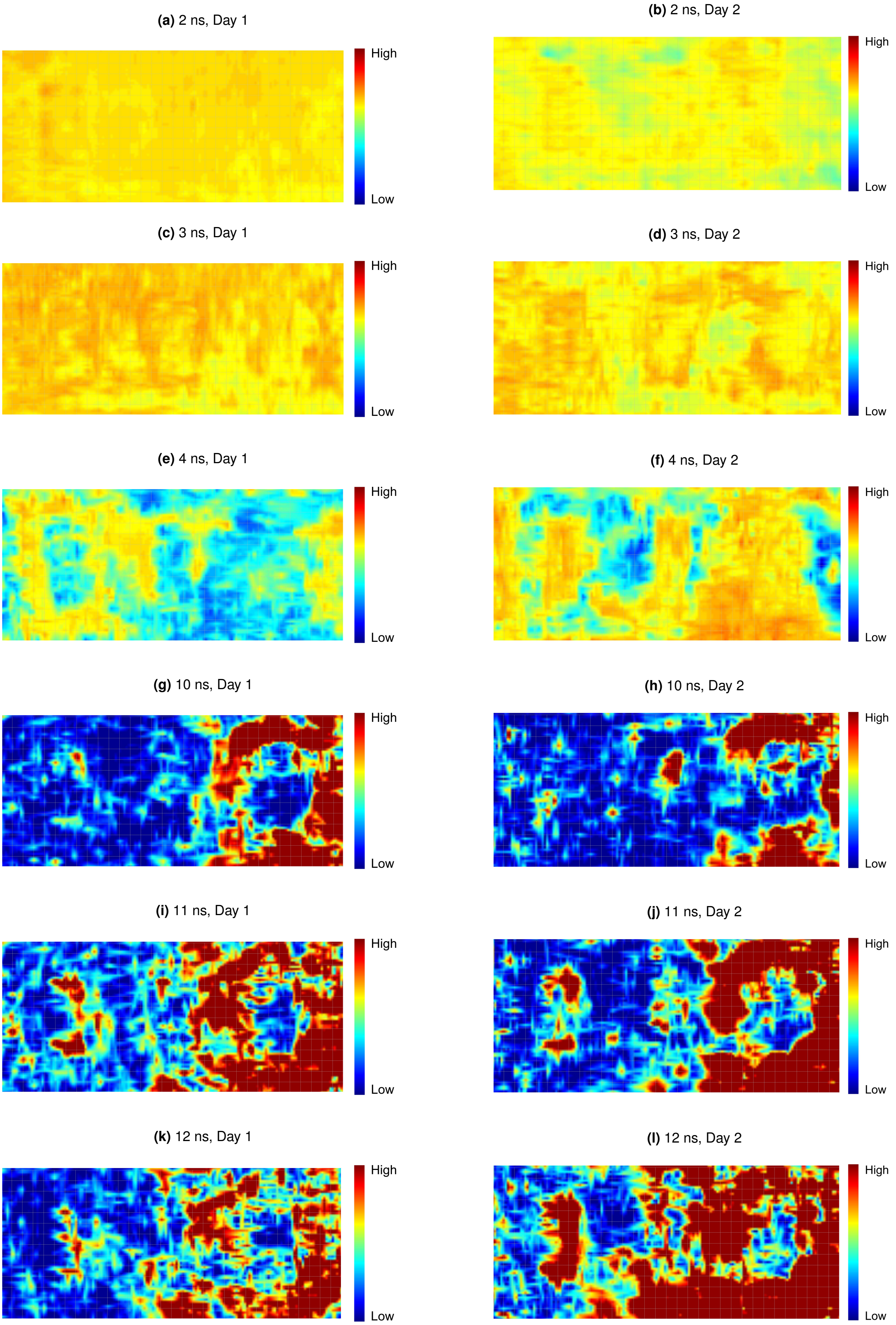

Figure A.9: Comparing timeslices from Day 1 in dry conditions (left column) and Day 2 in wet conditions (right column) acquired with Noggin 500 MHz. Timeslices are generated in EKKO_project and processed with envelope to distinguish high versus low amplitude anomalies.

B
Ground Conductivity Meter Data

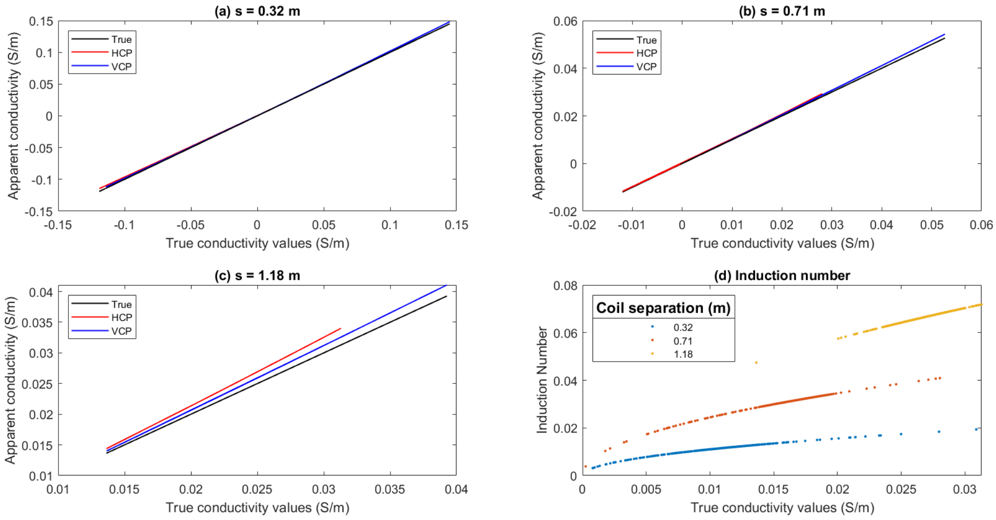

Figure B.1: Day 2 apparent conductivities acquired with 0.5 m line spacing at 3 intercoil spacings (a) 0.32 m (b) 0.71 m and (c) 1.18 m above a range of true half-space conductivities. The results are shown for both HCP and VCP configurations. The expected true behavior is shown in black. Plot (d) shows the induction number for the 3 intercoil spacing.

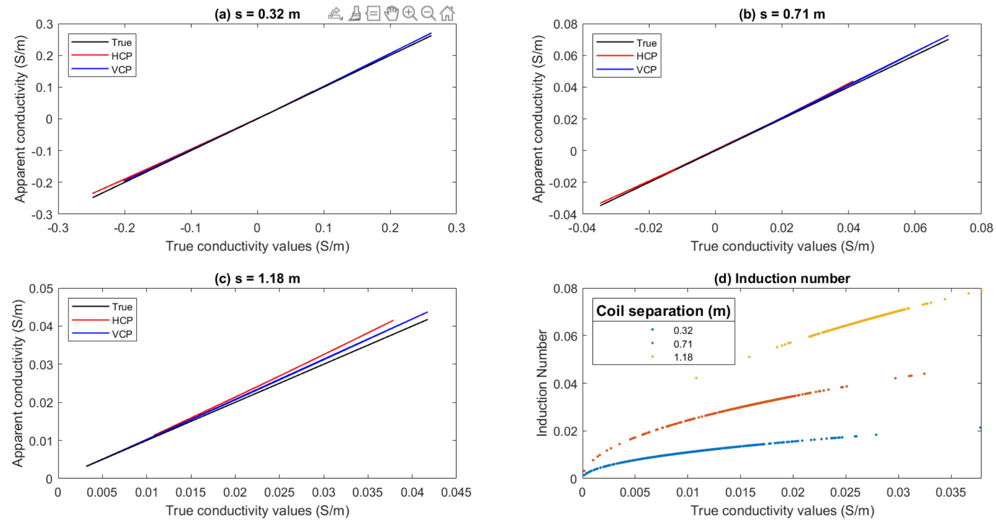

Figure B.2: Day 2 apparent conductivities acquired with 0.25 m line spacing at 3 intercoil spacings (a) 0.32 m (b) 0.71 m and (c) 1.18 m above a range of true half-space conductivities. The results are shown for both HCP and VCP configurations. The expected true behavior is shown in black. Plot (d) shows the induction number for the 3 intercoil spacings.

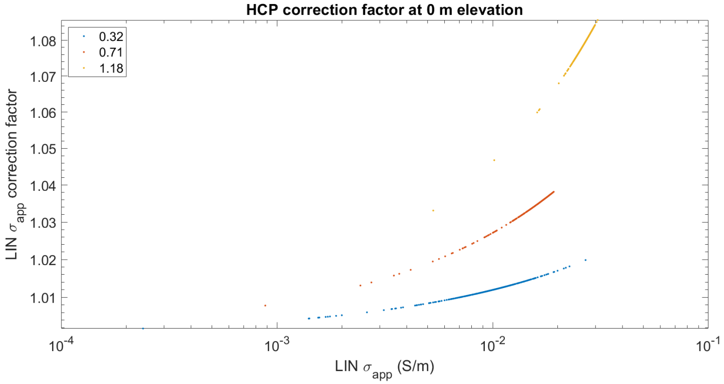

(a) Correction factor required to remove deviation from LIN approximation for 3 intercoil spacings in HCP configuration.

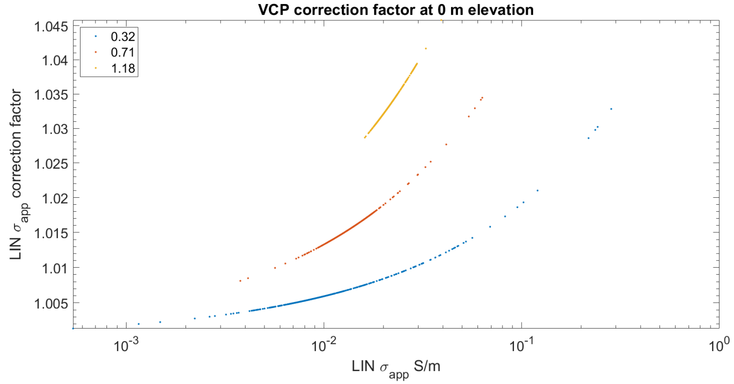

(b) Correction factor required to remove deviation from LIN approximation for 3 intercoil spacings in VCP configuration.

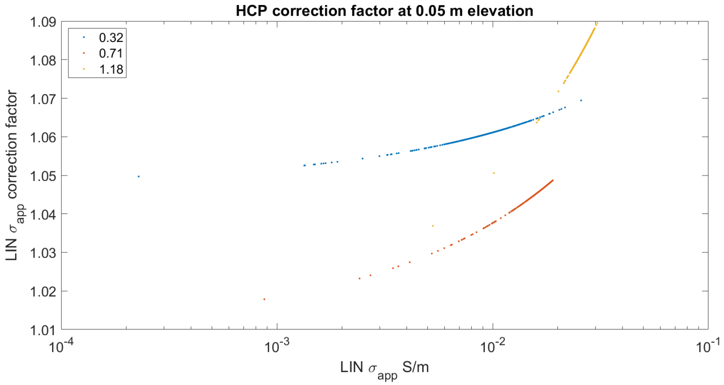

(c) Correction factor required to remove deviation from LIN approximation for 3 intercoil spacings in HCP configuration located 5 cm elevation above the ground surface.

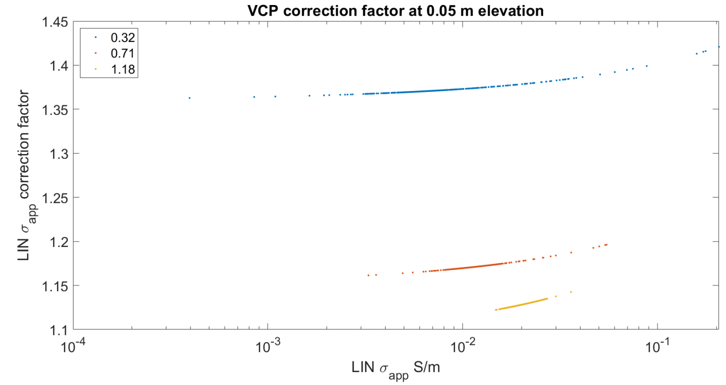

(d) Correction factor required to remove deviation from LIN approximation for 3 intercoil spacings in VCP configuration located 5 cm elevation above the ground surface.

Figure B.3: Correction factor applied to CMD Data collected at ARISTA on Day 1 with 0.5 m line spacing.

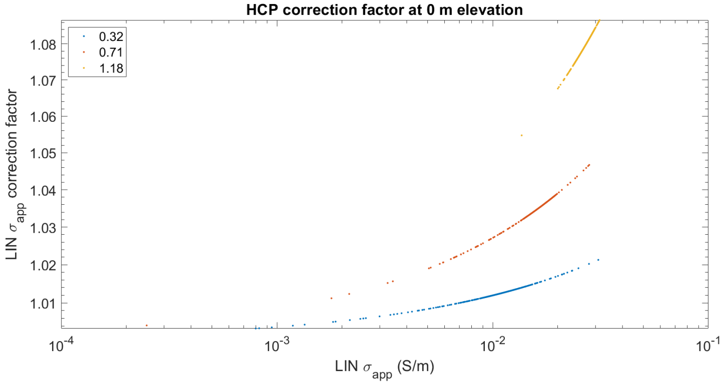

(a) Correction factor required to remove deviation from LIN approximation for 3 intercoil spacings in HCP configuration.

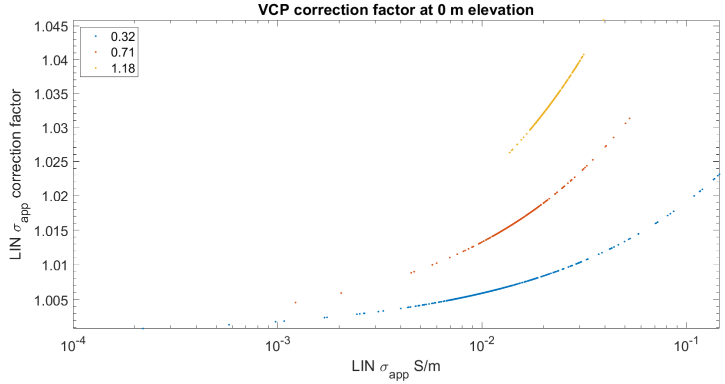

(b) Correction factor required to remove deviation from LIN approximation for 3 intercoil spacings in VCP configuration.

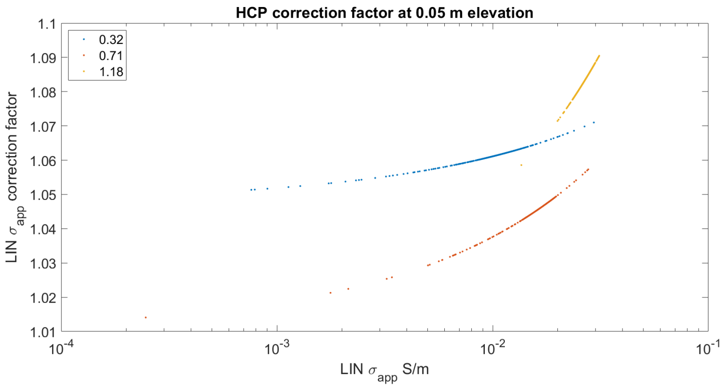

(c) Correction factor required to remove deviation from LIN approximation for 3 intercoil spacings in HCP configuration located 5 cm elevation above the ground surface.

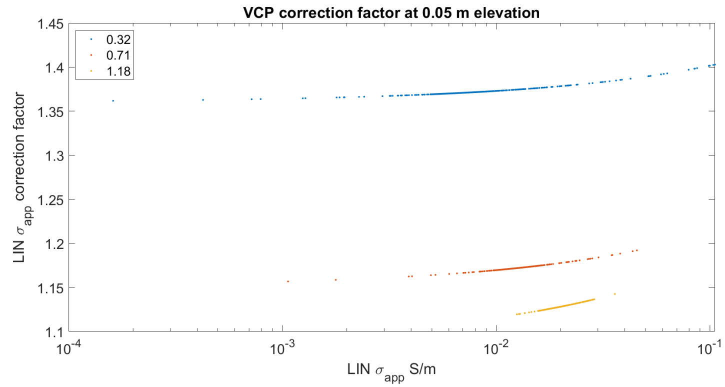

(d) Correction factor required to remove deviation from LIN approximation for 3 intercoil spacings in VCP configuration located 5 cm elevation above the ground surface.

Figure B.4: Correction factor applied to CMD Data collected at ARISTA on Day 2 with 0.5 m line spacing.

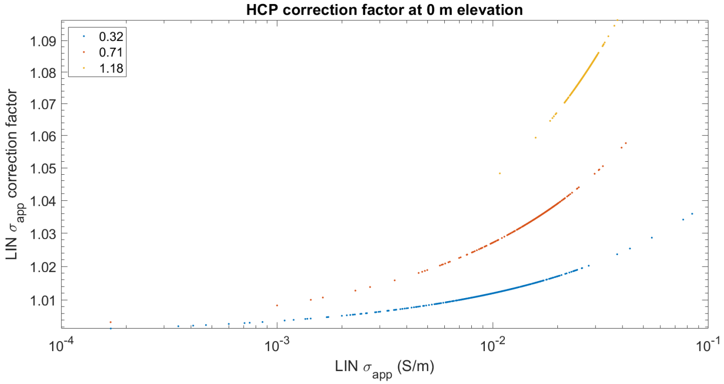

(a) Correction factor required to remove deviation from LIN approximation for 3 intercoil spacings in HCP configuration.

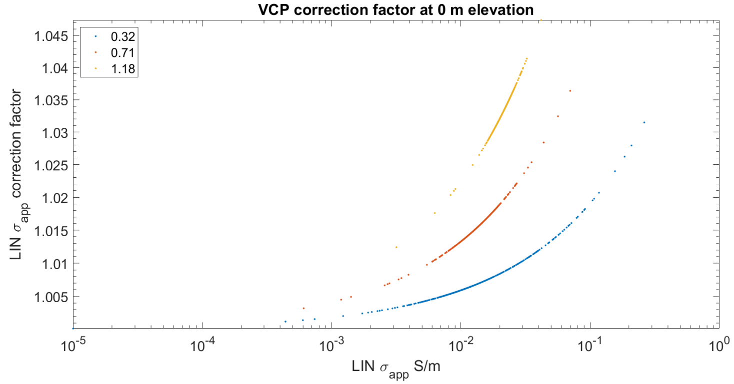

(b) Correction factor required to remove deviation from LIN approximation for 3 intercoil spacings in VCP configuration.

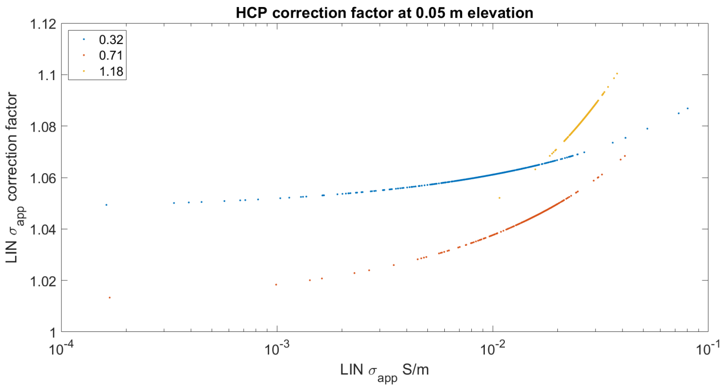

(c) Correction factor required to remove deviation from LIN approximation for 3 intercoil spacings in HCP configuration located 5 cm elevation above the ground surface.

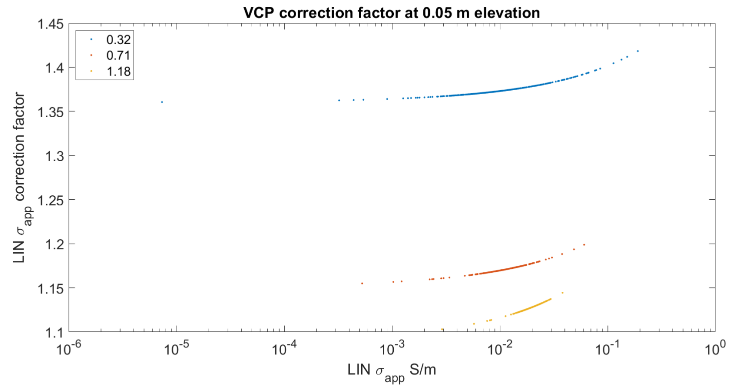

(d) Correction factor required to remove deviation from LIN approximation for 3 intercoil spacings in VCP configuration located 5 cm elevation above the ground surface.

Figure B.5: Correction factor applied to CMD Data collected at ARISTA on Day 2 with 0.25 m line spacing.

(a) s = 0.32 m, no correction applied.

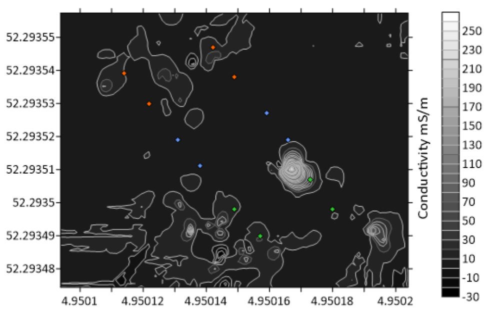

(b) s = 0.32 m, LIN correction applied.

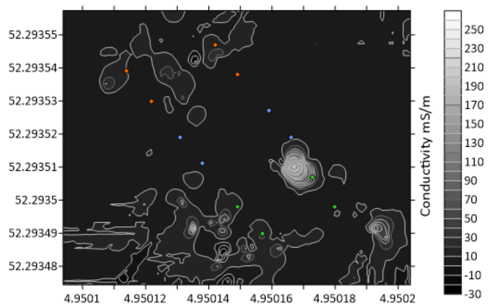

(c) s = 0.32 m, elevation correction applied.

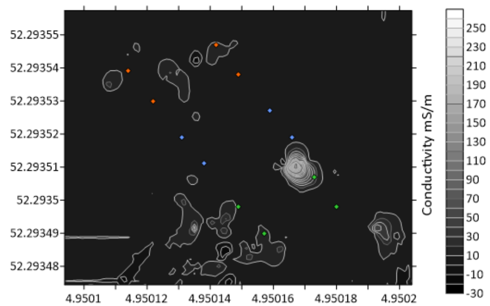

(d) s = 0.71 m, no correction applied.

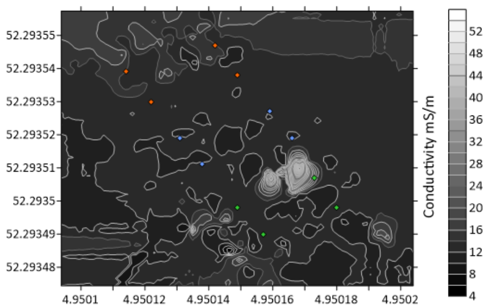

(e) s = 0.71 m, LIN correction applied.

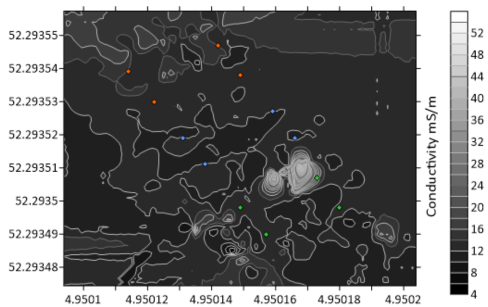

(f) s = 0.71 m, elevation correction applied.

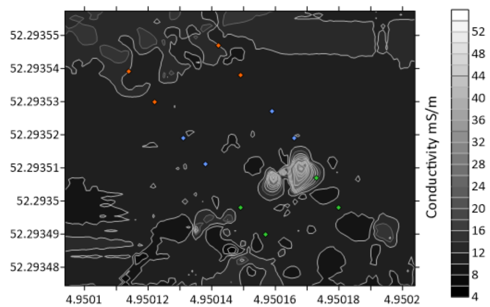

(g) s = 1.18 m, no correction applied.

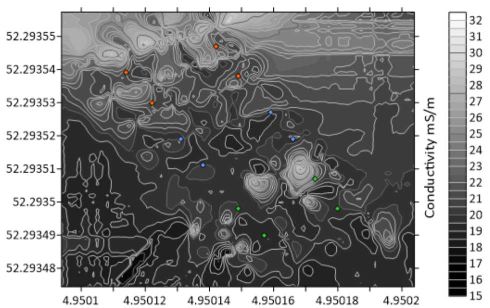

(h) s = 1.18 m, LIN correction applied.

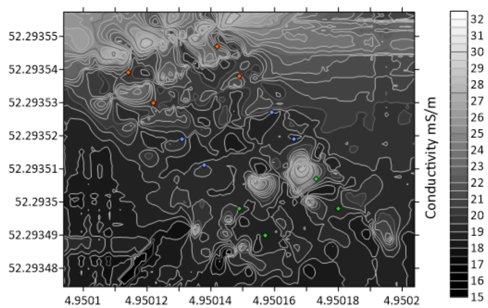

(i) s = 1.18 m, elevation correction applied.

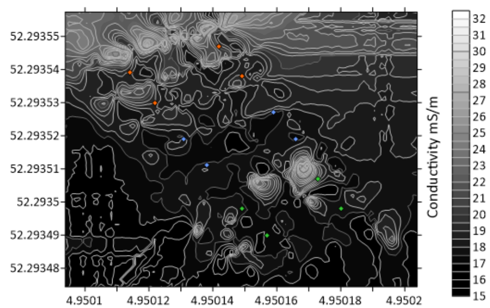

Figure B.6: Demonstrating the effect of LIN and elevation correction on VCP data acquired on Day 1 at 3 intercoil spacings. Raw data with no correction applied in the left column, LIN corrected data in the middle column and elevation corrected data in the right column. The approximate positions of the burials are denoted by the green (burial A), blue (burial B) and orange (burial C) markers which mark the corners of the burials shown in Figure 6.2. Contour intervals are consistent across the corrections for intercoil spacing, focusing on the individual effect caused by the correction procedure at a particular depth sensitivity.

(a) s = 0.32 m, corrected conductivity, 0.5 m spacing.

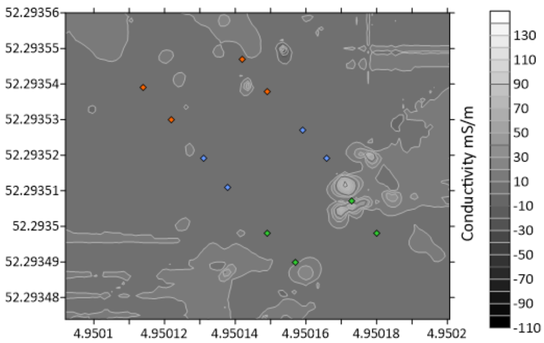

(b) s = 0.32 m, corrected conductivity, 0.25 m spacing.

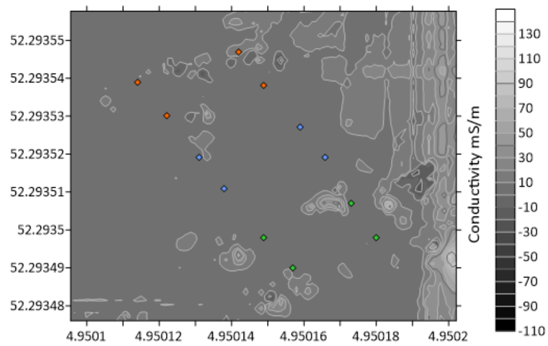

(c) s = 0.71 m, corrected conductivity, 0.5 m spacing.

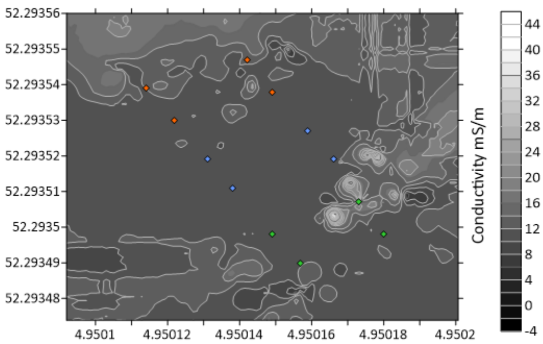

(d) s = 0.71 m, corrected conductivity, 0.25 m spacing.

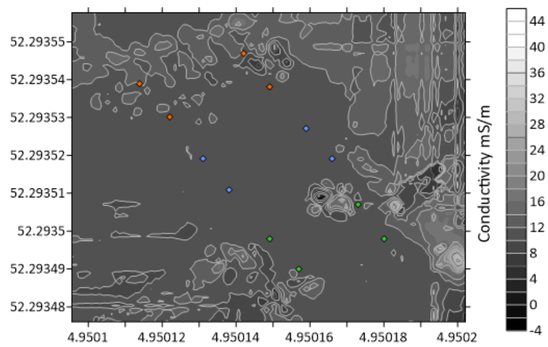

(e) s = 1.18 m, corrected conductivity, 0.5 m spacing.

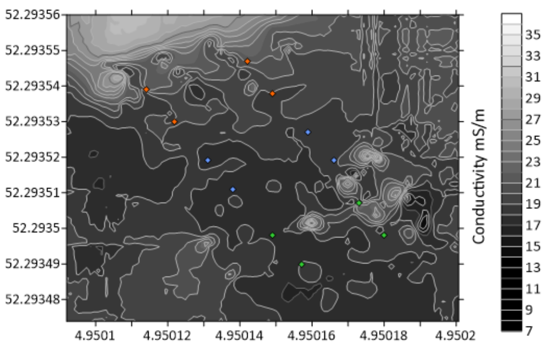

(f) s = 1.18 m, corrected conductivity, 0.25 m spacing.

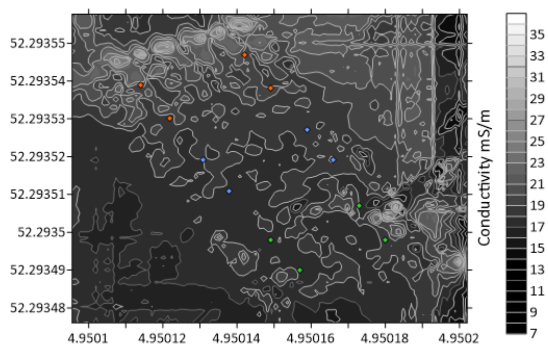

Figure B.7: Comparison between corrected conductivity collected using 0.5 m versus 0.25 m line spacing in VCP configuration on Day 2. The approximate positions of the burials are denoted by the green (burial A), blue (burial B) and orange (burial C) markers which mark the corners of the burials shown in Figure 6.2. Contour intervals are consistent across the corrections for one intercoil spacing, focusing on the individual effect caused by line spacing within at a particular depth sensitivity.

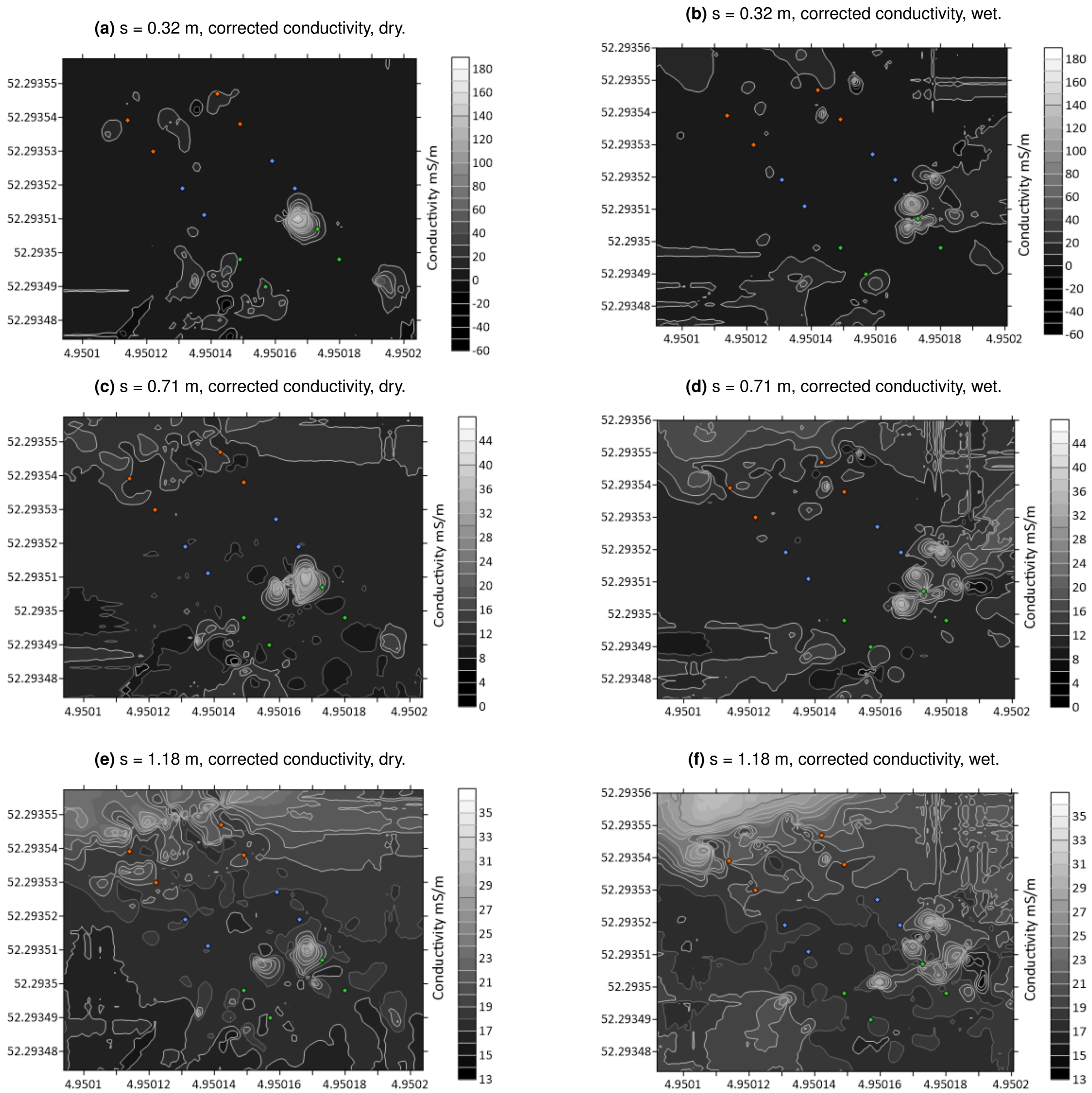

Figure B.8: Comparison between corrected conductivity collected with 0.5 m line spacing in VCP configuration on Day 1 dry conditions (right column) and Day 2 wet conditions (left column). The approximate positions of the burials are denoted by the green (burial A), blue (burial B) and orange (burial C) markers which mark the corners of the burials shown in Figure 6.2. Contour intervals are consistent across the corrections for one intercoil spacing, focusing on the individual effect caused by soil moisture at a particular depth sensitivity.

C
Leica Point Measurements

Leica Geosystems AG
Heinrich Wild Strasse
CH-9435 Heerbrugg
St. Gallen, Switzerland

Phone: + 41 71 727 3131
Fax: + 41 71 727 4674

- when it has to be right

Points Code Report

Report created: 07/06/2022 12:33:23

Project Details

General

Project Name:	ARISTA 10052022
Owner:	-
Lead Surveyor:	Kate Brooks
Date Created:	05/11/2022 10:42:46
Last Accessed:	07/06/2022 12:25:33
Application Software:	Infinity 3.6.1

Customer Details

Customer Name:	-
Contact Person:	-
Number:	-
Email:	-
Skype:	-
Website:	-

Master Coordinate System

Coordinate System Name:	RDNAPTRANS2018
Transformation Type:	Classical 3D
Residual Distribution:	None
Ellipsoid:	Bessel
Projection Type:	Customised
Geoid Model:	-
CSCS Model:	rdtrans2018

Path:	C:\Users\kateb\OneDrive\Documents\Leica Geosystems\Infinity\Projects\ARISTA 10052022\ARISTA 10052022.iprj
Size:	471.4 MB
Comments:	-

Summary

#	Point ID	Point Role	Easting [m]	Northing [m]	Ortho. Height [m]	Ellips. Height [m]	Code	Code Group	Code Description	Code Attributes	Code Annotation	Date/Time
1	grave3_01	Calculated	125,183.4319	478,484.6513	-	39.3217						05/11/2022 11:00:29
2	grave3_02	Calculated	125,182.9394	478,485.6552	-	39.3387						05/11/2022 11:00:55
3	grave3_03	Calculated	125,181.5229	478,483.6750	-	39.2992						05/11/2022 11:01:36
4	grave3_04	Calculated	125,180.8700	478,484.8833	-	39.3718						05/11/2022 11:02:06
5	grave4_01	Calculated	125,184.5018	478,482.5495	-	39.3243						05/11/2022 10:56:00
6	grave4_02	Calculated	125,184.1324	478,483.2933	-	39.3617						05/11/2022 10:56:39
7	grave4_03	Calculated	125,182.6627	478,481.5296	-	39.3783						05/11/2022 10:57:32
8	grave4_04	Calculated	125,182.0657	478,482.2506	-	39.3784						05/11/2022 10:58:09
9	grave5_01	Calculated	125,185.5770	478,480.1609	-	39.3871						05/11/2022 10:53:53
10	grave5_02	Calculated	125,185.1227	478,481.0404	-	39.3405						05/11/2022 10:54:29
11	grave5_03	Calculated	125,183.9122	478,479.2176	-	39.3768						05/11/2022 10:54:50
12	grave5_04	Calculated	125,183.2976	478,480.1162	-	39.3441						05/11/2022 10:55:23
13	GX0Y0	Fixed RTK - Tilted	125,186.7014	478,479.4755	-	39.3485						05/10/2022 12:59:52
14	GX0Y3.5	Fixed RTK - Tilted	125,183.5850	478,477.9391	-	39.3421						05/10/2022 13:00:03
15	GX8Y0	Fixed RTK - Tilted	125,183.0617	478,486.5887	-	39.3137						05/10/2022 13:00:16
16	GX8Y3.5	Fixed RTK - Tilted	125,179.9541	478,485.0907	-	39.3318						05/10/2022 13:00:27
17	RTCM-Ref 0030	GNSS Setup	121,826.8286	486,841.8286	-	72.0339						05/10/2022 12:59:40

D
Research Module

Research Module

Geophysical methods for forensic investigation: imaging and characterization of buried human remains at ARISTA

by

Kate Brooks

Supervisors (TU Delft):	Prof. dr. ir. E. Slob (e.c.slob@tudelft.nl) Dr. D. Ngan-Tillard (d.j.m.ngan-tillard@tudelft.nl) Dr. ir. D. Draganov (d.s.draganov@tudelft.nl)
Supervisor (NP):	M. Lüschen (mark.luschen@politie.nl)
Supervisor (NFI):	C. Nienaber (c.nienaber@nfi.nl)
Institution:	Delft University of Technology
Place:	Faculty of Civil Engineering and Geoscience, Delft
Project Duration:	October, 2021 - January, 2022

Cover Image: A police line (police tape) established at the scene of a car crash in the Cedar-Riverside neighborhood of Orleans. Tony Webster (2008).

Abstract

A literature review of some key geophysical methods which might be applied to homicide investigations, and an examination of their benefits and limitations with respect to the detected response, environmental and seasonal controls, temporal controls, and survey design, is presented here. These methods have been compared based on their applicability and success in the detection of a simulated clandestine grave in a known environment in the Netherlands, at the Amsterdam Research Initiative for Sub-surface Taphonomy and Anthropology test facility. Both ground penetrating radar and resisitivity methods have had the greatest success until now in the detection of clandestine bodies, while bulk ground conductivity meters and magnetic methods have fewer success in the literature. That being said, sources of interference at the test facility, in addition to soil homogeneity and age of burial, present barriers to the success of ground penetrating radar or resistivity methods independently. Based on the environment and burial targets at the test facility, the best combination of geophysical methods consists of ground penetrating radar and 2D/3D electrical resistivity tomography in addition to a preliminary bulk ground conductivity survey to identify anomalous regions and sources of interference.

Contents

1 Introduction

Forensic investigations, and in particular those related to homicide cases and the search for buried clandestine objects, demand quick and effective methods to obtain evidence and reach conclusions. Pre-excavation geophysical surveys are a non-destructive method which can provide forensic searchers with a view of the subsurface which is undisturbed and may aid in the identification of target regions which require further invasive investigation (Schultz, 2007). Recent work in forensic geophysics research aims at using simulated clandestine graves to determine the optimal detection methods and survey layouts for use in forensic homicide investigations (Molina et al., 2016). A clandestine burial is defined as a grave which is located in a remote, unrecorded location, which has been hand-excavated and sits at a depth of <1 m below the ground level (bgl) (Pringle et al., 2016). Clandestine graves, and their corresponding geophysical responses vary greatly from unmarked graveyard/cemetery burials; which are buried deeper ($\sim$ 1.8 m bgl), are contained within a coffin or other distinct material, and may contain embalming fluids which help considerably with detection (Booth and Pringle, 2016; J. Hansen et al., 2014; Pringle et al., 2020).

The majority of previous research concerning the use of geophysical surveys to locate buried human remains have approached the determination of the optimum detection techniques and configurations using controlled research sites and simulated clandestine burials. Often times pig cadavers are used as proxies for human bodies buried in clandestine graves (Booth and Pringle, 2016; Molina et al., 2016; Pringle et al., 2020). However, the use of non-human models in taphonomic research is not ideal, as studies have shown a significant forensic difference between the two species (Connor et al., 2018; Dautartas et al., 2018; Knobel et al., 2018) revealing the importance of the use of human cadavers in forensic investigations. Additionally, Forbes et al., (2005) report that close to half of 87 homicide victims recovered in clandestine burials in the U.S. were clothed or encased in material, thus both "naked" and "clothed" scenarios have often been considered in previous works (Pringle, Jervis, Hansen, et al., 2012; Pringle et al., 2016; Pringle et al., 2020).

In 2017 the Amsterdam Research Initiative for Sub-surface Taphonomy and Anthropology (ARISTA) facility opened as the first forensic cemetery in Europe (F. Hansen, 2019). The primary research goal at ARISTA is to study the decay and detection of buried cadavers in soil and weather conditions particular to the Netherlands. There are currently three cadavers buried at the ARISTA facility, two are used for entomology studies and the third for non-invasive remote sensing research (Mulder, 2019). This study concerns the geophysical detection of the third cadaver, as a proxy for detection of clandestine buried bodies in forensic investigations. The ARISTA facility has huge potential, in combination with an optimized geophysical survey design, to provide much needed information on the detectability of human remains under known environmental conditions particular to the Netherlands.

The success of a geophysical method in detecting forensic targets depends on numerous factors including geology and soil type at the site, the burial environment, the depth below ground level, time since burial, expected target size, the target composition (type) and the survey layout and equipment used. The information gathered in this literature review will be used to draw conclusions on the best geophysical methods, survey design and processing techniques specifically applied to the ARISTA forensic cemetery. First, we investigate geophysical methods being used today for the detection of clandestine graves and compare their reported advantages and shortcomings. Second, we examine in detail the site conditions, and previous works performed at the ARISTA facility. Last, we draw conclusions about which methods will be successful in the characterization of simulated clandestine graves at the ARISTA facility, in preparation for a Master's thesis project.

2
Geophysical Methods

2.1. Ground penetrating radar

Ground penetrating radar (GPR) is a geophysical technique which involves the acquisition of high frequency (10 MHz - 3 GHz) electromagnetic (EM) waves from reflections due to the presence of a subsurface contrast in dielectric permittivity and/or electrical resistivity. GPR is an EM method which exploits the wave-like nature of EM fields. This behaviour is dominant over diffuse EM field behaviour when the magnitude of energy dissipation, which is associated with electrical conductivity, is relatively small compared to energy storage, which is associated with dielectric permittivity. These conditions are typically satisfied in low-loss and low conductivity materials.

All GPR configurations involve a transmitter (source) and antenna (connected to the receiver). The transmitter sends out the signal and the receiver detects the influence on the electric field from subsurface boundaries or contrasts in relevant material properties at the antenna, which is positioned at a desired measurement location. Sources of material contrasts include soil horizons, increased water content, and in the case of forensic investigations, highly conductive metal objects, changes in density, the presence of voids or fluids, and soil compaction (Schultz, 2007). The magnitude of this contrast between the target of interest and the surrounding material is what determines the amount of energy which reflects back to the surface. GPR surveying is the most common and well tested technique used in forensic investigations involving the detection of burials associated with homicide victims, due to it's relatively quick acquisition and very high resolution (Pringle, Ruffell, et al., 2012; Schultz, 2012).

2.1.1. Survey Design

The choice of antenna frequency is a very important one in GPR surveys; in order to obtain the correct depth of penetration while maintaining vertical resolution of the target features. The central frequency, which is often referred to, is the ideal frequency at which the antenna emits most efficiently, however, the GPR emits a range of radio frequencies. GPR bandwidth is equal to the center frequency of the antenna; for example an antenna with center frequency of 500 MHz will have a range of frequencies radiated at power levels within half the power level radiated at 500 MHz, between 250 MHz and 750 MHz. The choice of frequency depends on the target size, depth bgl, geology and soil type (Pringle, Ruffell, et al., 2012). A lower frequency antenna will have a high depth of penetration in ideal conditions (for 10 - 120 MHz up to 50 m) (Schultz, 2012) but do not produce high vertical resolution. The opposite is true for high frequency antennae, which produce a short wavelength radar wave which may only penetrate a meter or less in the majority of soils, but can resolve features as small as a few cm (Schultz, 2007). High resolution however is not always advantageous; often these antennas yield too much detail, imaging small discontinuities which reflect energy but which make the true target unidentifiable (Nobes, 1999; Pringle, Jervis, Hansen, et al., 2012; Schultz, 2003). Typically antenna frequencies between 400 to 500 MHz are used in the detection of buried bodies in forensic investigations, as they strike a good balance and have the correct depth of investigation (Schultz, 2003, 2007, 2012; Schultz and Martin, 2011). However, lower frequency GPR antennae (110 to 225 MHz) were shown to be preferable in other studies, in particular to detect deeper burials and when there is extensive clutter in the subsurface (Pringle, Jervis, Hansen, et al., 2012; Schultz and Martin, 2012). Lower frequency antenna should also be considered in environments where soil properties limit the depth of penetration (Schultz and Martin, 2011). Schultz and Martin (2012) demonstrated that in sandy soil a 250 MHz antenna produced clearer reflections, as grave features were detected as one discernable reflection. Using higher frequency antennas (500 MHz) graves may appear as multiple reflection features which is more difficult to interpret. Pre-survey calibration is very important in order to evaluate which frequency will likely provide the best results.

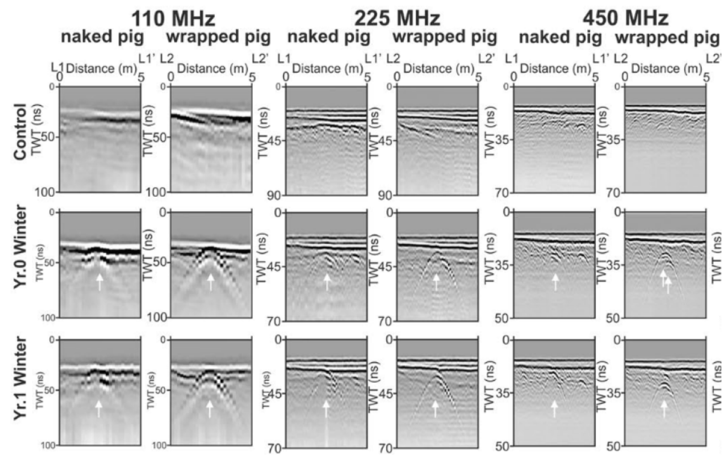

Figure 2.1: 2D GPR profiles from Pringle et al., (2020) 1 year post-burial, using 110, 225 and 450 MHz frequency across "naked" and "wrapped" pig cadavers. White arrows indicate center of grave anomaly. Control data demonstrates a break or disturbance in soil horizon, and cadaver responses are characteristic of hyperbolic-shaped anomalies.

2.1.2. Detected response

The human body has a very high concentration of water, and thus a recent burial should result in high GPR reflectivity as compared to the surrounding soil. Clandestine graves can also be detected by GPR due to contrasts in the properties of the disturbed soil in the grave, which may be less dense than the surroundings (Schultz, 2007). Additionally, it has been found that non-biological items such as items used to wrap or cover the victim are highly detectable by GPR (Pringle, Jervis, Hansen, et al., 2012; Pringle et al., 2016; Pringle et al., 2020).

In a GPR profile a clandestine burial may appear as a break or disturbance in the soil horizon or as a hyperbolic-shaped anomaly (Schultz, 2007). Disturbed soil in particular can be quite prominent in GPR sections (Johnston, 2021), appearing as a strong horizontal reflection event (Molina et al., 2016). Hansen, Pringle and Goodwin, (2014) suggest a similar response will result from rapidly dug unmarked graves, and clandestine burials of murder victims; characterized by an obvious GPR 1/2 hyperbolic reflection event. Results from GPR survey conducted by Pringle et al., (2020) over "naked" and "wrapped" cadavers is shown in Figure 2.1. Over the control grave there are clear disturbances in the soil horizon, and hyperbolic shaped anomalies over both "wrapped" and "naked" cadavers. Horizontal time slices typically show square shaped anomalies over target positions (Molina et al., 2016).

2.1.3. Environmental and seasonal controls

Radar signals get weaker as they travel within the subsurface due to attenuation; an object can only be detected using GPR if the electric field reflected back to the surface arrives at the receiver before it is completely attenuated (Johnston, 2021). Soils which are high in electrical conductivity, such as clay rich soils, reduce the GPR depth of penetration dramatically (Johnston, 2021). Favorable conditions for GPR surveys include dry and sandy soils, regions free of debris, cobbles and gravel, flat and level ground and open areas with sparse brush and trees (Schultz, 2007). Non-favourable conditions for GPR include soils saturated with water, soils with high clay and organic contents, and those which do not satisfy the other environmental conditions mentioned previously. In addition, Schultz and Martin (2012, 2011) found that in sandy homogeneous soil, with poor differentiation of soil horizons, GPR could not detect disturbed soil. However, when a diagnostic soil horizon such as a spodic horizon in their study is disturbed, then the grave may be detected (Schultz and Martin, 2012). This is another control in which the local environment may impact the detectability of a clandestine grave.

Seasonal controls of GPR responses to clandestine burials are very minimal, as demonstrated by Booth and Pringle (2016) who found no systematic evolution of the GPR response to simulated graves over their survey period. Schultz and Martin (2012) did find that during rainy seasons and following rainfall events increased soil moisture may act as a mechanism to highlight graves; as rainfall events increased decomposition of the target resulting in an increase in soil conductivity surrounding the body.

Due to the fact that GPR surveys are highly sensitive to changes in the environmental state of the host, and not to changes in the conditions of the burial, dating remains is very difficult using GPR (Booth and Pringle, 2016).

2.1.4. Temporal controls

The human body should produce high GPR reflectivity when compared to the surrounding soil, due to the presence of water in the body (Johnston, 2021). However over time the body loses mass and water, and the contrast between the surrounding soil and the body decreases dramatically. This effect has been shown by Nobes (1999) who found that the age of burial is important, as target detection and signature vary considerably over time. Work by Pringle, Jervis, Hansen, et al., (2012) systematically measuring the geophysical response of clandestine burials from 0-3 years post burial was continued in Pringle et al., (2016) for 4-6 years post burial and Pringle et al., (2020) up to 10 years post burial. These investigations were performed on made ground, consisting of a thin shallow layer (0.01 m) of organic-rich top soil, underlain by predominantly natural sandy loam with graves excavated to 0.5 m bgl. Pringle et al., (2016) found that when using a central frequency of 225 MHz a "naked burial" is detected, albeit poorly, up to 5 years post burial, while using all other frequencies this was not the case. Conversely, "wrapped" cadavers were detected 10 years post burial (Pringle et al., 2020). Wrapped surfaces create a larger material contrast as opposed to a decomposing "naked" cadaver which produces a smaller reflection and greater attenuation of the GPR signal. The optimal central frequency for detection of both "naked" and "wrapped" cadavers was determined to be 225 to 450 MHz due to less non-target anomalies, good target resolution and high data acquisition speed (Pringle et al., 2016; Pringle et al., 2020). Compaction, in particular in sandy soils, may result in the reduction in contrast between grave fill and surrounding soil, reducing the GPR reflectivity and thus the ease of detecting a buried body (Schultz and Martin, 2011). In general the sooner post burial the geophysical surveys can be taken the higher chance of detection.

2.2. Resistivity methods

Electrical resistivity methods aim to determine the resistivity distribution in the subsurface. The subsurface resistivity is dependent on the electric parameters of the volume of interest. For forensic investigations these will be similar to those listed for GPR, including water content, the presence of conductive metal objects, changes in density and porosity in the soil, presence of fluid and/or voids, and soil compaction (Loke, 2015). All active source resistivity methods involve the introduction of a current (I) of known magnitude into the subsurface via two current-electrodes. Subsequently the electric potential (V) difference can be measured on the surface by potential-electrodes. The electric potential can be measured at numerous locations in the subsurface by varying the position of the two potential-electrodes. In order to determine the apparent resistivity of the subsurface, we need to consider the finite distance between the position at which the electric potential is measured and where the current is injected. The geometric factor k contains a measure of this distance, and thus the apparent resistivity is given by:

$$\rho_a = \frac{V}{I}k \tag{2.1}$$

The geometric factor k depends on the electrode configuration used in the survey. Common electrode configurations include dipole-dipole, Wenner and Schlumberger; they differ in electrode distance and order. The apparent resistivity ρ_a is determined under the assumption of an entirely homogeneous subsurface. An estimate of the true resistivity model of the subsurface is obtained through implementation of an inversion scheme, which incorporates resistivity variations in the ground as well as taking the topography into account.

2.2.1. Survey Design

Two resistivity methods are primarily used in forensic investigations: horizontal profiling techniques and vertical profiling techniques. An example of horizontal profiling is the fixed offset, twin-electrode array. This system has four probes, one current and one voltage probe located on a mobile frame with fixed offset which collect survey readings. The other current and voltage probes are placed remotely at a fixed position, with large offset from each-other, as well as from the mobile electrodes (Milsom and Eriksen, 2011). This survey design prioritizes horizontal resolution, and can be completed quite rapidly. The result of such data acquisition produces a bulk ground resistivity profile, demonstrating resistivity anomalies across a survey grid in 2D, providing no resistivity information at depth. This method has been used successfully in a number of surveys which are looking at the detection of simulated clandestine burials (J. Hansen et al., 2014; Jervis et al., 2009; Pringle, Jervis, Hansen, et al., 2012; Pringle et al., 2016; Pringle et al., 2020).

Vertical profiling techniques, are the combination of many electrodes to complete vertical electric soundings (VES), which uses fixed midpoint and multiple distances between electrodes, and the aforementioned horizontal profiling simultaneously (Reynolds, 2011). These techniques are more common in geological applications as they make use of long linear arrays of many electrodes with fixed spacing. These systems, for example electrical resistivity tomography (ERT), incorporate the acquisition of repeated measurements at different electrode spacing at multiple points along the electrode array, allowing for the generation of vertical profiles and tomography. A combination of current and potential electrode pairs is used to generate a pseudo cross-section of apparent resistivity below the survey line. These methods have the added flexibility of using a number of different array configurations. The depth of investigation achieved by these methods depends on the electrode separation, geometry and array configuration. Often times fixed resistivity surveys are preferred in searches over ERT due to their coverage of the subsurface (J. Hansen et al., 2014; Jervis et al., 2009; Pringle, Ruffell, et al., 2012), however ERT has the advantage of providing depth information, and has been collected over clandestine burials in previous works successfully (Pringle, Jervis, Hansen, et al., 2012; Pringle et al., 2016; Pringle et al., 2020).

Given that the value of the measured apparent resistivity depends on the electrode array geometry, this is an important consideration in resistivity survey design. There are over 102 different surface array types, however the three main types are Wenner, Schlumberger and dipole-dipole arrays (Ellwood, 1990; Reynolds, 2011). Each array type has advantages, disadvantages and sensitivities. The Wenner array was used by Ellwood et al., (1994) in a bulk ground resistivity survey to image and locate clandestine graves. In a study conducting ERT measurements of clandestine graves in grassed, sandy soil, semi-rural environment Pringle, Jervis, Hansen, et al., (2012) determined the Wenner array configuration to be optimal. Jervis et al., (2009) completed dipole-dipole bulk ground resistivity surveys over simulated clandestine burials demonstrating that a small survey grid pattern (0.25 to 0.5 m spaced data point sampling) was important in order to resolve comparatively small spatial targets. The principal disadvantage of resistivity surveys, and something which should be considered in survey planning is that they are slow, and require very dense sampling in order to resolve individual graves (Jones, 2008). The acquisition of 3D ERT is advantageous in order to obtain information across the extent of a plausible grave area, in addition to depth information. There are two methods in which 3D ERT surveys may be acquired. The first being through the acquisition of 2 sets of multiple parallel, equally spaced 2D arrays positioned perpendicular to one another forming a grid which allows for the generation of a 3D image from 2D data (Mulder, 2019). The second is an inherently 3D survey, wherein sets of 2 electrodes are selected and combinations of surrounding electrodes at a certain distance are used to measure the potential outside of the 2D plane (Mulder, 2019). In order to complete 3D surveys in a reasonable time frame, the optimization of survey design is required through a comprehensive acquisition geometry, consisting of a square grid, with equally spaced electrodes in the x and y directions.

2.2.2. Detected response

Multiple works have found that decompositional fluids are the dominant factor in clandestine grave detection using electrical resistivity methods (Jervis et al., 2009; Pringle, Jervis, Hansen, et al., 2012). Decompositional fluids may be retained in the soil for considerable periods of time post burial and may then be detected due to a rise in electrical conductivity measured by electrical resistivity surveys (Juerges et al., 2010).

The response over a clandestine burial is expected to be a low resistivity anomaly (Pringle, Ruffell, et al., 2012). The source of this anomaly being the increased soil porosity and the presence of decompositional fluids, both of which increase the conductivity of the soil (Jervis et al., 2009). However, Jervis et al., (2009) also found that the resistivity response to a "wrapped" pig cadaver in a simulated clandestine burial was a high resistivity anomaly, suggesting that wrapping the cadaver prevents decompositional fluids from entering the soil, and thus creating a barrier to electrical conduction. These findings are also supported by the findings from Pringle, Jervis, Hansen et al., (2012); Pringle et al., (2016); Pringle et al., (2020) and further demonstrated in Figure 2.2.

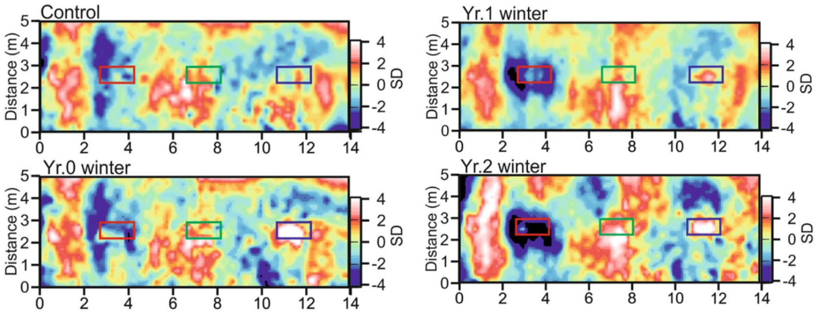

Figure 2.2: Electrode resistivity mapping (ERM) from Pringle et al., (2020) for up to 2 years post-burial. Left: naked pig, Middle: empty burial, Right: naked pig.

2.2.3. Environmental and seasonal controls

Bulk-ground resistivity surveys have the advantage that they are less affected by above-ground interference as compared to other methods, due to the fact that probes are physically inserted into the ground (Milsom and Eriksen, 2011). In the case were GPR is not suitable due to the presence of clay-rich soils and in environments with numerous trees (woodland regions), ERT is often selected for use in detection of clandestine graves (Molina et al., 2020).

Pringle, Jervis, Hansen et al., (2012) found that the success of electrical resistivity methods in detecting clandestine burials depends on the burial style, soil type and time since burial. Studies have shown that local variations in soil moisture content when surveying in dry conditions in heterogeneous soil may have a masking effect on the desired targets (Ellwood et al., 1994; Jones, 2008). Thus, the best time to complete a survey is during the winter months because under dry conditions in the spring and summer, many anomalies are present which mask the targets as a result of heterogeneous soil (Jervis et al., 2009). The largest field problem encountered in resistivity surveys is high electrode contact resistance, which is common in regions consisting of dry sand, boulders, gravel and frozen ground (Reynolds, 2011).

2.2.4. Temporal controls

The decompositional fluid conductivity of simulated clandestine graves has been found to change significantly over time (Pringle, Ruffell, et al., 2012). Temporal changes in the electrical resistivity response using fixed-offset and electrical resistivity imaging (ERI) were systematically measured from 0-3 years post burial (Pringle, Jervis, Hansen, et al., 2012), for 4-6 years post burial (Pringle et al., 2016) and up to 10 years post burial (Pringle et al., 2020) of both "wrapped" and "naked" pig cadavers. In the 0-3 year study, "naked" cadavers were detected as a low-resistance anomaly up to 2.5 years post-burial (Pringle, Ruffell, et al., 2012). However, after 4 years "naked" cadavers are very difficult to identify using fixed-offset methods, and for ERI the same was found after 5 years (Pringle et al., 2016). This is due to the migration of decompositional fluids overtime, which may result in the detection of resistivity anomalies in locations which are not consistent with target locations. Conversely, "wrapped" cadavers resulted in consistent, large high resistance anomaly up to 10 years post burial in both resistivity methods (Pringle et al., 2020). This is likely due to the wrapping acting as a barrier to decompositional fluid migration into the surrounding soil, limiting electrical conduction.

2.3. Electromagnetic induction methods

Electromagnetic induction methods combine the principles from Ampere's law and Faraday's law to obtain the apparent soil conductivity as it varies across space (Bigman, 2012). Conductivity meters measure the relative change in ground conductivity between the background material and the targets through the induction of an electromagnetic current (Reynolds, 2011). EM ground conductivity meters come in many forms, some are small-loop frequency-domain EM systems containing two small coils, separated by a set distance, while others might have multiple coils separated by flexible distances (Reynolds, 2011). In the former case, one coil acts as a transmitting antenna, and the other as a receiving antenna as the device is moved along a survey transect (Reynolds, 2011). The transmitting antenna generates an electromagnetic field which induces an electric current in the receiving antenna. This results in the generation of a primary magnetic field which is defined as the part of the magnetic field which would be present even in the absence of the earth. The resulting electromagnetic response of the ground to this primary field is a secondary magnetic field which passes through the receiving coil and induces current flow (Bigman, 2012). The total measurement, containing contributions from both the primary and secondary magnetic field is obtained by the instrument and subsequently divided by the predicted background noise. There are two components which make up the magnitude of the secondary field, the In-Phase component (the real part) and the Quadrature (the imaginary part). From this the low induction number (LIN) approximation is made. The LIN approach, is an approximation used to compute the apparent conductivity of the subsurface in a highly resistive medium (Beamish, 2011). This approximation is valid when the separation distance between the transmitter and the receiver is much smaller than skin depth. For different EM instruments this limit is reached at different subsurface resistivities (Beamish, 2011). As long as the LIN approximation is valid you can assume a constant sounding depth, and the Quadrature component can be taken as an approximate linear measure of the apparent conductivity of the ground. The CMD-Mini explorer from GF Instruments, measures the apparent conductivity (mS/m) and inphase ratio (ppt: parts per thousand) of the secondary field, however the inphase ratio is rarely used (GF Instruments, 2020).

2.3.1. Survey Design

In theory, one advantage to EM methods is that they can focus on different depths below the surface, depending on the depth of burial of the grave and local ground conditions. Unfortunately the reality isn't so straight forward, in fact sensitivity is always highest near the transducers. The sensitivity volume does increase when the frequency is reduced or the inter-coil spacing is increased. So in theory by obtaining measurements at different frequencies, varying depths of exploration can be obtained (Reynolds, 2011). In summary, objects located at greater depths might be detectable by lower frequencies in the case that they are not within the volume of sensitivity for higher frequencies or smaller coil spacing. The CMD-Mini explorer has a said effective depth range of 0.5 / 0.25 m, 1.0/0.5 m and 1.8/0.9 m, depending on the distance between the two dipoles which can be adjusted (GF Instruments, 2020).

Two major drawbacks of conductivity meters is their low resolution and slow continuous sampling, often collecting data up to a maximum of 2 readings per second (Clay, 2006). This rate is fast enough to detect large features such as ditches, however it may not provide close enough sampling intervals to resolve burials (Bigman, 2012). One way to get around the low sampling speed is to identify and use the most appropriate single frequency in a multifrequency system. Bigman (2012) was able to record 8 measurements per second using a GEM-300 conductivity meter, providing higher resolution measurements. Bulk ground conductivity surveys may be useful in conjunction with other methods, not in the identification of individual graves, but in order to rapidly characterize and determine the spatial limits of a burial site (Dick et al., 2015). EM surveys using ground conductivity meters might also be used in order to evaluate background conductivity values at a forensic search site, in order to assess the extent of radar attenuation (Nobes, 1999).

2.3.2. Detected response

Apparent conductivity measurements are influenced by material properties, size, shape, orientation of the object and porosity/compaction of the soil; the same parameters which influence resistivity methods described previously (Bigman, 2012). As it applies to forensic investigations, variations in apparent conductivity may result from mixing of the topsoil and subsoil, differences in compaction and air cavities and the disturbed soil in the filled grave shaft (Bigman, 2012). The electromagnetic response from a buried object can be an anomalous positive response, with possible negative side lobes, or may also appear as the opposite case, depending on the contrast between the grave contents and the surroundings (Nobes, 1999). Pringle and Jervis (2010) collected in-situ temporal conductivity data in a simulated clandestine grave using a lysimeter over a two year study period and found increasing conductivity levels with respect to background values over the course of the study. This suggests that the clandestine burials might be detected by conductivity meters due to the release of decompositional fluids, as in resistivity surveys, however this has not been demonstrated in any published works. Seasonality may also impact measures of apparent conductivity, as Bigman (2012) suggest that moisture in the soil improves the contrast between the resistive grave materials (prehistoric burials) such as bone, and the surrounding soil matrix.

Ground conductivity meters have been found to successfully identify shafts and tomb chambers (Frohlich and Lancaster, 1986). Regarding the detection of prehistoric burial chambers, Frohlich and Lancaster (1986) found higher apparent conductivity over infilled chambers, and lower apparent conductivity over intact chambers, which were filled with air. However, in cases where the cavities were small and there was low contrast between the burial material and the surrounding soil the burials were not resolvable. Bigman (2012) had success in locating prehistoric and historic North American burials using GEM-300 conductivity meter, with anomalies appearing in a very distinct manner as a signature of low apparent conductivity. These results are shown in Figure 2.3. The low conductivity values are likely due to differences in compaction and air cavities and the disturbed soil in the filled grave shaft. EM surveys conducted by France et al., (1992) in the Western US were able to locate simulated clandestine burials of pig cadavers. Typically EM conductivity meters are less sensitive then resistance meters to the same phenomena, however they are favorable over resistivity techniques in some environments (Jones, 2008).

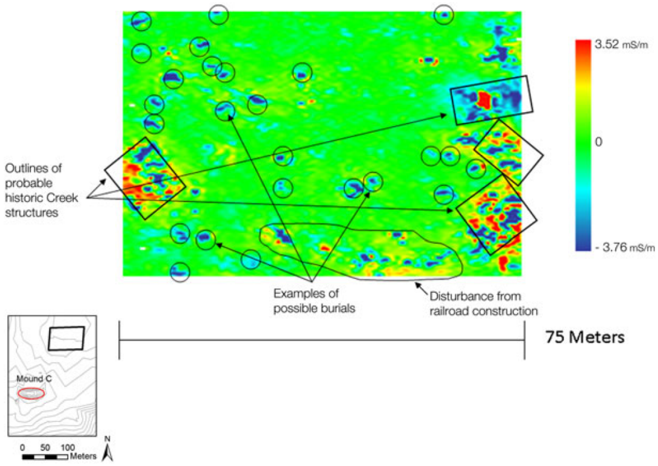

Figure 2.3: Conductivity data from Bigman (2012) obtained using GEM-300 EM induction instrument. Anomalies representing prehistoric and historic North American burials appear as distinct low apparent conductivity anomalies. However numerous other anomalies are present due to soil disturbances from other sources.

2.3.3. Environmental and seasonal controls

The advantages of electromagnetic surveys is their ability to conduct surveys rapidly and within a large variety of landscapes (Pringle, Ruffell, et al., 2012). EM conduction meters eliminate the need for probe contact required in electrical resistivity techniques, which is of particular importance in sensitive areas, such as forensic search areas (Bigman, 2012). However there has been very limited use of EM surveys in law enforcement investigations (Pringle, Ruffell, et al., 2012).

Performing electromagnetic conductivity surveys in urban environments is highly problematic for the detection of targets (Dick et al., 2015). Nobes (1999) had difficulty differentiating anomalies from unmarked graves in a cemetery due to significant background interference from fence boundaries and local topography. In general, EM survey equipment is very sensitive to above ground conductive objects, which often removes the potential for using them in typical search areas, such as urban environments (Reynolds, 2011). In a study by Molina et al., (2016), bulk ground conductivity survey results produced poorly detectable individual anomalies over simulated clandestine graves.

2.4. Magnetic methods

Magnetic methods are geophysical tools which detect variations in the Earth's magnetic field due to the presence of nearby objects (Pringle et al., 2015). Any object placed in a magnetic field acquires a magnetization, although to which degree this occurs is highly varied (Milsom, 2003). Magnetic susceptibility is a geologically diagnostic parameter which describes how susceptible a material is to becoming magnetised (Reynolds, 2011). Materials and objects which are metallic have very high magnetic susceptibility, and are highly detectable using magnetic methods and likely contain a high concentration of ferro- and ferri-magnetic minerals (Reynolds, 2011). Magnetic susceptibility meters measure the variations in magnetic susceptibility in the subsurface. The ambient magnetic field is of interest in geophysical investigations, as it describes the Earth's magnetic field at a particular location on the Earth's surface due to contributions from the local surroundings and the subsurface.

Magnetometers are geomagnetic instruments which measure the horizontal and vertical components of the ambient magnetic field, or the total ambient magnetic field which is affected by the presence or proximity of ferro-magnetic minerals, their orientation and depth bgl (Milsom and Eriksen, 2011; Reynolds, 2011). Fluxgate magnetometers comprise 2 copper wires surrounding magnetic cores. An AC current is passed through one coil, inducing a magnetic field in both cores. The secondary voltages in the coils cancel out at all times, however in the presence of the ambient external field the secondary voltage shifts (Reynolds, 2011). This shift in voltage is measured by the magnetometer, and is proportional to the magnitude of the external field component. Fluxgate magnetometers measure specific components of the ambient magnetic field. A very similar theory is applied in resonance magnetometers, however the magnetic core is exchanged for proton-rich liquid or alkali-vapour cell. The primary difference between these so called "resonance magnetometers" and fluxgate magnetometers is that these devices monitor the behaviour of atomic particles in an ambient magnetic field to provide an absolute measure of the total magnetic field, rather than vector components of the field (Reynolds, 2011).

Magnetic gradiometers are geomagnetic instruments which employ two identical magnetometers separated by a small distance and measure the difference in total magnetic field strength between them (Reynolds, 2011). Gradient measurements are particularly useful in archaeological and environmental work as they emphasize near surface sources, suppressing long-wavelength sources (Milsom, 2003) and require no correction for diurnal variations (Reynolds, 2011).

2.4.1. Survey Design

In a survey comparing magnetic susceptibility and gradiometry methods in the detection of forensic and metallic objects, the magnetic susceptibility method proved more successful in detecting target objects. Fluxgate and magnetic gradiometry survey results have been found to be difficult to interpret due to the subtlety of anomalies resulting from target metal objects (J. Hansen and Pringle, 2013). In this study it is suggested that without the comparison to control data, the target locations would not have been identified. In general, magnetometers are more successful in the detection of forensic landmine and UXO clearance and detection, over their use in burial detection (Pringle, Ruffell, et al., 2012).

2.4.2. Detected response

The magnetic response to a buried object might be either a positive or negative peak, or positive and negative transitions depending on whether the grave and its contents are more or less magnetic than the surrounding soil (Nobes, 1999). Molina et al., (2016) conducted magnetic susceptibility surveys over simulated clandestine burials and found that these measurements were likely picking up the disturbed grave soil rather then the desired targets, given that the empty control grave had a more defined anomaly. Thus, magnetic methods typically detect variations in soil composition, rather than objects in the grave itself; unless metal objects are present.

Magnetometer surveys can be conducted very rapidly (Jones, 2008). However, the presence of igneous rocks and other ferrous materials such as metal objects, may obscure more subtle patterns when trying to locate clandestine graves (Jones, 2008). In cemeteries and graveyards, highly magnetic materials are often present in burials, such as steel or iron in caskets, coffins or vaults, stone or brick monuments, which render the graves highly detectable by magnetic surveys. However, in the detection of clandestine graves, the presence of these materials is less likely and thus their detection relies on anomalies from disturbed or compacted soils, which may appear as a magnetic low (Jones, 2008). These different source types and their characteristic anomalies are shown in Figure 2.4 for reference. It's important to note that this data comes from unmarked graves at a cemetery, which has a much different burial environment and targets as compared to clandestine burials.

2.4.3. Environmental and seasonal controls

Magnetic techniques have often proven to be unsuccessful in forensic applications as they commonly suffer from interference due to the presence of both surface and subsurface objects (Pringle et al., 2015).

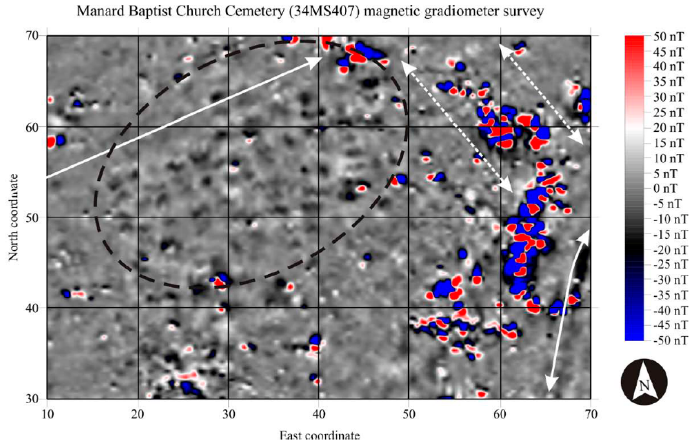

Figure 2.4: Results from magnetic survey presented by Jones (2008). Survey was completed at Manard Baptist Church Cemetery (Camp Gruber, OK). Strong magnetic anomalies are due to ferrous metal sources, while more subtle anomalies in the gray-scale range are likely disturbed and compacted soils. The black outline is an area containing cemetery patterns and white lines indicate linear anomalies.

Pringle et al., (2008) found that magnetic susceptibility surveys were not able to resolve a clandestine grave to a high degree in an urban depositional environment. The source of the poor results in this work are due to the presence of disturbed soils across the grave site which act to mask the grave location (Pringle et al., 2008). Magnetic susceptibility techniques are likely more effective in environments with very shallow soil strata, wherein the disturbance of soil from the generation of a grave may result in soil from deeper layers being brought towards the surface (Pringle et al., 2008). This effect increases the contrast in magnetic susceptibility between surrounding soil and the grave fill soil and thus increasing the detectability of the grave.

Magnetic gradiometry data over a simulated clandestine grave in an urban environment produced results which were difficult to identify, which the authors presume is due to the lack of ferrous materials present in the grave (Pringle et al., 2008). Pringle et al., (2008) suggest that magnetic gradiometry surveys are more appropriate for graves 10+ years old rather than recent graves, as bacterial action is thought to enhance the magnetic signal over time.

Pringle et al., (2015) present a magnetic susceptibility survey which was successful in detection of disturbed ground with no forensic object present, over one year post-disturbance. The disturbed ground showed anomalous high susceptibility measurements compared to background values (Pringle et al., 2015). Thus suggesting that the magnetic susceptibility technique is successful in detecting an area of disturbance in heterogeneous soil across a one year time period in a varied temperate climate (Pringle et al., 2015). However, this work also completed magnetic susceptibility surveys over simulated clandestine graves in an urban environment in clay-rich soil and were unsuccessful at resolving the grave. There were high values measured over the target, however a number of other positions in the survey grid had similar MS values, likely due to the presence of other disturbed ground. In a coastal environment, the simulated clandestine burial was successfully detected, likely due to the presence of highly heterogeneous soil. However the authors note that magnetic susceptibility surveys run into difficulties in detecting objects at sites with homogeneous soils where very little material disturbance would result from the burial (Pringle et al., 2015). In general, magnetic survey results over simulated, recent burial clandestine grave, have not been successful in a wide range of environments (Juerges et al., 2010).

3
ARISTA test facility

The first taphonomic research facility in Europe, ARISTA, was instated in 2017. This facility is used to investigate the decomposition and detection of buried human bodies under known conditions. The North-Holland province within which the ARISTA facility is located was drained and filled during the early 20th century, the sediment fill being mainly sand and peaty soil taken from nearby lakes (Oostra et al., 2020). When the facility was being constructed the surface of the terrain was levelled, involving the removal of large-sized heaps of soil and large vegetation, such as birches and bramble (Oostra et al., 2020). The remaining vegetation was left in-situ in order to maintain a natural state. The test site consists of a 32 x 18 m plot enclosed by a large 3 m high fence which extends 1 m into the ground.

3.1. Soil Analysis

The resulting terrain within which the graves at the ARISTA facility currently sit consists of 1 m thick layer of homogeneous sand of various types and some peat (Oostra et al., 2020). This layer is covered by 10-20 cm of humus-rich topsoil (Buijs and Skinner, 2021). The groundwater table fluctuates around 70 cm depth, and is tilted slightly down towards the north-west (Oostra et al., 2020). The results of a soil analysis conducted at the site suggest that the sand fraction of all samples was above 94.8% (Buijs and Skinner, 2021). A single sample was taken from the top 5 cm of soil and it was found that a much higher amount of organic matter was present here, thus the topsoil contains higher organic material such as dead leaves, insects, microorganisms etc. (Buijs and Skinner, 2021). The electrical conductivity at the site was consistent across sample locations, ranging between 60.7 to 114 muS/m. The top 5 cm of the single topsoil sample shows an electrical conductivity of 228.0 muS/m.

3.2. Burial Sites

In March, 2018 the first inhumation took place involving the burial of a recently deceased donor, and a second pit which was empty and used for reference purposes (Oostra et al., 2020). These are the two graves which are available for geophysical investigation at the ARISTA facility, one refilled empty pit and one containing a human cadaver. Both graves were generated at the same time, and neither grave has been exhumed since burial (F. Hansen, 2019). The pits were both dug 2 m long, 80 cm wide and 60 cm deep. The location of the two pits were buried in the northwest corner of the terrain which correlated to the lowest level of the groundwater table, with the goal in mind to prevent taphonomic contamination of nearby graves (Oostra et al., 2020). The cadaver was buried at 0.6 m depth, thus the top of the body is expected at approximately 0.3 m below the surface, though compaction of the soil since burial may cause this approximate depth to increase (F. Hansen, 2019). Temperature probes, and humidity probes were buried with the body for taphonomy studies. Cables connecting the sensors to multiplexers are also present, they run through a trench located between each grave and the path, which is between the graves at 1 m distance (F. Hansen, 2019). Both graves are located in very close proximity (within 1 m) of a fence supported by metal poles and a small metal plate in the ground (F. Hansen, 2019). Previous works observed that the sand was very loose on top of the graves and raised about 5 cm up when compared to the surrounding ground (F. Hansen, 2019; Mulder, 2019). In 2020 the decomposition state of the body was expected to be around stage 4 to 5, between complete skeletonization and the continued decomposition of soft tissues by enzymes, micro-organisms and insects (F. Hansen, 2019).

3.3. Previous Works

Hansen (2019) completed a Bachelors thesis investigation at the ARISTA facility, performing GPR measurements using the 250-MHz pulseEKKO instrument. Common-offset and common-midpoint lines were obtained over the burial areas. The results of this work found that a high degree of interference was seen in almost all common-offset GPR lines due to the close proximity of metal objects (ie. metal fences within 1 m of burials and a metal plate) and trenches to the target graves. For example, the presence of the metal plate generated echoing signals in the data affecting the entire line. The interference was not the same for both graves, thus it's hard to determine which anomalies might be attributed to grave contents, and which to interference. This significantly hampered their ability to interpret the GPR data of both burials. In addition, the use of 250 MHz GPR at the ARISTA facility lead to a penetration depth three times greater than the maximum grave depths, due to high radar velocity in the sandy soil at the test site (F. Hansen, 2019). In future the authors recommended the use of 500-MHz antenna at the ARISTA facility, which would provide higher resolution data which would encourage the distinction between interference effects and responses from the graves themselves.

Mulder (2019) completed ERT measurements as a portion of a Bachelors thesis at the site, however ran into significant technical issues and thus did not produce any results. They used 2D dipole-dipole and 3D dipole-dipole geometries to acquire the data, with 0.3 m spacing between electrodes. Measurements were taken 4 times, with 50 V, 100 V and then twice more in reciprocal. This method has a lot of potential for use in future works.

4
Discussion and Outlook

When determining the optimum geophysical technique to use in a particular case, considerations are often exhaustive due to the extremely case-specific nature of forensic investigations. At minimum the key considerations should be the geology and soil type at the site, the burial environment, the depth below ground level, time since burial, expected target size, and the target composition (Pringle, Ruffell, et al., 2012). A table summarizing the key considerations given what we know of the burial and the study site from previous works, alongside the aforementioned geophysical methods is presented in Figure 4.1. Each method has been given a color-coded grade which corresponds to the efficacy of that method in relationship to one of the key considerations. This table will help to guide the following discussion on which method/s might be most successful in characterizing the simulated clandestine grave and the empty pit at the ARISTA test site.

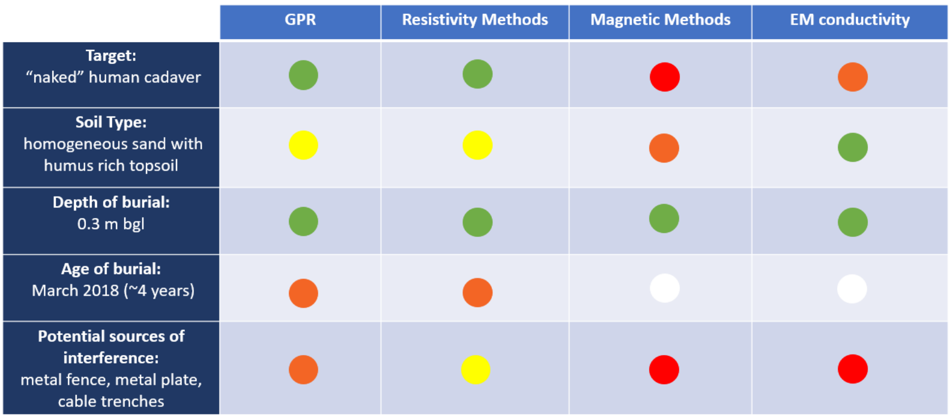

Figure 4.1: Table containing the key considerations at the ARISTA test facility. The relative efficacy/ suitability of each technique with regards to each key consideration is shown by a 4 level colour scale. Green = highly suitable, Yellow = some special considerations required, Orange = large concerns regarding suitability, Red = very large concerns which are difficult to overcome, White = suitability is not well known.

When first considering the target type, a human cadaver which is buried without "wrapping"; both GPR and resistivity methods have successfully detected these targets to a high degree, however very little evidence is present in the literature to suggest that magnetic methods and conductivity meters have the same ability. Given this fact, and the absence of high contrast features such as buried metal objects or wrapping, both magnetic methods and conductivity meters have been ruled out as the primary method of detection at the ARISTA facility.

The environment at the ARISTA facility is theoretically favorable for GPR and thus we expect the target response over the burial to be a 1/2 hyperbolic-shaped anomaly or a break or disturbance in the soil horizon. However, the detection of the burial pit, as a region of disturbed soil, might be difficult given the homogeneity of the soil and what is inferred to be likely poor differentiation of soil horizons. The presence of sources of high interference such as the metal fence and plate so near to the burial and pit represent the largest challenge in target detection. In order to mitigate these effects Hansen (2019) suggested the use of 500 MHz antenna which provides higher resolution and might also allow for the differentiation between interference patterns and target response. Given that the age of the burial is approximately 4 years, another important consideration is the detectability due to aging; a 225 MHz antenna was able to detect "naked" burials up to 5 years post burial, however the same detection with higher frequency antenna is difficult as the response appears as multiple reflection features (Pringle, Jervis, Hansen, et al., 2012). The use of visualization using horizontal time-slices might be a key distinguishing factor when implementing higher frequency antennas at this site.

Resistivity methods are likely to be less influenced by the noise sources present at the test site, given that probes are physically inserted into the ground. The expected response is low resitivity anomalies over both the burial and pit, however due to the presence of decompositional fluids the burial should be distinguished by a lower resistivity response. The soil environment is suitable for resistivity surveys, however it is important to pay attention to contact resistance and preferrable to complete surveys in the winter to prevent anomalies due to soil drainage. Regarding the burial age, works have found "naked" burials to be detectable up to 4 years post burial using fixed-offset methods, and 5 years using electrical resistivity imaging (ERI) methods (Pringle et al., 2016). Suggesting that ERI or ERT is better for investigations on older burials, in addition to providing depth information. The use of small survey grid pattern as suggested by Mulder (2019) and Jervis et al., (2009), is essential for the detection of clandestine graves, between 0.25 to 0.5 m electrode spacing is ideal. Both Wenner and dipole-dipole array types have been used successfully to detect clandestine graves.

Using a combination of detection techniques has the potential to greatly improve the detectability of the desired targets. There have been a few studies which look at the use of multiple geophysical techniques in forensic searches (Dick et al., 2015; J. Hansen and Pringle, 2013; Molina et al., 2016; Pringle et al., 2008; Pringle et al., 2016). The work by Pringle et al., (2008) recommend a combined geophysical investigation of clandestine graves consisting of a preliminary bulk ground resistivity survey, followed by closely spaced GPR and ERT 2D profiles in regions of known high conductivity anomalies in order to resolve the target. In such a case, a preliminary bulk ground conductivity survey might be used instead of a bulk ground resistivity survey given equipment accessibility and rapidity of coverage.

The suggested geophysical investigation at this site to characterize both the burial and refilled pit involves the combined use of methods. The bulk ground conductivity meter CMD-Mini explorer will be used to obtain a preliminary conductivity survey of the study area, followed by more in-depth investigation over the burial and pit using GPR and ERT to characterize the responses from both targets. The CMD-Mini explorer will be used to rapidly determine the spatial extent of the burial site, at a chosen depth of 0.5 / 0.25 m. For GPR a common-offset device with 500 MHz antenna will be used, given the recommendations by Hansen (2019) and others. Collection of GPR is best done in grid survey configurations; this layout allows for the generation of depth slices forming a horizontal map from the combination of vertical slices at a particular depth (Johnston, 2021). GPR survey grids, consisting of closely spaced lines will be completed over both the burial and pit, ensuring that multiple GPR lines intersect the burials. In an ideal case the line spacing should be equal to the antenna length (Johnston, 2021), and given that the survey area is small, this survey configuration can be completed in a reasonable time frame. Acquisition of GPR data will help to determine whether under known soil conditions the presence of a human cadaver in homogenous soil is differentiable for an infilled pit. ERT is selected as the resistivity method as it provides depth information, and is more successful in the detection of burials 4+ years after generation, as compared to the fixed-offset method. An electrode spacing of 0.3 m is suggested, based on previous work by Mulder (2019). Based on the time allotted for resistivity surveying, both 3D and 2D dipole-dipole electrode arrays may be implemented. These methods require a grid survey layout, with electrodes positioned in parallel lines with equidistant spacing in both x and y directions. The combination of all three of these techniques will allow for direct comparison between methods, providing a greater opportunity to rule out interference effects and characterize the response from a burial versus an infilled pit.

References

Beamish, D. (2011). Low induction number, ground conductivity meters: A correction procedure in the absence of magnetic effects. *Journal of Applied Geophysics*, *75*(2), 244–253. https://doi.org/10.1016/J.JAPPGEO.2011.07.005

Bigman, D. P. (2012). The use of electromagnetic induction in locating graves and mapping cemeteries: An Example from native North America. *Archaeological Prospection*, *19*(1), 31–39. https://doi.org/10.1002/ARP.1416

Booth, A., & Pringle, J. (2016). Semblance analysis to assess GPR data from a five-year forensic study of simulated clandestine graves. *Journal of Applied Geophysics*, *125*, 37–44. https://doi.org/10.1016/J.JAPPGEO.2015.11.016

Buijs, L., & Skinner, R. (2021). *Baseline Analysis of the Soil at Forensic Cemetery ARISTA in Amsterdam* (tech. rep.). University of Amsterdam. Amsterdam.

Clay, R. (2006). Conductivity survey: a survival manual. In J. Johnson (Ed.), *Remote sensing in archaeology: An explicitly north american perspective* (pp. 79–108). University of Alabama.

Connor, M., Baigent, C., & Hansen, E. S. (2018). Testing the Use of Pigs as Human Proxies in Decomposition Studies. *Journal of Forensic Sciences*, *63*(5), 1350–1355. https://doi.org/10.1111/1556-4029.13727

Dautartas, A., Kenyhercz, M. W., Vidoli, G. M., Meadows Jantz, L., Mundorff, A., & Steadman, D. W. (2018). Differential Decomposition Among Pig, Rabbit, and Human Remains. *Journal of Forensic Sciences*, *63*(6), 1673–1683. https://doi.org/10.1111/1556-4029.13784

Dick, H., Pringle, J., Sloane, B., Carver, J., Wisniewski, K. D., Haffenden, A., Porter, S., Roberts, D., & Cassidy, N. J. (2015). Detection and characterisation of Black Death burials by multi-proxy geophysical methods. *Journal of Archaeological Science*, *59*, 132–141. https://doi.org/10.1016/J.JAS.2015.04.010

Ellwood, B. (1990). Electrical resistivity surveys in two historical cemeteries in Northeast Texas: A method for delineating unidentified burial shafts. *Historical Archaeology 1990 24:3*, *24*(3), 91–98. https://doi.org/10.1007/BF03374139

Ellwood, B., Owsley, D. W., Ellwood, S., & Mercado-Allinger, P. (1994). Search for the grave of the hanged Texas gunfighter, William Preston Longley. *Historical Archaeology 1994 28:3*, *28*(3), 94–112. https://doi.org/10.1007/BF03374192

Forbes, S., Stuart, B., & Dent, B. (2005). The effect of the method of burial on adipocere formation. *Forensic Science International*, *154*(1), 44–52. https://doi.org/10.1016/J.FORSCIINT.2004.09.109

France, D., Griffin, T., Swanburg, J., Lindemann, J., Clark Davenport, Trammell, V., Armbrust, C. T., Kondratieff, B., Nelson, A., Castellano, K., & Hopkins, D. (1992). A Multidisciplinary Approach to the Detection of Clandestine Graves. *Journal of Forensic Sciences*, *37*(6), 13337J. https://doi.org/10.1520/JFS13337J

Frohlich, B., & Lancaster, W. J. (1986). Electromagnetic surveying in current Middle Eastern archaeology: Application and evaluation. *http://dx.doi.org.tudelft.idm.oclc.org/10.1190/1.1442190*, *51*(7), 1414–1425. https://doi.org/10.1190/1.1442190

GF Instruments. (2020). CMD: Electromagnetic conductivity meters for multi-layer survey.

Hansen, F. (2019). *The Use of Common-Offset and Multiple-Offset GPR methods for Forensic Investigations* (Doctoral dissertation). Delft University of Technology. Delft.

Hansen, J., & Pringle, J. (2013). Comparison of magnetic, electrical and ground penetrating radar surveys to detect buried forensic objects in semi-urban and domestic patio environments. *Geological Society Special Publication*, *384*(1), 229–251. https://doi.org/10.1144/SP384.13

Hansen, J., Pringle, J., & Goodwin, J. (2014). GPR and bulk ground resistivity surveys in graveyards: locating unmarked burials in contrasting soil types. *Forensic science international*, *237*. https://doi.org/10.1016/J.FORSCIINT.2014.01.009

Jervis, J., Pringle, J., & Tuckwell, G. (2009). Time-lapse resistivity surveys over simulated clandestine graves. *Forensic Science International*, *192*(1-3), 7–13. https://doi.org/10.1016/J.FORSCIINT.2009.07.001

Johnston, G. (2021). Using GPR to Locate Unmarked Graves Webinar - YouTube. Retrieved December 6, 2021, from https://www.youtube.com/watch?v=rV5Z_6AUMUk

Jones, G. (2008). Geophysical Mapping of Historic Cemeteries. *Technical Briefs in Historical Archaeology*, *3*, 25–38.

Juerges, A., Pringle, J., Jervis, J. R., & Masters, P. (2010). Comparisons of magnetic and electrical resistivity surveys over simulated clandestine graves in contrasting burial environments. *undefined*, *8*(6), 529–539. https://doi.org/10.3997/1873-0604.2010041

Knobel, Z., Ueland, M., Nizio, K. D., Patel, D., & Forbes, S. L. (2018). A comparison of human and pig decomposition rates and odour profiles in an Australian environment. *https://doi-org.tudelft.idm.oclc.org/10.1080/00450618.2018.1439100*, *51*(5), 557–572. https://doi.org/10.1080/00450618.2018.1439100

Loke, M. H. (2015). *Tutorial : 2-D and 3-D electrical imaging surveys* (tech. rep.). www.geotomosoft.com

Milsom, J. (2003). *Field Geophysics: The Geological Field Guide Series* (3rd ed., Vol. 1). John Wiley Sons Ltd.

Milsom, J., & Eriksen, J. (2011). *Field Geophysics* (4th ed.). John Wiley Sons, Ltd. https://doi.org/10.1002/9780470972311

Molina, C. M., Pringle, J., Saumett, M., & Evans, G. (2016). Geophysical monitoring of simulated graves with resistivity, magnetic susceptibility, conductivity and GPR in Colombia, South America. *Forensic Science International*, *261*, 106–115. https://doi.org/10.1016/J.FORSCIINT.2016.02.009

Molina, C. M., Wisniewski, K., Drake, J., Baena, A., Guatame, A., & Pringle, J. (2020). Testing Application of Geographical Information Systems, Forensic Geomorphology and Electrical Resistivity Tomography to Investigate Clandestine Grave Sites in Colombia, South America. *Journal of Forensic Sciences*, *65*(1), 266–273. https://doi.org/10.1111/1556-4029.14168

Mulder, C. (2019). *ERT and GPR as Potential Geophysical Tools for Detecting Clandestine Buried Forensic Evidence* (Doctoral dissertation). Delft University of Technology. Delft.

Nobes, D. (1999). Geophysical surveys of burial sites: A case study of the Oaro urupa. *GEOPHYSICS*, *64*(2), 357–367. https://doi.org/10.1190/1.1444540

Oostra, R. J., Gelderman, T., Groen, W. J., Uiterdijk, H. G., Cammeraat, E. L., Krap, T., Wilk, L. S., Lüschen, M., Morriën, W. E., Wobben, F., Duijst, W. L., & Aalders, M. C. (2020). Amsterdam Research Initiative for Sub-surface Taphonomy and Anthropology (ARISTA) - A taphonomic research facility in the Netherlands for the study of human remains. *Forensic Science International*, *317*, 110483. https://doi.org/10.1016/J.FORSCIINT.2020.110483

Pringle, J., Giubertoni, M., Cassidy, N. J., Wisniewski, K. D., Hansen, J. D., Linford, N. T., & Daniels, R. M. (2015). The use of magnetic susceptibility as a forensic search tool. *Forensic Science International*, *246*, 31–42. https://doi.org/10.1016/J.FORSCIINT.2014.10.046

Pringle, J., & Jervis, J. (2010). Electrical resistivity survey to search for a recent clandestine burial of a homicide victim, UK. *Forensic Science International*, *202*(1-3), e1–e7. https://doi.org/10.1016/J.FORSCIINT.2010.04.023

Pringle, J., Jervis, J., Cassella, J., & Cassidy, N. (2008). Time-lapse geophysical investigations over a simulated urban clandestine grave. *Journal of forensic sciences*, *53*(6), 1405–1416. https://doi.org/10.1111/J.1556-4029.2008.00884.X

Pringle, J., Jervis, J., Hansen, J., Jones, G., Cassidy, N., & Cassella, J. (2012). Geophysical Monitoring of Simulated Clandestine Graves Using Electrical and Ground-Penetrating Radar Methods: 0–3 Years After Burial*,†. *Journal of Forensic Sciences*, *57*(6), 1467–1486. https://doi.org/10.1111/J.1556-4029.2012.02151.X

Pringle, J., Jervis, J., Roberts, D., Dick, H., Wisniewski, K., Cassidy, N., & Cassella, J. (2016). Long-term Geophysical Monitoring of Simulated Clandestine Graves using Electrical and Ground Penetrating Radar Methods: 4-6 Years After Burial. *Journal of forensic sciences*, *61*(2), 309–321. https://doi.org/10.1111/1556-4029.13009

Pringle, J., Ruffell, A., Jervis, J. R., Donnelly, L., McKinley, J., Hansen, J., Morgan, R., Pirrie, D., & Harrison, M. (2012). The use of geoscience methods for terrestrial forensic searches. *Earth-Science Reviews*, *114*(1-2), 108–123. https://doi.org/10.1016/J.EARSCIREV.2012.05.006

Pringle, J., Stimpson, I., Wisniewski, K., Heaton, V., Davenward, B., Mirosch, N., Spencer, F., & Jervis, J. (2020). Geophysical monitoring of simulated homicide burials for forensic investigations. *Scientific Reports 2020 10:1*, *10*(1), 1–12. https://doi.org/10.1038/s41598-020-64262-3

Reynolds, J. (2011). An Introduction to Applied and Environmental Geophysics 2nd Edition. *John Wiley Sons, Ltd*, 193.

Schultz, J. (2003). *Detecting buried remains in Florida using ground-penetrating radar - ProQuest* (tech. rep.). University of Florida. Florida.

Schultz, J. (2007). Using Ground-Penetrating Radar to Locate Clandestine Graves of Homicide Victims: Forming Forensic Archaeology Partnerships With Law Enforcement. *Homicide Studies*, *11*(1), 15–29. https://doi.org/10.1177/1088767906296234

Schultz, J. (2012). The Application of Ground-Penetrating Radar for Forensic Grave Detection. In D. Dirkmaat (Ed.), *A companion to forensic anthropology* (pp. 85–100). John Wiley Sons, Ltd. https://doi.org/10.1002/9781118255377.CH4

Schultz, J., & Martin, M. (2012). Monitoring controlled graves representing common burial scenarios with ground penetrating radar. *Journal of Applied Geophysics*, *83*, 74–89. https://doi.org/10.1016/J.JAPPGEO.2012.05.006

Schultz, J., & Martin, M. M. (2011). Controlled GPR grave research: comparison of reflection profiles between 500 and 250 MHz antennae. *Forensic science international*, *209*(1-3), 64–69. https://doi.org/10.1016/J.FORSCIINT.2010.12.012